POLITECNICO DI MILANO

SCHOOL OF INDUSTRIAL AND INFORMATION ENGINEERING

MASTER OF SCIENCE IN MATERIALS ENGINEERING AND NANOTECHNOLOGY

POLITECNICO
MILANO 1863

Two-dimensional sp-sp^2 carbon nanostructures: density functional theory simulations of structural, electronic and vibrational properties

Supervisor: Prof. Carlo S. Casari
Co-supervisor: Dr. Alberto Milani

Graduation thesis of:
Patrick Serafini
873747

ACADEMIC YEAR 2017-2018

Abstract

In my thesis work I have carried out a computational investigation, by means of Density Functional Theory (DFT), of 2D sp-sp^2 carbon nanostructures. Using a bottom up approach I have analyzed the electronic properties of molecular fragments having finite dimension and constituted by phenyl groups linked by diacetylenic units. This study aimed at investigating how intramolecular effects can affect the π-conjugation of the single fragments, modulating HOMO-LUMO band gap. First, size effects have been analyzed by computing the band gap of single one dimensional chains, made by phenyls and diacetylenic units, for increasing chain lengths. Then an analysis on electronic properties of finite molecular fragments was done, evaluating the band gap, depending on their connectivity (meta, ortho and para conjugation), extension and topology. The results obtained shows also how molcular simulations can be useful for the molecular design of novel innovative systems.

Based on this investigation, I have considered infinite periodic structures. At first, as a reference structure, I have studied electronic and vibrational properties of the infinite 2D graphdiyne (GDY). The analysis concerned the computation of the band structure, the evaluation of the band gap, and the prediction of the Raman spectra, with a detailed characterization of the normal modes associated to the main bands showed in the spectra. I drove then my attention towards GDY nanoribbons (GDYNRs), originated by "cutting" the infinite 2D structure along specific directions. By this way, depending on the edge type, armchair and zigzag nanoribbons can be built. The study aimed at analyzing how the different edges can affect electronic and vibrational properties of these structures. Therefore the band structure of armchair and zigzag GDYNRs was studied, depending on their width, and Raman spectra were computed and interpreted by analyzing the normal modes of vibrations. Marker bands of GDYNRs with different edges have been identified, providing important informations for the characterization of these new intriguing nanostructures.

Sommario

Nel mio lavoro di tesi ho condotto un'analisi computazionale, mediante calcoli di Density Functional Theory, di nanostrutture 2D sp-sp^2 di carbonio. Utilizzando un approccio bottom up, ho analizzato le proprietà elettroniche di frammenti molecolari di dimensione finita, costituiti da gruppi fenili collegati da unità diacetileniche. Tale studio vuole investigare come gli effetti intramolecolari possano influenzare la coniugazione π dei frammenti, modulando il gap HOMO-LUMO. Inizialmente, tali frammenti sono stati analizzati calcolando il band gap di singole catene monodimensionali, costituite da fenili e unità diacetileniche, al crescere della loro lunghezza. Quindi ho condotto un'analisi sulle proprietà elettroniche di frammenti molecolari, valutando il gap, in funzione della connettività (orto, meta, para), dell'estensione e della topologia. I risultati ottenuti mostrano come le simulazioni molecolari siano utili per il molecular design di nuovi sistemi innovativi.

Basandomi su tale studio, ho analizzato strutture periodiche infinite. Inizialmente, come riferimento, ho studiato le proprietà elettroniche e vibrazionali della grafdiina infinita 2D (GDY). L'analisi si è concentrata sul calcolo della struttura a bande, sulla valutazione del band gap e sulla previsione dello spettro Raman, accompagnata da una caratterizzazione dettagliata dei modi normali associati alle bande principali mostrate nello spettro. Ho quindi spostato l'attenzione verso nanoribbon di GDY (GDYNRs), originati "tagliando" la struttura 2D infinita lungo direzioni specifiche. Così, in funzione del tipo di bordo, possono essere costruiti dei nanoribbon armchair o zigzag. Lo scopo dello studio è quello di analizzare come i diversi bordi influenzano le proprietà elettroniche e vibrazionali di tali strutture. Perciò ho studiato la struttura a bande dei GDYNRs armchair e zigzag, in funzione del loro spessore, e ho calcolato ed interpretato i loro spettri Raman analizzando i modi normali di vibrazione. Inoltre sono state identificate le bande marker dei GDYNRs aventi bordi differenti, dando importanti informazioni per la caratterizzazione di queste interessanti nanostrutture.

Estratto

Questo lavoro di tesi si focalizza, attraverso un'indagine computazionale svolta mediante calcoli Density Functional Theory (DFT), sullo studio delle proprietà strutturali, elettroniche e vibrazionali di particolari sistemi molecolari ibridi 2D di carbonio in ibridizzazione sp-sp^2. Tale analisi è motivata dal fatto che negli ultimi 30 anni i materiali nanostrutturati a base di carbonio hanno raggiunto una grossa importanza nel campo della ricerca sulle nanotecnologie. In più le interessanti proprietà previste per l'allotropo ideale di carbonio sp, studiato solo a livello teorico e chiamato carbina, ha spinto molti gruppi di ricerca a concentrarsi sullo studio di strutture a base di carbonio caratterizzate da tale ibridizzazione. Negli ultimi 20 anni, l'attenzione si è riversata soprattutto sullo studio delle catene lineari finite di carbonio (CAWs), e nello studio delle loro proprietà elettroniche, ottiche e vibrazionali in funzione della loro struttura chimica e delle possibilità di sintetizzarle mediante opportuni metodi chimici e fisici. In tale contesto e in riferimento all'ancor più vasta tematica di ricerca che ha come focus il grafene, alcuni gruppi di ricerca hanno mosso la loro attenzione verso sistemi ibridi di carbonio sp-sp^2, sia dal punto di vista sperimentale che teorico. Il mio lavoro di tesi si colloca precisamente in quest'ultimo contesto.

Utilizzando un approccio bottom up ho innanzitutto analizzato, a livello teorico, le proprietà elettroniche di nanostrutture di dimensione finita costituite da gruppi fenili collegati tra di loro attraverso catene diacetileniche. I calcoli computazionali sono stati svolti utilizzando il funzionale PBE0 ed il set di base 6-31G(d,p), con il programma GAUSSIAN09. Lo studio è volto a comprendere come la connettività tra le unità diacetileniche (se in posizione meta, orto o para) ai gruppi fenili possa influire sulla coniugazione degli elettroni π dei singoli frammenti, modulandone il gap elettronico HOMO-LUMO. Per prima cosa ho analizzato il band gap di singole catene costituite da fenili e unità diacetileniche connesse ai fenili stessi nelle diverse posizioni meta, para ed orto, e come esso evolvesse all'aumentare delle unità diacetileniche lungo la catena. Quindi ho proceduto con l'analisi di singoli fram-

menti finiti formati dagli stessi gruppi chimici e ho valutato come l'estensione, la connettività tra le unità diacetileniche e la topologia stessa del frammento potesse influire sul band gap stesso proponendone un'interpretazione sulla base delle interazioni intramolecolari. Tale studio, oltre a chiarire meglio le proprietà di tali strutture, ha permesso di mettere a punto un "design" molecolare che può essere utile a gruppi di ricerca volti alla sintesi di tali molecole così da avere un riferimento sulle proprietà di strutture verso le quali orientare gli sforzi di sintesi.

Una volta comprese meglio le proprietà dei sistemi finiti, mi sono mosso verso l'analisi di strutture periodiche ed infinite. Questa analisi computazionale è stata fatta utilizzando i programmi CRYSTAL14 e CRYSTAL17 che operano applicando condizioni periodiche al contorno per trattare cristalli 1, 2 o 3D e utilizzando nuovamente il funzionale PBE0 e il 6-31G(d,p) set di base. Tale studio è stato motivato dalla volontà di analizzare una particolare struttura sp-sp^2 del carbonio, molto studiata recentemente in letteratura e denominata γ-grafdiina (GDY). Dall'analisi della GDY infinita 2D, il fine ultimo era di muoversi verso l'analisi delle proprietà elettroniche e vibrazionali di nanoribbon, costruiti "tagliando" la struttura infinita bidimensionale della γ-grafdiina lungo particolari direzioni e ottenendo delle strutture in cui viene imposto un confinamento lungo una delle due direzioni. Come modello di riferimento, la prima struttura periodica analizzata da me è stata appunto la grafdiina infinita. L'analisi si è focalizzata sia sul calcolo della struttura a bande, in modo da analizzare le proprietà elettroniche in termini di band gap, sia sull'interpretazione dettagliata dello spettro Raman svolgendo un'analisi dettagliata dei modi normali di vibrazione. Di seguito mi sono quindi dedicato all'analisi computazionale dei nanoribbon di grafdiina. In funzione delle direzioni lungo le quali è possible tagliare la struttura bidimensionale della grafdiina, due tipologie di nanoribbon con due differenti bordi possono essere ottenute: armchair e zigzag. Lo studio da me compiuto si è soffermato sull'analisi delle proprietà elettroniche e vibrazionali di tali strutture, in modo da comprendere come il tipo di bordo influisse su di esse, analizzando i relativi band gap e spettri Raman. Per quanto riguarda le proprietà elettroniche, è stato valutato il band gap e come il suo valore fosse influenzato dal tipo di bordo presente nella struttura nonchè come esso evolvesse con l'aumentare dello spessore dei nanoribbon, facendo luce sugli effetti di confinamento in questi sistemi. Infine lo spettro Raman è stato analizzato per diversi nanoribbon armchair e zigzag, con particolare attenzione ai modi normali associati alle bande marker che li contraddistinguono dalla GDY infinita. Oltre ad analizzare come tali picchi e modi normali associati evolvessero con l'aumentare dello

spessore del nanoribbon, è stato fatto anche un confronto tra gli spettri dei nanoribbon zigzag e armchair per capire se ci fosse un modo per distinguerli sulla base dei loro spettri Raman. Questa analisi è volta allo scopo di comprendere meglio le proprietà elettroniche e vibrazionali di tali strutture, ma anche di avere un buon strumento di caratterizzazione a supporto di studi condotti a livello sperimentale.

Contents

Chapter 1

Introduction

In the recent 30 years nanostructured carbon-based materials have reached a great importance in the field of nanoscience and nanotechnology. Fullerene, graphene, nanotubes and other forms of carbon are some examples of this big interest towards these type of materials. The continous research towards other exotic forms of carbon makes the recent period "The era of carbon allotropes" [1]. Moreover the absence of a real experimental *sp* allotrope, theoretically investigated and called *carbyne*, has stimulated a lot of scientists and reasearch groups in the investigation of *sp*-carbon based materials [2]. These materials are considered as possible novel nanostructures with innovative and peculiar electronic properties. More recently carbon atom wires (CAWs) started to be studied as possible novel materials in the field of molecular electronics [3]. These structures are studied both with experimental and theoretical/computational methods. From the experimental point of view, different techniques have been implemented to produce carbon atom wires [4], but different characterization techniques have been employed to determine their structural, vibrational and electronic properties. Parallel to experimental works, many computational investigations focused on the prediction of the properties of *sp*-carbon chains further revealed the interesting behaviour and the promising properties of these systems [3]. In this context, my thesis work is focused on theoretical investigations, by means of Density Functional Theory, of peculiar carbon nanostructures characterized by mixed *sp*-sp^2 hybridization. At first I focused my attention on molecular fragments made by hexagonal rings containing sp^2 hybridized carbon atoms, linked toghether by linear diacetylenic units where the hybridization of carbon was *sp*. The aim of this study was to give theoretical references of these structures for what concern their electronic and vibrational properties, expecially for chemists who synthesized them [5]. Infact we try to understand

their electronic behaviour, by evaluating the band gap, changing the type of fragment, the length and connection type of the *sp* units, the extension of the fragments themselves and other parameters to play, in a molecular design way, in the synthesis of these structures to obtain the desired properties. Moreover, studying the vibrational properties and in particular the Raman spectra of these structures, it is possible to provide a further interpretation useful for the characterization of novel systems properly designed and synthetized. The second part of my thesis focuses on the theoretical investigation of the 2D graphdiyne and on its nanoribbons made by cutting the infinite 2D crystal along specific directions. Also in this case, electronic and vibrational properties were analyzed. Band gap and Raman spectra of different type of nanoribbons were investigated as a function of their width and their edge-type. The aim of this study was to give a detailed characterization of grapdiyne nanoribbons and give an interpretation of their electronic properties in order to apply them in the future as possible novel materials in nanoelectronics.

Chapter 2

Carbon Atom Wires (CAWs) and hybrid sp - sp^2 carbon-based materials

2.1 Carbyne

Carbyne is defined as the one-dimensional infinite linear chain formed only by covalently bonded sp-carbon atoms. It is thus the true one dimensional atomic chain characterized by a diameter of only one atom. The production of single sp-carbon chains long enough to be reliably considered as an infinite one is nowadays challenging. The longest chains (up to 6000 atoms) identified up to now have been recently detected inside double-wall carbon nanotubes. The longest wire in isolated form has been synthesized by Tykwinski and Chalifoux [6] with lengths of more than 40 carbon atoms. For small chains it can be shown that their behaviour is ruled by end-effects while for long chains, with more than 50 carbon atoms, Peierls distortion takes place and rules the chain behaviour [7]. There are two possible forms of carbyne that possess different electronic and vibrational properties. The first one is called "polyyne" and it is characterized by an alternation, along the chain, of triple and single CC bonds. Due to this, the structure will be characterized by a certain bond length alternation ($BLA = r_1 - r_2$, with r_1 and r_2 bond distances of the single and triple bonds respectively, Fig. 2.1). The second one is called "cumulene" and can be described as a periodic repetition of only double bonds along the chain and will be characterized by $BLA = 0$. These two configurations would correspond to an insulating/semiconducting system for $BLA \neq 0$ (polyyne) or truly metallic systems when $BLA = 0$ (cumulene), revealing the usual connection between molecular structure (BLA) and electronic

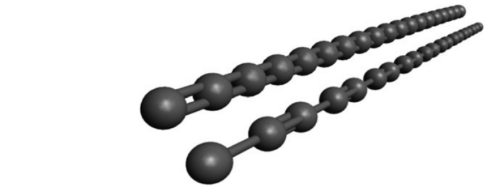

(a)

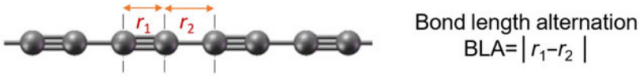

(b)

Figure 2.1: (a) The structure of ideal carbyne with the two possible configurations: cumulene (top) and polyyne (bottom) and (b) the bond length alternation (BLA) as the parameter to describe the structure of a finite wire [3]

properties (band gap) which is peculiar of polyconjugated molecules. Due to the previous cited Peierls distortion, occurring for an infinite chain, the only stable form is the polyynic one. A lot of computational works revealed that carbyne should have very unique properties such as a very high Young modulus (up to 32 TPa) and a specific stifness of about 10^9 Nm/kg, much higher than all the other materials, including carbon nanotubes, graphene and diamond. Thermal conductivity has been predicted to reach extremely high values (80-200 kW/mK for cumulenes and polyynes at room temperature) and it is attributed to high phonon frequencies and long phonon mean free path allowing ballistic thermal transport up to the microscale. Moreover, for what concern electronic properties, cumulene is expected to be a metal while polyyne a semiconductor with large electron mobilities and peculiar conductance behaviour, including ballistic transport even with spin polarization. [3]

2.2 CAWs: examples of carbyne-like systems

In the last 20 years more and more attention has been focused on sp-carbon chains. This interest was stimulated by the fact that different kinds of finite-length carbon atom chains have been syntesized. Raman spectroscopy has emerged as a strong characterization tool to unambiguosly identify and investigate these type of structures. Differently from Raman of sp^2-carbon systems that have Raman fingerprint signals in $1300-1600\ cm^{-1}$ region, Raman signals that characterizes sp-carbon

chains are located at $1800 - 2300\ cm^{-1}$. Through this technique, due to the fact that peak position downshifts for increasing wire length, it is possible to identify polyynes depending on their size [8]. Hydrogen-capped polyynes are a particularly simple and interesting system for which both synthesis, made by Cataldo [9], but also theoretical investigations were done [10]. In the second case, the trend of the BLA as a function of the increasing length of the *sp*-chain were analyzed in details. What it is found is that BLA decreases for increasing length of the chains due to the increase of π-electron conjugation. This sctructural variation is followed by a lowering of the gap between the highest occupied and the lowest unoccupied molecular orbitals (HOMO-LUMO gap). Obviously it is impossible to reach the 0 gap case of cumulene structure because at some length Peierls distortion occurs but chemical strategies have been developed to this aim for short systems. Indeed for small molecules made by relatively short carbon chains, the predominant effect in inducing a cumulene or polyynic structure along the chain is given by the end groups [11]. Infact, for example, for hydrogen-capped polyynes the terminal $-CH$ bond forces the next CC bond to have a triple character, the next one to have a single character and so on, thus inducing a polyynic structure. Instead, a $= CH_2$ terminal group will force, in the same way, the next CC bond to be double and so on, inducing in this way a cumulenic structure. Cumulenic structures have been synthetized by Tykwinski and co-workers using the approach of the end groups. Infact quite short *sp*-carbon chains have been terminated by an sp^2-carbon atom connected to two substituted phenyl groups, creating a chemical connection similar to that presented by ideal vinylidene-capped molecules. So, thanks to these end-groups, the *sp*-carbon chains are forced to display a cumulenic equalized geometry [12].

2.3 Novel $sp - sp^2$ carbon-based materials

Carbon atom wires can be fundamental units also for more complex nanostructured and novel materials, characterized by peculiar and tunable properties. In particular we will focus on novel $sp - sp^2$ systems, such as graphyne, graphdiyne and related fragments reported in Fig. 2.2.

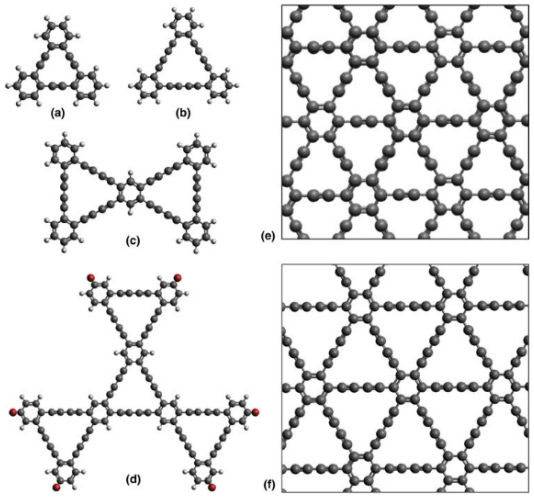

Figure 2.2: Structures of $sp \rightarrow sp^2$ molecular fragments of graphyne (a) and graphdiyne of increasing size (b→d). In model (d), the red spheres represent bis-terbutyl substituted phenyl groups. The structure of extended 2D graphyne and graphdiyne is reported in (e) and (f), respectively. [3]

Graphyne (GY) and graphdiyne (GDY) are indeed hybrid sp/sp^2 carbon systems presenting a well-organized and regular arrangement of the atoms. The 2D crystal of these systems is constituted by sp^2-carbon hexagons interconnected by means of sp-carbon chains having different lengths (GY and GDY sp-carbon chains are formed respectively by 2 and 4 carbon atoms). These structures stimulated the attention in the last decade mainly for their very peculiar electronic properties. Following a bottom-up approach it was possible, for example by Haley, to synthesize 2D molecules as subfragments of GDY of different topology and dimension (Fig. 2) [13]. Regarding 2D $sp - sp^2$ crystals some efforts were spent towards the on-surface synthesis of GDY structures. In this context, Xu and co-workers have demonstrated that it is possible to fabricate 2D graphdiyne-like systems by depositing halogenated precursors and by promoting an homocoupling reaction on a gold surface and then analyzed with STM microscopy [14].

2.4 The infinite graphdiyne

As already mentioned above, graphdiyne is a one-atom-thin carbon network (like graphene), which can be constructed by replacing some $-C-C-$ bonds in graphene with uniformly distributed diacetylenic linkages $-C \equiv C-C \equiv C-$. As a result, such flat carbon (sp^2+sp) net-

works with a high π-conjugation, uniformly distributed pores, density much smaller than for graphene and with tunable electronic properties are considered now as possible promising materials for nanoelectronics, as membranes, for energy storage applications or as candidates for anode materials in batteries [15]. Among the different types of graphdiyne, we will focus our attention on the γ-graphdiyne whose structure is reported in Fig. 2.3. The $C - C$ bonds in the hexagons

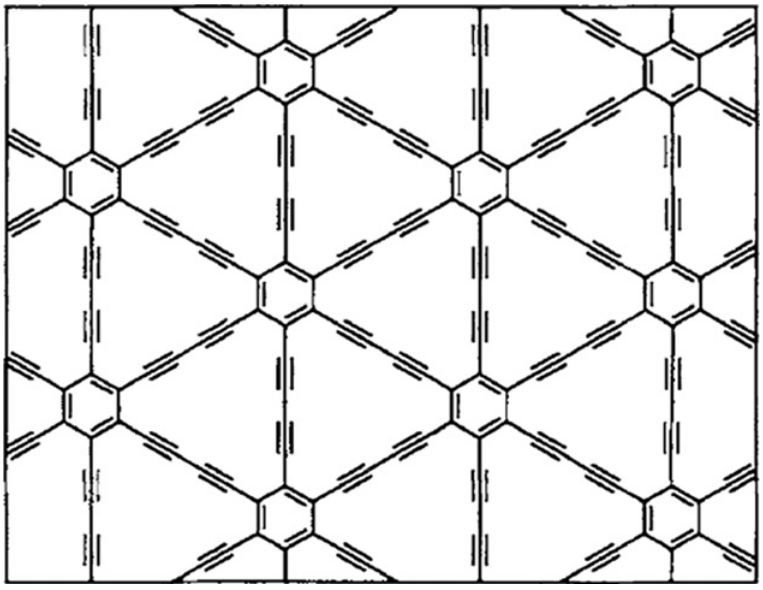

Figure 2.3: Structure of γ-graphdiyne [15]

and in diacetylenic linkages are not uniform, reflecting different bonding types for each pair of carbon atoms. This diversity leads to greater structural flexibility of GDYs as compared with graphene. On the other hand the presence of diacetylenic units in 2D carbon networks decreases their stability in comparison with graphene and some other sp^2 like graphene allotropes. From the electronic point of view, GDY is a semiconductor with direct band gap at Γ point of the Brillouin zone (wavevector k=0).

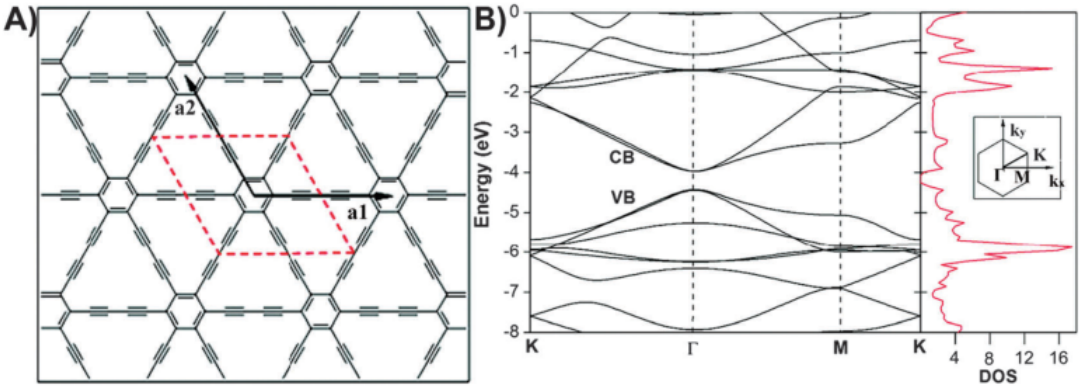

Figure 2.4: Schematic representation of a single GDY sheet. Band structure and density of states for a single GDY sheet, obtained from DFT calculations. The Brillouin zone is also shown. [16]

The band structure includes deep σ-type bands, whereas the low-energy $\pi(\pi^*)$ bands form the edges of the gap (Fig. 2.4). The reported band gaps usually go from 0.46 to 1.22 eV depending on the applied methods and the exchange-correlation functionals used [15]. In Tables 2.3, 2.2 some values of the band gap are reported.

Table 2.1: Lattice constant and band gap values of GDY taken from the literature and calculated with different methods and exchange-correlation functionals [15].

	GDY
a(Å)	9.44^b;9.464^d;9.48^h;9.37^i
BG(eV)	0.53^b-0.52/1.18^d-1.22^e-044/1.10^g-0.46^h-0.53^i

Table 2.2: Band gap values from the literature [15]

b	FP-LCAO	*d*	VASP: GGA-PBE/Crystal06: B3LYP
e	hybrid exchange-correlation functional	*g*	ABINIT-YAMBO: LDA/GW
h	VASP-PAW: GGA/PBE	*i*	CASTEP: GGA/PBE

Table 2.3: Computational details of the band gap values [15]

GDY has an hexagonal simmetry and belongs to the two-dimensional space-group *P6/mmm* (D_{6h}) in the Hermann-Maugin notation [17]. For the first-order Raman scattering, the process is limited to phonons at the Brillouin zone center Γ point respecting the law of momentum

conservation. The calculated Raman spectra and atomic motions of vibrational modes of γ-GDY are shown in Fig. 2.5 [18].

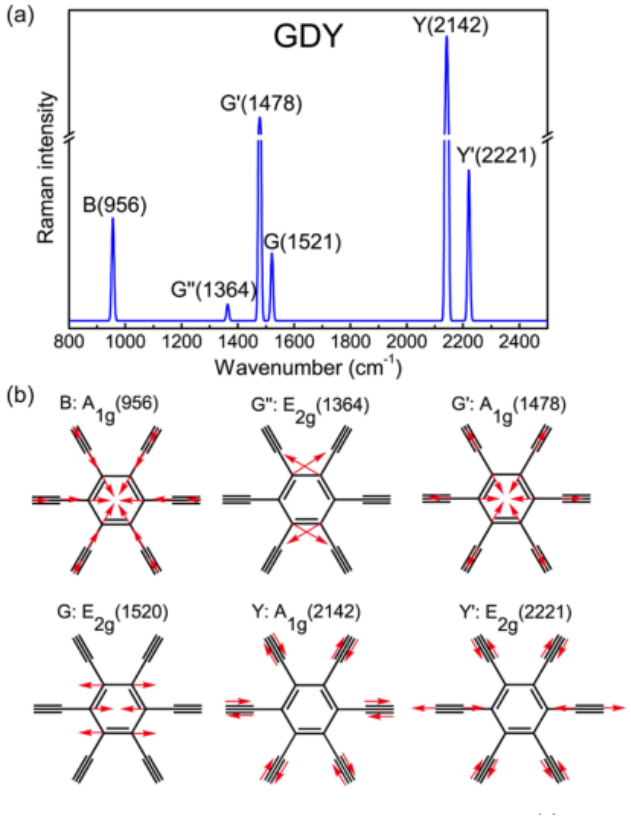

Figure 2.5: Raman spectra and vibrational modes of GDY. (a) Raman spectrum (b) Atomic motions of intense Raman-active modes, in which the red arrows show the motion directions of the main contributors. [18]

The graphdiyne has six intense Raman peaks: the breathing vibration of the hexagonal benzene rings is B, the vibrations related to sp^2 carbon are G,G' and G" (similar to other carbon-based sp^2 materials), and the alkyne-related modes are Y and Y'. The G peak comes from stretching of aromatic bonds as in graphene, but it is characterized by low intensity and wavenumber. The Y peak comes from the synchronous stretching/contracting of triple bonds, which is a fully symmetric mode. The G" peak is connected to the scissoring vibration of atoms in benzene ring. The G' peak comes from the vibrations of C-C bonds between triply coordinated atoms and theirs doubly coordinated neighbors (G' is even stronger than G). The Y' peak is another stretching mode of alkyne triple bonds, but the vibrations of different

triple bonds are out-of-phase: one-third of triple bonds are stretching while the remaining two-thirds are shortening.

2.5 Graphdiyne nanoribbons

A finite graphene sheet has edges, in which there are atoms with different coordination numbers and dangling bonds. These structures, called nanoribbons (NRs), exhibit properties different from the ideal infinite graphene sheet and are now widely investigated [19]. For these reasons attention was paid also to similar structures: *sp*-sp^2 nanoribbons of GYs (GY-NRs) and GDYs (GDY-NRs). Ribbon width, edge morphology, edge functionalization and other parameters can be modified to tailor electronic, chemical, mechanical and magnetic properties. Generally two main types of the most symmetric variants of edge configurations of ribbons, designed by "cutting" through infinite GY and GDY networks, may be analyzed: zigzag and armchair [15] (Fig. 2.6).

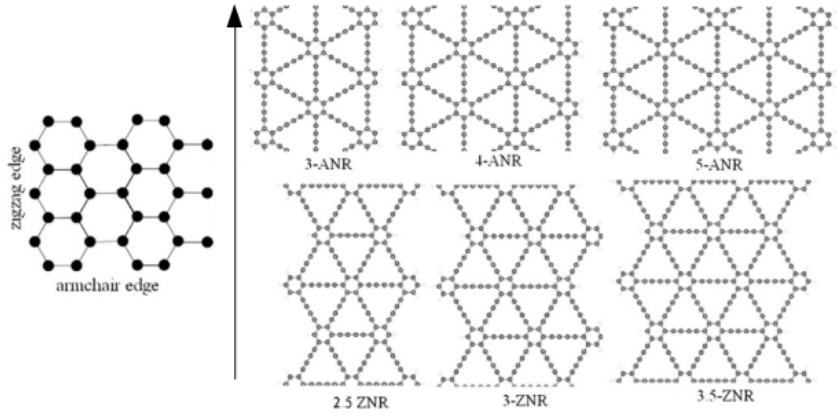

Figure 2.6: The structures of armchair (ANR) and zigzag (ZNR) graphdiyne nanoribbons labeled according to the number of chains of C_6 hexagons. On the left: the configurations of zigzag and armchair edges for graphene ribbons are illustrated. The arrow inicates the periodic axis of the nanoribbons [15]

Concerning GDY nanoribbons, a simple nomenclature of NRs was proposed, where the index n indicates the number of repeated units ($-C_6 - C \equiv C - C \equiv C - C_6 - C \equiv C - C \equiv C - C_6$-) that can be counted along the width of the ribbon. For this scheme, armchair nanoribbons (ANRs) are defined by only integers value of n, whereas for zigzag nanoribbons (ZNRs) the number of repeated units n can be

also an half integer. Examples of such structures are shown in Fig. 2.6.

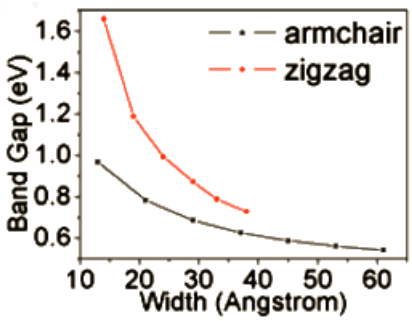

Figure 2.7: Trend in the band gap as a function of the nanoribbons' width for zigzag and armchair NRs. [20]

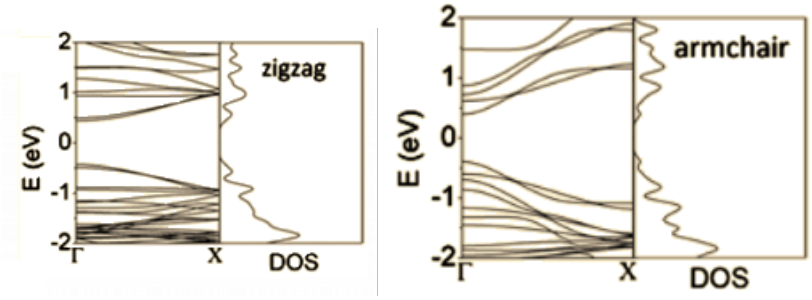

(a) (b)

Figure 2.8: (a),(b) Band structures and density of states (DOS) for zigzag and armchair nanoribbons with n=3 are reported. LDA functional was used for the calculations [20]

A lot of computational studies have been carried out to study electronic properties of these structures. ANRs and ZNRs with variable width were analyzed and it was found that all these ribbons are still semiconductors and their band gaps decrease as the ribbon width increases approaching, as expected, the limit of the 2D-GDY as reported in Figs. 2.7, 2.8 [21] [20]. Analyzing the stability of NRs passivated by H atoms at the edges, it was found that they are more stable than the "parent" 2D networks; besides, stability of graphdiyne nanoribbons decreases as their widths increase. Moreover, the extimation of the Young's modules of GDY ribbons demonstrate that the elastic stiffness of graphdiyne NRs is much smaller than for graphene ribbons [21].

2.6 Possible applications of GDYs

For their peculiar structural, mechanical and electronic properties, studied in detail by several theoretical works, graphdiynes have a lot of possible applications as superb contenders for nanoscale semiconductors with adjustable gaps, as new materials with direction-dependent mechanical properties for possible nanomechanical applications, for electronic and opto-electronic devices, for hydrogen storage [15]. Sun et al have studied graphdiyne sheets decorated with lithium and the calculations show that these sheets can host a large amount of lithium, suggesting these materials to be designed as anode materials for lithium batteries [22]. Another possible application of graphdiyne sheets could be their use as separation membranes for hydrogen purification from syngas, that usually contain undesired molecules like CH_4 and CO. Due to their thickness of one atom, they seem to be the most promising candidates because the efficiency of the membrane decreases with the increase of its thickness [23]. Water desalination through nanoporous membranes has been suggested as an energy-efficient method that could substitute commercial technologies, such as reverse osmosis. Buehler et al. demonstrated that a carbon "nanoweb" allowing both barrier-free permeation of water molecules and perfect rejection of salt ions would be an ideal candidate for water desalination [24]. A carbon nanoweb can be built from a monolayer of GY or GDY, robust and porous, with well defined atomic triangular pores. The search for new GDY-based materials and their applications is today at its initial stage and will probably expand in future research.

Chapter 3

Theoretical Background

3.1 Quantum Chemistry Theory for Crystalline and Molecular Calculations

In this chapter principles of quantum chemistry [25] and, in particular, of *Density Functional Theory* will be presented [26], [27], [28], [29], [30]. First, basic principles of quantum mechanics will be introduced [31], and then the Hartree-Fock theory will be presented. After the treatment of correlated methods based on Hartree-Fock, DFT will be analyzed.

3.1.1 The Schrödinger equation

In quantum mechanics, a certain physical state can be described by a specific function that takes the name of wavefunction. It usually depends on three variables that are position in space, time and spin, and it can be evaluated as the solution of a very famous equation called Schrödinger equation. This one involves time and space derivatives of the wavefunction and can be written as :

$$i\hbar\frac{\partial\Psi}{\partial t} = \hat{\mathcal{H}}\Psi \tag{3.1}$$

Writing the wavefunction as the product between two differnt terms that respectively depend on time and space it's possible to separate the two variables and to write a time independent Schrödinger equation.

$$\hat{\mathcal{H}}(\vec{r})\Psi(\vec{r}) = E(\vec{r})\Psi(\vec{r}) \tag{3.2}$$

The energetic description of a particle is embedded in the Hamiltonian operator $\hat{\mathcal{H}}$, that is usually the sum between the kinetic and potential

term of the overall system:

$$\hat{\mathcal{H}} = \sum \left(-\frac{\hbar^2}{2m_i}\nabla_i^2 \right) + \hat{\mathcal{V}} \tag{3.3}$$

Considering this expression for the Hamiltonian we are neglecting all the possible spin-spin interaction or spin-orbit couplings due to the absence of external magnetic perturbations. The sum is done over all the particles that are present in the system we are considering, and the potential term expresses all the possible interactions between them. Now we can consider a system of M nuclei and N electrons that can be described respectively by position vectors $\vec{R}_A$ and $\vec{r}_i$. We define $\vec{r}_{iA}$ the distance between the i electron and the nucleus A, $\vec{R}_{AB}$ the distance between nuclei A and B and $\vec{r}_{ij}$ the distance between the i and the j electron :

$$\vec{R}_{AB} = \vec{R}_A - \vec{R}_B \quad \vec{r}_{iA} = \vec{r}_i - \vec{r}_A \quad \vec{r}_{ij} = \vec{r}_i - \vec{r}_j \tag{3.4}$$

Now we can write the Hamiltonian associated to this system :

$$\hat{\mathcal{H}} = -\sum_{i=1}^{N}\frac{1}{2}\nabla_i^2 - \sum_{A=1}^{M}\frac{1}{2M_A}\nabla_A^2 - \sum_{i=1}^{n}\sum_{A=1}^{M}\frac{Z_A}{\vec{r}_{iA}} + \sum_{i=1}^{N}\sum_{j>1}^{N}\frac{1}{\vec{r}_{ij}} + \sum_{A=1}^{M}\sum_{B>A}^{M}\frac{Z_A Z_B}{\vec{R}_{AB}} \tag{3.5}$$

M_A rapresents the ratio between the mass of the A nucleus and the mass of the electron while Z_A is the A nucleus' atomic number. The first two terms are respectively the kinetic energies of electrons and nuclei in the system, the third term is the attraction term between electrons and nuclei while the other two remaining terms are the repulsive contributions between two electrons and two nuclei respectively.

3.1.2 Born-Oppenheimer approximation

To deal with the problem we have to do a lot of approximations, due to its complexity. The first important semplification is called Born-Oppenheimer or adiabatic approximation. It is based on the fact that nuclei are thousand of times heavier with respect to electrons, which means that their velocity will be very lower with respect to that of electrons. So considering this, we can solve the elctronic problem of the system considering nuclei as frozen. In this way the kinetic energy of the nuclei can be neglected (adiabatic term) and the nuclei-nuclei repulsion can be considered as a constant. So the electronic problem can be solved separately and will depend only parametrically on nuclei coordinates; the Hamiltonian of the system of N particles in a field of

M nuclei can be written in the following way:

$$\hat{\mathcal{H}}_{elec} = -\sum_{i=1}^{N} \frac{1}{2}\nabla_i^2 - \sum_{i=1}^{N}\sum_{A=1}^{M} \frac{Z_A}{\vec{r}_{iA}} + \sum_{i=1}^{N}\sum_{j>i}^{N} \frac{1}{\vec{r}_{ij}} \tag{3.6}$$

So the stationary state Schrödinger equation for the electrons will become :

$$\hat{\mathcal{H}}_{elec}\Psi_{elec}(\vec{r}_i;\vec{R}_A) = \varepsilon_{elec}(\vec{R}_A)\Psi_{elec}(\vec{r}_i;\vec{R}_A) \tag{3.7}$$

In which both wavefunction and eigenvalues depends parametrically on nuclear coordinates. This means that for each set of nuclear coordinates we have a different expression of the wavefunction with respect to electronic coordinates. So the electronic problem is solved at first and then the nuclear problem can be considered. In this way we can take into account the effect of electrons on nuclei considering their mean field. So the total energy for the nuclei can be written, adding the nuclear repulsion term, as:

$$\varepsilon_{tot} = \varepsilon_{elec} + \sum_{A=1}^{M}\sum_{B>A}^{M} \frac{Z_Z Z_B}{\vec{R}_{AB}} \tag{3.8}$$

In this way, writing the Hamiltonian for nuclei in which we insert the mean field generated by electrons (evaluated from the electronic equation), it can be found that the total energy of the system is the potential term nuclei are subjected to. So the Hamiltonian for nuclei will be:

$$\hat{\mathcal{H}}_{nucl} = -\sum_{A=1}^{M} \frac{1}{2M_A}\nabla_A^2 + \varepsilon_{tot}(\vec{R}_A) \tag{3.9}$$

This approximation considers nuclei moving on the potential energy surface obtained from the solution of the electronic problem. The solution of the Schrödinger equation for nuclei gives informations on vibrations of the system. The total wavefunction, under the Born-Oppenheimer approximation, will be the product between the electronic and the nuclear one:

$$\Psi_{tot}(\vec{r}_i;\vec{R}_A) = \Psi_{elec}(\vec{r}_i;\vec{R}_A)\Psi_{nucl}(\vec{R}_A) \tag{3.10}$$

3.1.3 Hartree approximation

Now we will focus on the electronic problem. Although the adiabitic approximation is very important to simplify the system, it is not sufficient to solve it completely. Infact the electronic problem remains very

complicated and it is necessary to make further approximations. The first one was given by Hartree that considered the system of electrons as a system of non interacting particles. The interaction between them was taken into account introducing a mean field felt by each single electron. In this way the total Hamiltonian can be written as the sum of single particle Hamiltonians:

$$\hat{\mathcal{H}} = \sum_{i=1}^{N} h(i) \tag{3.11}$$

Where h(i) is the sum of kinetic and potential term of a single electron i. In this approximation, the Hartree proposal was to write the wavefunction of the overall system of electrons as the product of single particle wavefunctions:

$$\Psi^{HP} = \Psi(\vec{r}_1, \vec{r}_2, \vec{r}_3, ..., \vec{r}_N) = \psi_1(\vec{r}_1)\psi_2(\vec{r}_2)\psi_3(\vec{r}_3)...\psi_N(\vec{r}_N) \tag{3.12}$$

Writing the total wavefunction as the so called Hartree product, the Schrödinger equation for the electrons will be:

$$\hat{\mathcal{H}}\Psi^{HP} = E\Psi^{HP} \tag{3.13}$$

Where:

$$E = \varepsilon_i + \varepsilon_j + ... + \varepsilon_k \tag{3.14}$$

The Hartree product is an uncorrelated function whose square modulus describe the probability density to find electron 1 in x_1, electron 2 in x_2 and so on independently from the position of the other electrons.

3.1.4 Pauli exclusion principle and antisymmetry

The big disadvantage of the wavefunction written as an Harteee product, so as the product of single particle wavefunctions, is that it doesn't respect the antisymmetry principle and it doesn't take into account that electrons are indistinguishable. Infact, due to the fact that electrons are fermions, the total wavefunction of a system made by these particles must be antisymmmetric. For this reason, the sign of the wavefunction must change due to a coordinate exchange between two particles

$$\psi(x_1, x_i, ..., x_j, ..., x_N) = -\psi(x_1, x_j, ..., x_i, ..., x_N) \tag{3.15}$$

To take into account the antisymmetry principle we can write the total wavefunction of the system as a Slater determinant. For a system of N

electrons, it can be written in the following way:

$$\Psi(1,2,3,...,N) = \frac{1}{\sqrt{N!}} \begin{vmatrix} \psi_1(1) & \psi_2(1) & ... & x_N(1) \\ \psi_1(2) & \psi_2(2) & ... & x_N(2) \\ \vdots & \vdots & ... & \vdots \\ \psi_1(N) & \psi_2(N) & ... & x_N(N) \end{vmatrix} \tag{3.16}$$

In which the single wavefunctions inside the determinant are rapresented by molecular orbitals. The coordinates exchange between two electrons consists in the exchange between two rows that causes an inversion in the sign of the wavefunction. Furthermore if two columns are equal the determinant is zero, and this fact takes into account the Pauli exclusion principle. So the Slater determinant considers the so called *exchange* effects that are neglected using the Hartree product. In this way the movement of electrons with parallel spin is correlated in some way, but the motion of the anti-parallel spin electrons remains uncorrelated. For this reason the Slater determinant is considered as a theory that doesn't take into account the correlation.

3.1.5 Hartree-Fock approximation

Taking a system constituted by N electrons, we can describe its wavefunction with a Slater determinant made by single particle wavefunctions. For this procedure the variational method is used. Based on this principle, the wavefunction that fits in the best way the system we are considering is the one that minimize the energy :

$$E_0 = \left\langle \Psi_0 | \hat{\mathcal{H}} | \Psi_0 \right\rangle \tag{3.17}$$

By minimizing E_0 it is possible to derive the equation for the optimized orbitals, the Hartree-Fock equation:

$$f(i)\psi = \varepsilon\psi \tag{3.18}$$

where f(i) is the Fock operator :

$$f(i) = -\frac{1}{2}\nabla_i^2 - \sum_{A=1}^{M} \frac{Z_A}{\vec{r}_{iA}} + \nu^{HF}(i) \tag{3.19}$$

in which ν^{HF} is the mean potential felt by the i electron generated by all the other electrons. In this way the many-body problem is reduced to a one-body due to the fact that the electron-electron repulsion is treated as a mean effect. However the mean field depends on the wavefunctions themselves, so to solve this problem it is necessary to use an iterative

procedure called SCF (*Self-Consistent-Field*). The procedure starts with the selection of the trial orbitals, and at first the equation is used to evaluate the mean field with these ones. Then, with the calculated mean field, the equation is solved to compute the new orbitals that will be used to evaluate the new mean field of the system. This procedure is repeated until it converges to a certain value of mean field, so when the potential found in the last step is equal to the next one and the orbitals used to build the Fock operator are equal to its wavefunctions. At this point it is said that the system reached the *selfconsistency*. The Slater determinant written with the computed orbitals is the wavefunction of the fundamental state. The remaining orbitals are called virtual orbitals and are empty. So a finite basis set, as explained later, is used and the more it's extended, the lower is the energy evaluated. The Fock operator can be written as the sum of three terms; the first one is:

$$h(1) = -\frac{1}{2}\nabla_1^2 - \sum_A \frac{Z_A}{\vec{r}_{1A}} \tag{3.20}$$

that is the sum between the kinetic and potential energy related to elctron-nucleus attraction. The other two terms are the ones that constitute ν^{HF}. The first one is present also in the Hartree theory and is the *Coulomb* operator that rapresents the coulombic repulsion between electrons:

$$\hat{\mathcal{F}}_b(1) = \int dx_2 \psi_b(2)^2 \vec{r}_{12}^{-1} \tag{3.21}$$

it rapresents the mean potential in x_1 due to an electron in the ψ_b state. The second term is the *exchange* operator, whose expression is defined for its effect on the orbital ψ_a:

$$\hat{\mathcal{K}}_b(1)\psi_a(1) = \left[\int dx_2 \psi_b^*(2)\vec{r}_{12}^{-1}\psi_a(2)\right]\psi_b(1) \tag{3.22}$$

Finally the Hartree-Fock equation can be written in the following way:

$$\left[h(1) + \sum_{b\neq a}\hat{\mathcal{F}}_b(1) - \sum_{b\neq a}\hat{\mathcal{K}}_b(1)\right]\psi_a(1) = \varepsilon_a\psi_a(1) \tag{3.23}$$

and, in a more compact way, we can write also the Hartree-Fock operator as:

$$\nu^{HF}(1) = \sum_b \hat{\mathcal{F}}_b(1) - \hat{\mathcal{K}}_b(1) \tag{3.24}$$

so that the Fock operator becomes the sum of the core Hamiltonian and the Hartree-Fock operator previously defined:

$$f(1) = h(1) + \nu^{HF}(1) \tag{3.25}$$

3.1.6 Quantum theory for crystals: The Bloch Theroem

Due to the fact that in the thesis work I dealt with crystalline structure, it is necessary to describe the Hartree-Fock theory applied to crystals. They can be described by two elements: a lattice and a basis. The lattice is a volume in 1D, 2D or 3D made by a discrete infinite set of points. We can define the so called primitive cell as the smallest volume of space able to reconstruct, by rigid translation, all the crystal. This peculiar property of crystals is named translational symmetry. The basis is rapresented by the number of lattice points that are present in the primitive cell. This one will be characterized by a certain number of vectors, depending on the considered dimension, called basis vectors. Each point, for a 3D case, can be described by the following formula:

$$\vec{T}_n = n_1\vec{a}_1 + n_2\vec{a}_2 + n_3\vec{a}_3 \tag{3.26}$$

where a_1, a_2 and a_3 are the basis vectors of the lattice. The basis of the crystal consists in the number of elements or atoms that composes the primitive cell. Usually crystals, over the translational symmetry, possess also other types of symmetry like the point group ones. Due to translational invariance each physical property of the crystal must be invariant under translation and so it is periodic:

$$f(\vec{r} + \vec{T}_n) = f(\vec{r}) \tag{3.27}$$

Moreover, every periodic physical property can be written in the form of a Fourier series:

$$f(r) = \sum_{n_1,n_2,n_3} f_n exp^{\left[i\frac{2\pi}{V_C}\vec{T}_n\vec{r}\right]} \tag{3.28}$$

where V_C is the primitive cell volume:

$$V_C = |\vec{a}_1 * \vec{a}_2 \times \vec{a}_3| \tag{3.29}$$

Doing this, we have defined another set of points, called reciprocal space, described by the following formula:

$$\vec{K} = K_1\vec{b}_1 + K_2\vec{b}_2 + K_3\vec{b}_3 \tag{3.30}$$

Where $\vec{b}_1$,$\vec{b}_2$ and $\vec{b}_3$ are the primitive lattice vectors of the reciprocal space. So for each direct lattice there is one reciprocal lattice associated to and they are linked by each other by the Fourier transform:

$$f(r) = \sum_K f_n e^{i\vec{K}\vec{r}} \tag{3.31}$$

In crystals we can write the Schrödinger equation in the same way of a molecule, but the translational symmetry must be taken into account:

$$\hat{H}(\vec{r})\psi(\vec{r}) = E\psi(\vec{r}) \tag{3.32}$$

Considering a generic lattice translational vector T_n the solution of the equation:

$$\hat{H}(\vec{r} - \vec{T}_n)\psi(\vec{r} - \vec{T}_n) = E\psi(\vec{r} - \vec{T}_n) \tag{3.33}$$

must be the same of the (32). Using group theory it is possible to demonstrate that each eigenfunction of the Schrödinger equation satisfies the following relationship:

$$\Phi(\vec{r} + \vec{T}_n; \vec{k}) = e^{i\vec{k}\vec{T}_n}\Phi(\vec{r}; \vec{k}) \tag{3.34}$$

in which k is the wavevector of the reciprocal space and $\Phi(\vec{r}; \vec{k})$ is the so called Bloch's function. This equation rapresents the first form of the Bloch's theorem. Moreover it is possible to write the eigenfunction as the product between a plane wave modulated by a periodic function with the same periodicity of the crystal lattice:

$$\Phi(\vec{r}; \vec{k}) = e^{i\vec{k}\vec{r}}u_{\vec{k}}(\vec{r}) \tag{3.35}$$

This is called second form of the Bloch's theorem. An important property of this theorem is that $\Psi(\vec{r}; \vec{k})$ and $\Psi(\vec{r}; \vec{k} + \vec{K})$ are eigenfunctions corrisponding to the same eigenvalue:

$$\Psi(\vec{r} + \vec{T}_n; \vec{k} + \vec{K}) = e^{i(\vec{k}+\vec{K})\vec{T}_n}\Psi(\vec{r}; \vec{k} + \vec{K}) \tag{3.36}$$

Being $e^{i\vec{K}\vec{T}_n} = 1$

$$\Psi(\vec{r} + \vec{T}_n; \vec{k} + \vec{K}) = e^{i\vec{k}\vec{T}_n}\Psi(\vec{r}; \vec{k} + \vec{K}) \tag{3.37}$$

and so $\Psi(r; k)$ and $\Psi(r; k+K)$ are eigenfunctions of the same eigenvalue $E(k + K) = E(k)$. The consequence of this theorem is that the set of energy eigenvalues in the reciprocal space, that are called energy bands, are periodic with period equal to K. So it is possible to restrict the study of the electronic bands only in the so called first Brillouin zone, that is the primitive cell in the reciprocal space (from $-K$ to $+K$).

3.1.7 Born Von Karman boundary conditions

Until now we have supposed that crystals are infinite, but it is not true. They are finite, and so it is necessary to introduce some boundary conditions compatible with the property of translational invariance.

Considering a crystal made by N cells, we can impose that the wavefunction in the first cell coincides with that of the last one:

$$\Psi(r + mNa; k) = e^{imNak}\Psi(r; k) = \Psi(r; k) \tag{3.38}$$

and so:

$$e^{imNak} = 1 \tag{3.39}$$

From this expression we can understand that only some k values within the first Brillouin zone are possible to exist, in particular:

$$k = (\frac{\pi n}{Na}) \tag{3.40}$$

Where n is an integer number. These conditions are called Born Von Karman boundary conditions and set a discretization of k values in the k-space. But, due to the fact that usually N is a very big number for macroscopic crystals, the discretization in reciprocal space is very small and the discrete values seem to be a continuum.

3.1.8 Roothan-Hall equations

The Hartree-Fock equation cannot be implemented efficiently with numerical algorithms because reliable procedures to obtain numerical solutions have not been yet found to solve the integro-differential equation. However, thanks to Roothan, it is possible to write it in a matrix form in order to be solved with numerical calculations. The idea to bypass the limitation was to write the wavefunctions, so the molecular orbitals, as a set of known functions. In this way the HF equation becomes an algebraic equation resolvable by matrix algebra. Therefore the molecular orbitals were expressed as a linear combination of atomic orbitals and these atomic orbitals are themselves approximated with gaussian contractions. So introducing a certain set of K known functions called basis set, we can write MO (molecular orbitals) as a linear expansion:

$$\psi_i = \sum_{\mu=1}^{K} C_{\mu i}\phi_\mu \quad i = 1, 2, ..., K \tag{3.41}$$

The accuracy of the approximation becomes higher the more you expand the set of atomic orbitals, so an exact expansion for an infinite basis set would be obtained. But for computational limitations a finite basis set must be used. Now considering the closed-shell Hartree-Fock equation in which we have only the spatial dependence of the wavefunction:

$$f(r_1)\psi_j(\vec{r}_1) = \varepsilon_j\psi_j(\vec{r}_1) \tag{3.42}$$

and by left multiplying for $\phi_\mu^*(1)$ and integrating over $d\vec{r}_1$ the (42) after that we have substituted the linear expansion, we obtain a matrix expression of the equation. Infact defining the overlap matrix:

$$S_{\mu\nu} = \int d\vec{r}_1 \phi_\mu^*(1)\phi_\nu(1) \tag{3.43}$$

and the Fock matrix:

$$F_{\mu\nu} = \int d\vec{r}_1 \phi_\mu^* f(1)\phi_\nu(1) \tag{3.44}$$

the matrix equation becomes:

$$\sum_\nu F_{\mu\nu}C_{\nu i} = \varepsilon_i \sum_\nu S_{\mu\nu}C_{\nu i} \quad i = 1, 2, ..., K \tag{3.45}$$

from which we can write the final expression of the Roothan-Hall equations:

$$\mathbf{FC} = \mathbf{SC}\varepsilon \tag{3.46}$$

$\mathbf{C}$ is the square $K \times K$ matrix of the expansion coefficients $C_{\mu i}$ while ε is the diagonal matrix of the orbitals' energies. $F_{\mu\nu}$ is the sum of two contributions, the first one

$$H_{\mu\nu}^{core} = \int d\vec{r}_1 \phi_\mu^*(1)h(1)\psi_\nu(1) \tag{3.47}$$

is the core Hamiltonian, while the second,$G_{\mu\nu}$ can be written in terms of matrix density $P_{\mu\nu}$:

$$P_{\mu\nu} = 2\sum_a^{\frac{N}{2}} C_{\mu a}C_{\nu a}^* \tag{3.48}$$

The Fock matrix depends on the density matrix, and so on the expansion coefficients. This leads to the fact that Roothan equations are nonlinear and it is necessary to use an iterative procedure to solve them. Furthermore it is possible to orthonormalize the equation loosing the dependence on the overlap matrix and make it a simple eigenvalue problem, obtaining the transformed Roothan equations:

$$\mathbf{F'C'} = \mathbf{C'}\varepsilon \tag{3.49}$$

From which we can evaluate C and then solve the iterative procedure.

3.1.9 SCF procedure

The SCF is defined as the iterative procedure to solve the electronic problem using the matrix Roothan equations. It is characterized by the following passages:

1. Characteristics of the molecule: nuclear coordinates, atomic numbers, number of electrons, basis set.
2. Calculation of the integrals: $S_{\mu\nu}, H_{\mu\nu}^{core}, (\mu\nu|\lambda\sigma)$.
3. Diagonalization of the overlap matrix $S_{\mu\nu}$ and evaluation of the transformation matrix.
4. Guess of the density matrix **P**.
5. Computation of the **G** matrix from density matrix and double integrals $(\mu\nu|\lambda\sigma)$.
6. Addition of **G** to $H_{\mu\nu}^{core}$ to obtain the Fock matrix.
7. Calculation of the transformed Fock matrix **F'**.
8. Diagonalization of **F'** to obtain **C'** and ε
9. Evaluation of **C** from **C'**
10. Computation of a new matrix density from **C**
11. If the new matrix density is the same of the previous one, the problem is solved. If it is not, the procedure is repeated from the point 5 with the new density matrix.
12. If the procedure reaches convergence, **C**, **P** and **F** are used to obtain all the quantities of interest.

3.1.10 Crystalline orbitals

Until now we have considered molecular problems, so single molecule calculations. Now we want to find a way to deal with crystals. In order to do that we have to introduce the concept of CO-LCAO (crystalline orbitals as a linear combination of atomic orbitals). As we have done for molecules, we can write crystalline orbitals as a linear combination of atomic orbitals:

$$\Psi_i = \sum_{\mu} C_{i\mu} \Phi_{\mu} \tag{3.50}$$

But in this case the translational invariance must be taken into account, so the atomic orbitals are written as Bloch's functions :

$$\Phi_\mu(\vec{r};\vec{k}) = \frac{1}{\sqrt{N}} \sum_{\vec{T}_n} e^{i\vec{k}\vec{T}_n} \psi_\mu^{\vec{T}_n}(\vec{r} - \vec{r}_\mu) \tag{3.51}$$

where $\psi_\mu^{\vec{T}_n}(\vec{r}-\vec{r}_\mu)$ is the μ_{th} atomic orbital referred to cell 0 and having origin in $\vec{r}_\mu$. These ψ_μ atomic obitals are built using gaussian contractions. In other words they constitute the basis set for the SCF procedure.

3.1.11 SCF for crystalline orbitals

Using Bloch's functions as basis set, we can rewrite the Fock matrix in the following way:

$$F_{\mu\nu}(\vec{k}) = \sum_{\vec{T}_n} e^{i\vec{k}\vec{T}_n} F_{\mu\nu}(\vec{T}_n) \tag{3.52}$$

In which $F_{\mu\nu}(\vec{T}_n)$ are the matrix elements of the Fock operator between the μ_{th} AO located in the 0 cell and the ν_{th} AO located in the $\vec{T}_n$ cell. So the Roothan-Hall equation becomes:

$$\mathbf{F}(\vec{k})\mathbf{C}(\vec{k}) = \mathbf{S}(\vec{k})\mathbf{C}(\vec{k})\mathbf{E}(\vec{k}) \tag{3.53}$$

Theoretically the equation can be solved for an infinite set of k values within the first Brillouin zone. Practically it is done only for a narrow range of k values. The Fock operator in the reciprocal space can be reduced in the following form:

$$F_{\mu\nu}(k) = \sum_m e^{i\vec{k}m} \left\langle \psi_\mu^0 | \hat{F} | \psi_\nu^m \right\rangle \tag{3.54}$$

It is the Fourier transform of the Fock operator from direct to reciprocal space. Now using this expression of $F(\vec{k})$ and using the Roothan-Hall equations previously written we can solve the same problem using SCF procedure also for crystals.

3.1.12 Basis-set

As previously seen, in order to do the iterative procedure and solve the electronic problem related to molecules or crystals it is necessary to define a starting basis set made by atomic orbitals. A reliable expression for them is the Slater-type orbital (STO) function:

$$\phi_i(\zeta, n, l, m; \vec{r}, \theta, \phi) = N r^{n-1} e^{-\zeta\vec{r}} Y_{ln}(\theta, \phi) \tag{3.55}$$

In which n,l,m are quantum numbers, N is a normaliaztion constant and ζ is the exponent of the STO. Due to the fact that these type of orbitals are very computationally expensive, specially for the calculation of double integrals, Gaussian-type orbitals (GTO) are used to express the basis set in which the Slater functions are substituted with gaussian ones:

$$g(\alpha, l, m, n; x, y, z) = Ne^{-\alpha x^2} x^l y^m z^n \tag{3.56}$$

Now n,l,m are not quantum numbers but simply exponents. Usually the single atomic orbital is expressed in terms of contraction, so linear combinations, of gaussian functions:

$$\psi_\mu = \sum_{p=1}^{L} d_{p\mu} g_p(\alpha_{p\mu}, \vec{r}) \tag{3.57}$$

where both coefficients and exponents are determined at the beginning of the calculation and they remain untouched during the SCF. The "*minimal*" basis set is the one in which the single ground-state orbital is described by a single contraction. A first evolution consists in the "*split-valence*" basis set in which a distinction between valence and core orbitals is introduced. The core ones are described by only one contraction, while the valence orbitals are described by more than one contraction. An example of these orbitals is the 6-31G in which we have 6 primitives to describe the core orbitals and two contractions, made respectively by 3 and 1 primitives, to describe the outer shell orbitals. Moreover it is possible to introduce polarization functions in which d orbitals on heavy atoms and p orbitals for hydrogen are introduced and are indicated with * (6-31G* or 6-31G**) or as 6-31G(d,p). They are inserted as non- contracted gaussian's primitives and they unavoidably increase the computational cost.

3.1.13 Principles of Density Functional Theory

Density Functional Theory (DFT) is very different from the Hartree-Fock theory because now the attention is shifted from the wavefunction on the electron density. If the wavefunction, in a generic system of N electrons, depends on 3N spatial coordinates the electron density will depend only on three variables (x,y and z); it's evident the convenience of a method based only on density. This theory consists in writing all the quantities of the fundamental state of a system as functionals of the electronic density $\rho(\vec{r})$. In particular, the energy of the ground state can be written as a functional of the density and it rapresents the

minimum possible energy if the density is exact. It is an exact theory beacause, as will be seen, it contains an exchange-correlation potential that theoretically, if its exact expression would be known, will bring to an exact result. But we have no information on how to build it, which results in the necessity of using some approximations.

3.1.14 Hohenberg-Kohn theorems

The following two theorems are considered as the cornerstone of the DFT theory, thanks to which it was possible to formulate a physico-mathematical theory based on electronic density.

Th. 1 The external potential $\nu(\vec{r})$ is uniquely determined by the electronic density, apart from an additive constant.

Th. 2 Be $\tilde{\rho}(r)$ a non negative density normalized by N. So $E_0 < E_\nu[\tilde{\rho}]$ where $E_\nu[\tilde{\rho}]$ is the functional of the state which external potential is determined from an electronic density of the fundamental state $\tilde{\rho}$. The ground-state density can be evaluated using a variational method that involves only the density

Writing the electronic hamiltonian in the following way:

$$\hat{\mathcal{H}}_{elec} = \hat{\mathcal{T}}_e + \hat{\mathcal{V}}_{ext} + \hat{\mathcal{U}}_{ee} \tag{3.58}$$

Due to these theorems, if it is true that the electornic density adapts itself to reach the minimal configuration due to the external potential, it is also true the contrary. So the nuclear configuration is determined from the density. This enables us to write the total energy of the system as a functional of the electronic density:

$$E[\rho] = T_e[\rho] + V_{ext}[\rho] + U_{ee}[\rho] \tag{3.59}$$

These terms are expectation values of the (58). Now, isolating the terms that don't depend on the external potential:

$$E[\rho] = V_{ext}[\rho] + F_{HK}[\rho] = \int \rho(\vec{r})\nu(\vec{r})dr + F_{HK}[\rho] \tag{3.60}$$

where:

$$F_{HK} = \big\langle \Psi[\rho] | \hat{\mathcal{T}}_e + \hat{\mathcal{U}}_{ee} | \Psi[\rho] \big\rangle \tag{3.61}$$

Ψ is the ground state wavefunction with density ρ, while F_{HK} is a *universal* functional that depends only on electronic density and the equation (60) is an exact rapresentation of the system. Previous theorems give the possibility to compute exactly every stationary quantomechanical parameter. The main issue is that the F_{HK} functional is an extremely complex physical quantity, for which the exact form has not been determined yet.

3.1.15 Kohn-Sham method

It is possible to rewrite the total energy functional in the following way:

$$E[\rho] = T_e[\rho] + V_{ext}[\rho] + \frac{1}{2}\int\int \frac{\rho(\vec{r})\rho(\vec{r}')}{|\vec{r}-\vec{r}'|}d\vec{r}d\vec{r}' + E_{xc}[\rho] \tag{3.62}$$

In which U_{ee} is splitted in two terms. The frist one is the classical energy repulsion term between electrons while the second is the exchange-corelation term in which non classical contributions are taken into account. The solution of the problem was given by the Kohn-Sham method that is based on substituting the real system with one formed by independent electrons, characterized by the same density of the real system. The kinetic energy term of interacting particles was substituted with a non interactive one. This system is taken with the same electronic density of the interacting system but the electrons are considered independent. The part of the kinetic energy that considers the electron-electron interaction is embedded in the exchange-correlation term. So total energy functional becomes:

$$E_{KS}[\rho] = T_0[\rho] + V_{ext}[\rho] + U_{cl}[\rho] + E_{xc}[\rho] \tag{3.63}$$

In the E_{xc} is contained the only one approximation of the density functional theory, because an exact exchange-correlation functional is unknown. Various type of approximations have been proposed but they cannot be used precisely for all the chemical systems. We can introduce the hamiltonian of the non-interactive system:

$$\hat{\mathcal{H}}_0 = \sum_{i=1}^{N}\left(-\frac{\nabla_i^2}{2} + \nu_{eff}(\vec{r}_i)\right) \tag{3.64}$$

In which the eigenstates can be expressed in the form of Slater determinant where fictitious Kohn-Sham orbitals are present ϕ_i^{KS} with electronic density $\rho(r) = \sum_{i=1}^{N}|\phi_i^{KS}(\vec{r})|^2$. Applying a variational method on E_{KS}, the following equation can be derived:

$$\nu_{eff}(r) = \nu(\vec{r}) + \int \frac{\rho(\vec{r}')}{|\vec{r}-\vec{r}'|}d\vec{r}' + \mu_{xc}[\rho(\vec{r})] \tag{3.65}$$

in which $\mu_{xc}[\rho(\vec{r})] = \frac{\delta E_{xc}[\rho(\vec{r})]}{\delta\rho(\vec{r})}$. So at the end we can write the Kohn-Sham selfconsistent equations:

$$\left\{-\frac{\nabla^2}{2} + \nu_{eff}(\vec{r})\right\}\phi_i(\vec{r}) = \varepsilon_i\phi_i(\vec{r}) \tag{3.66}$$

We can use the same iterative procedure that we have used in (18) to solve this equation. So using the orbitals' energies the total energy can be expressed in the following way:

$$E_{KS}[\rho] = \sum_{i}^{N} \varepsilon_i - \frac{1}{2}\int\int \frac{\rho(\vec{r})\rho(\vec{r}')}{|\rho(\vec{r}) - \rho(\vec{r}')|} d\vec{r}d\vec{r}' + \left\{ E_{xc}[\rho] - \int \rho(\vec{r})\mu_{xc}[\rho]d\vec{r} \right\} \tag{3.67}$$

These equations have a form similar to HF equations, so they are useful to be used in a calculation code. But, differently from the Hartree-Fock equations, in the KS ones the ν_{eff} takes into account both exchange and correlation. So using a system of N non-interacting electrons but with the same electronic density of the interacting one allows to solve in an exact way the many body Schrödinger equations. For what concerns the KS orbitals we can say that their meaning is only related to the associated electronic density $\rho(\vec{r})$.

3.1.16 E_{xc} functionals

The exchange-correlation functional can be written as:

$$E_{xc}[\rho] = \frac{1}{2}\int\int \frac{\rho(\vec{r})\rho(\vec{r}')}{|\vec{r} - \vec{r}'|}[\tilde{g}(\vec{r}, \vec{r}') - 1]d\vec{r}d\vec{r}' \tag{3.68}$$

In which $\tilde{g}(\vec{r}, \vec{r}')$ is the two-body direct correlation function, called also pair correlation function, averaged depending on the force of the electronic contribution. Now defining the exchange-correlation hole $\tilde{\rho_{xc}}(\vec{r}, \vec{r}') = \rho(\vec{r}')[\tilde{g}(\vec{r}, \vec{r}') - 1]$, it is obtained that :

$$E_{xc}[\rho] = \frac{1}{2}\int\int \frac{\rho(\vec{r})\tilde{\rho_{xc}}(\vec{r}, \vec{r}')}{|\vec{r} - \vec{r}'|} d\vec{r}d\vec{r}' \tag{3.69}$$

Written in this way, E_{xc} rapresents the interaction between the electronic charge distribution and the electronic charge distribution affected by the exchange-correlation effects. The simpler approximation that can be done on electronic density is the *Local Density Approximation* (LDA) in which a locally homogeneous system is considered, so the electronic density is approximated to the one of an homogeneous electron gas. In these terms the exchange-correlation functional becomes:

$$E_{xc}^{LDA}[\rho] = \int \rho(\vec{r})\varepsilon_{xc}^{LDA}[\rho]d\vec{r} \tag{3.70}$$

In which $\varepsilon_{xc}^{LDA}[\rho] = \int \frac{\tilde{\rho}_{xc}^{LDA}(\vec{r},\vec{r}')}{|\vec{r}-\vec{r}'|} d\vec{r}$ is the exchange-correlation energy. It is a very strong approximation, and should be limited to systems

with slowly varying electronic distribution. Perdew demonstrated that since LDA is based on a real physical system, it works not so bad also with molecules. Moreover it is a real *first principles* approximation because it doesn't depend on any empirical parameter. We can reformulate the same approximation considering also the spin, obtaining the LSDA (Local Spin Density Approximation). An evolution of the LSDA approximation is the GEA(*Gradient Expansion Approximation*) that consists on a Taylor expansion of the E_{xc} functional. The GGA (*Generalized Gradient Approximation*) is a particular type of GEA in which the expansion is truncated at the first order:

$$E_{xc}[\rho] = \int f[\rho, \nabla\rho] d\vec{r} \tag{3.71}$$

The main strategy of this approach is to separate the term of exchange with that of correlation: $E_{xc}[\rho] = E_x[\rho] + E_c[\rho]$. The most important exchange functionals are B88, PW86 and PW91 while among the most important correlation functionals there are the LYP, PW86 and the PW91. It can be noticed that all these functionals, apart from the PW91, contain empirical parameters fitted on experimental data. So DFT cannot be defined a real *ab-initio* method, because the functional depends strongly on these empirical parameters.

3.1.17 PBE functional and hybrid methods

The PW91 functional was elaborated by Perdew and Wang in order to cancel the empirical dependence of the functional and make DFT a true *ab-initio* method. The procedure adopted by the two scientists was inspired by GEA, but the Taylor expansion in this case was expressed in the real space in order to delete all the terms responsible for the failure of the GEA itself. With this method, called *Real-Space Cutoff*, Perdew was able to create a functional that respected all the properties of an E_{xc} functional and moreover to make it unaffected by empirical parameters. This approximation, for a slowly variable electron density, tends to the LDA that is understandable. But the other functionals, also the LYP one, don't take into account this fact going away from the physical meaning of the functionals. With this functional the DFT can be considered a true *ab-initio* method, at least for the correlation part. The exchange part still contains empirical parameters beacuse it is derived from the B88. So Starting from this formulation, Perdew, Burke and Ehrenzorf built the PBE functional that nowadays is one of the most developed and used functional. The GGA functionals are not satisfying for what concern the exchange part. This fact brought to the formulation of hybrid functionals in which the exchange part

is substituted by the exact exchange. The method is based on the *Adiabatic Connection* formula :

$$E_{xc} = \int_0^1 E_{xc,\lambda} d\lambda \tag{3.72}$$

In this way the exchange-correlation functional is rapresented with only one expression that is a function of the coupling constant λ. If $\lambda = 1$ the system is considered completely correlated while for $\lambda = 0$ th correlation is 0. The functionals that are built in this way are called "hybrid". Several hybrid schemes have been proposed and the most widely used include three empirical parameter to rule the mixing of HF exchange and DF exchange and correlation:

$$E_{xc}^{ACM3} = E_{xc}^{LSD} + a_1\big(E_x^{HF} - E_x^{LSD}\big) + a_2 \Delta E_x^{GGA} + a_3 \Delta E_c^{GGA} \tag{3.73}$$

In this context, one of the most important three-parameters hybrid functional is the B3LYP one. But in vibrational calculation it tends to overestimate the frequency values, so it's necessary a scaling procedure of the obtained results. More recently, Becke has suggested that just one coefficient is sufficient to rule the HF/DF exchange ratio according to:

$$E_{xc}^{ACM1} = E_{xc}^{GGA} + a_1\big(E_x^{HF} - E_x^{GGA}\big) \tag{3.74}$$

These methods (usually referred to as ACM1) are quite successful. Perdew and co-workers have next shown that the optimum value of a_1 coefficient can be adjusted *a priori* taking into account that fourth-order perturbation theory is sufficient to get accurate numerical results for molecular systems. This leads to a family of adiabatic connection functionals thereafter referred to as ACM0 with the same number of adjustable parameters as their GGA's constituents:

$$E_{xc}^{ACM0} = E_{xc}^{GGA} + \frac{1}{4}\big(E_x^{HF} - E_x^{GGA}\big) \tag{3.75}$$

So using the PBE functional and HF exchange with predefined coefficients it is possible to exploit a parameter free density functional approach that is rapresented by the famous PBE0 hybrid functional. It is probably the best functional currently available which couples a good accuracy for molecular structures and properties along the whole periodic table to a direct connection to physical principles. It will be also the functional adopted for our computational calculations.

3.2 Theory of vibrations and Raman scattering for molecules and crystals

The following chapter will treat the basic theory of vibrations, passing through the concept of normal coordinates both for crystals [32] and molecules [33]. Then principles of Raman scattering, from the classical and quantum point of view, will be presented and discussed [34].

3.2.1 The harmonic approximation and classical vibrations for diatomic molecule

To deal with vibrations, as in the electronic case, we have to do some approximations. The first one is the Harmonic approximation. It is used to simplify the expression of the interatomic potential. It is based on the fact that for small amplitude vibrations it is possible to make a Taylor expansion, truncated at the second order, of the potential around the equilibrium positions of nuclei:

$$V(R) \approx V(R_0) + \left(\frac{dV}{dR}\right)_{R=R_0} (R - R_0) + \frac{1}{2}\left(\frac{d^2V}{dR^2}\right)_{R=R_0} (R - R_0)^2 \quad (3.76)$$

At equilibrium position the linear term is 0, so it becomes:

$$V(R) \approx V(R_0) + \frac{1}{2}k(R - R_0)^2 \quad (3.77)$$

where we can define the so called *force constant* k as:

$$k = \left(\frac{d^2V}{dR^2}\right)_{R=R_0} \quad (3.78)$$

The force along the coordinate R is proportional to k and to the displacement, as for a simple spring:

$$f(r) = -\frac{dV}{dR} = -k(R - R_0) = -k\Delta R \quad (3.79)$$

Solving the classical vibrational model for the diatomic molecule, in which the two nuclei are considered as simple masses connected by springs, we obtain an expression for the variation in time of the bond length:

$$R(t) = R_0 + A\sin(\omega t + \phi) \quad (3.80)$$

In which the angular frequency is:

$$\omega = \sqrt{\frac{k}{\mu}} \quad (3.81)$$

and $\mu = \frac{m_1 m2}{m_1+m_2}$ is the so called reduced mass. Usually the angular frequency is expressed in terms of cm^{-1} using the linear dispersion relation of light:

$$\bar{\nu} = \frac{\nu}{c} = \frac{\omega}{2\pi} = \frac{1}{2\pi c}\sqrt{\frac{k}{\mu}} \tag{3.82}$$

The oscillatory trend of the solution for the diatomic molecule is around the equilibrium bond length R_0 where the amplitude of the oscillation is given by the constant A.

3.2.2 Classical theory of vibrations in polyatomic molecules

To deal with this problem we consider a system with many degrees of freedom within the harmonic approximation. The approach consists in introducing a certain coordinate system using which it is possible to reduce the many body quantum vibrational problems in terms of a set of independent one dimensional quantum oscillators. We can write the classical Hamiltonian associated to this problem:

$$H = T + V = \frac{1}{2}\sum_i m_i \dot{u}_i^2 + \frac{1}{2}\sum_{ij} u_i k_{ij} u_j \tag{3.83}$$

The kinetic energy term is a diagonal quadratic form, so it is expressed as a sum of independent terms. While the potential energy term in general couples all pairs of displacement through the $k_{ij} = \left(\frac{\partial^2 V}{\partial x_i \partial x_j}\right)_{x_i = x_i^0}$ coefficients. The aim is to find an equivalent formulation but in which the Hamiltonian becomes fully diagonal. The Hamiltonian can be written also in terms of matrices in the following way:

$$\mathbf{H} = \frac{1}{2}\dot{\bar{\xi}}^t\dot{\xi} + \frac{1}{2}\dot{\bar{\xi}}^t\mathbf{W}\dot{\xi} \tag{3.84}$$

where W is defined as :

$$\mathbf{W} = \mathbf{M}^{-1/2}\mathbf{K}\mathbf{M}^{-1/2} \tag{3.85}$$

and expresses the potential V as a quadratic form with respect to the set of mass-weighted coordinates ξ. $\mathbf{K}$ and $\mathbf{M}$ rapresent respectively the matrix made by the spring constants and the matrix associated to the masses of nuclei. Now considering the diagonal rapresentation of $\mathbf{W}$:

$$\mathbf{W}\mathbf{L} = \mathbf{L}\Lambda \tag{3.86}$$

it is possible to rewrite the Hamiltonian as:

$$\mathbf{H} = \frac{1}{2}\dot{\bar{\xi}}^t \mathbf{L}\mathbf{L}^t \dot{\bar{\xi}} + \frac{1}{2}\dot{\bar{\xi}}^t \mathbf{L}\mathbf{\Lambda}\mathbf{L}^t \dot{\bar{\xi}} \tag{3.87}$$

Introducing a new set of coordinates called *normal coordinates* $\bar{q} = \mathbf{L}^t \bar{\xi}$, it is possible to write the Hamiltonian as a diagonal form both for the kinetic and the potential energy:

$$\mathbf{H} = \frac{1}{2}\dot{\bar{q}}^t \dot{\bar{q}} + \frac{1}{2}\dot{\bar{q}}^t \mathbf{\Lambda} \dot{\bar{q}} \tag{3.88}$$

where eigenvalues Λ rapresent squares of angular frequencies ω_i^2. Writing the equations of motion for normal coordinates:

$$q_i(t) = q_i^0 sin(\omega_i t + \psi_i \tag{3.89}$$

it is possible to write the displacements in terms of normal coordinates q:

$$\bar{u} = (\mathbf{M}^{-1/2}\mathbf{L})\bar{q} \tag{3.90}$$

Normal coordinates are fundamental for what concerns the relationship between chemical structure and specific vibration transitions. We will see in the following subsection that it is possible to correlate single normal modes with associated vibrational wavefunctions in a one-to-one manner. To visualize the normal modes the idea is to rapresent an animation of the atoms' motion for a selected i-th normal mode.

3.2.3 Quantum theory for vibrations in a polyatomic molecule

It is possible to write the quantum Hamiltonian for a polyatomic molecular system as :

$$\hat{H} = \hat{T} + \hat{V} = \sum_i \left[-\frac{\hbar^2}{2}\frac{\partial^2}{\partial q_i^2} + \frac{1}{2}\omega_i^2 q_i^2 \right] \tag{3.91}$$

It is convenient to use a dimensionless form of the Hamiltonian. Then defining the so called dimensionless position operator $t_i = q_i\sqrt{\omega_i \hbar}$ we obtain:

$$\hat{H} = \sum_i \frac{\hbar\omega_i}{2}\left[\frac{\partial^2}{\partial t_i^2} + t_i^2\right] = \sum_i \hbar\omega_i \hat{h}(t_i) \tag{3.92}$$

The eigenvalues and eigenvectors of the one-dimensional quantum oscillator described by the Hamiltonian $\hat{H}_{vib}(t_i) = \hbar\omega_i \hat{h}(t_i)$ are:

$$\hat{H}_{vib}(t_i)|n_i> \; = \hbar\omega_i \left(n_i + \frac{1}{2}\right)|n_i> \tag{3.93}$$

In which n_i are the eigenvectors of the vibrational problem that are related to normal coordinates and so to displacements. It is possible to show that for a many body Hamiltonian given by the sum of independent one-body Hamiltonians, the total wavefunction of the system is given by the product of the eigenfunctions of each one-body Hamiltonian and the total energy eigenvalue is the sum of the one-body eigenvalues:

$$\hat{H}\phi(t_1, t_2, t_3, ..., t_M) = E\phi(t_1, t_2, t_3, ..., t_M) \tag{3.94}$$

$$\phi(t_1, t_2, t_3, ..., t_M) = \prod_{i=1}^{M} \phi_{n_i}(t_i) \tag{3.95}$$

$$E = \sum_{i=1}^{M} \hbar\omega\left(n_i + \frac{1}{2}\right) \tag{3.96}$$

M is the number of vibrational normal modes obtained as eigensolutions of the secular equation. Usually adopting Cartesian displacements to describe molecular motions, three translations of the molecule as a rigid body and three rotations can be identified. Therefore true vibrations are $M = 3N - 6$. Rototranslations are associated to solutions with $\omega = 0$.

3.2.4 Vibrations in solids, Born-Von Karman model

Thanks to the adiabatic approximation we assume the existence of a vibrational potential energy U_e which is a function of displacements of nuclei with respect to their official positions in the crystal. From now on we will use the Born and Huang notation:

$$r\binom{p}{n} = R_n + r_p = n_1a_1 + n_2a_2 + n_3a_3 + r_p \tag{3.97}$$

$r\binom{p}{n}$ is the position with respect to the origin of the nucleus p with mass m_p located in the primitive cell (made by s atoms, that is the basis). The displaments of atomic nuclei will be :

$$u\binom{p}{n} = r'\binom{p}{n} - r\binom{p}{n} \tag{3.98}$$

where r' rapresents the instantaneous position of the nucleus (p n) that fluctuates due to vibrational motions. If we suppose that thermal motions only slightly perturb the periodic structure, the potential

energy can be expanded in a series arrested at the second order:

$$U_\nu = \frac{1}{2}\sum_{nn'}\sum_{pp'}^{1,s}\sum_{jj'}^{1,3}\Phi_{jj'}\begin{pmatrix}p & p'\\ n & n'\end{pmatrix}u_j\begin{pmatrix}p\\ n\end{pmatrix}u_{j'}\begin{pmatrix}p'\\ n'\end{pmatrix} \tag{3.99}$$

In which Φ is the interatomic force constants tensor defined as:

$$\Phi_{jj'}\begin{pmatrix}p & p'\\ n & n'\end{pmatrix} = \frac{\partial^2 U_\nu}{\partial u_j\binom{p}{n}\partial u_{j'}\binom{p'}{n'}} \tag{3.100}$$

The sum nn' must be extended to all N crystal cells. Physically $E_\alpha^{(e)}(u)+V_{nn} = U_\nu^\alpha(u)$ where $E_\alpha^{(e)}(u)$ is the electronic energy (eigenstate of the electronic problem) for example of the ground state. So this is still the harmonic approximation, but expressed for crystalline solids. We will begin with a classical treatment for vibrations in solids and then we will move to quantum theory. Using the *Lagrange equations* we can derive the Newtonian dynamic equations,that is a system of 3sN equations in 3sN variables $u_j\binom{p}{n}$

$$m_p\ddot{u}\begin{pmatrix}p\\ n\end{pmatrix} = -\sum_{n'}\sum_{p'}^{1,s}\Phi\begin{pmatrix}p & p'\\ n & n'\end{pmatrix} : u\begin{pmatrix}p'\\ n'\end{pmatrix} \tag{3.101}$$

where : is a rows by column product. Now, thanks to translational symmetry of the crystal it is possible to write n'=n+h, in which $h = T_h$ is a lattice translation. So :

$$\Phi\begin{pmatrix}p & p'\\ n & n'\end{pmatrix} = \begin{pmatrix}p & p'\\ n & n+h\end{pmatrix} = \Phi\begin{pmatrix}pp'\\ h\end{pmatrix} \tag{3.102}$$

and the dynamic equations become:

$$m_p\ddot{u}\begin{pmatrix}p\\ n\end{pmatrix} = -\sum_{h}\sum_{p'}^{1,s}\Phi\begin{pmatrix}pp'\\ h\end{pmatrix} : u\begin{pmatrix}p'\\ n+h\end{pmatrix} \tag{3.103}$$

Where the sum over h involves all the N lattice translations which join the cell n with the other ones. Applying periodic boundary conditions, as in the case of electrons:

$$u\begin{pmatrix}p\\ n+(N_j-1)a_j\end{pmatrix} = \begin{pmatrix}p\\ n\end{pmatrix} \tag{3.104}$$

and remembering that the fundamental soultions should satisfy Bloch theorem:

$$\begin{pmatrix}p\\ n\end{pmatrix} = \begin{pmatrix}p\\ 0\end{pmatrix}e^{iqn} \tag{3.105}$$

It is obtained that to every lattice wave at least one wavevector q is associated such that previous equation is satisfied. As in the case of electrons (k vectors), the set of q vectors is that composed by the N vectors contained in the first Brillouin zone. In this way we have reduced the set of 3sN dynamic equations to a set of 3s equations which describes the vibrations of the s nuclei contained in the cell 0. At this point we can introduce the dynamic matrix:

$$\mathbf{D}\begin{pmatrix} pp' \\ q \end{pmatrix} = \sum_h \frac{\Phi\binom{pp'}{h}}{\sqrt{m_p m_{p'}}} e^{iqh} \tag{3.106}$$

as the *discrete Fourier Transform* of interatomic force constant tensor. Now substituting the expression of the dynamic matrix inside the equation of motion and searching for elementary harmonic solutions as:

$$u(p,q) = \frac{1}{\sqrt{Nm_p}} Q(q) e(p,q) e^{-i\omega(q)t} \tag{3.107}$$

where e(p,q) is the *polarization vector*, we obtain the homogeneous system of linear algebraic equations (eigenvalue problem):

$$\sum_{j'}^{1,3} \sum_{p'}^{1,s} \left\{ D_{jj'}\begin{pmatrix} pp' \\ q \end{pmatrix} - \omega^2(q)\delta_{jj'}\delta_{jj'} \right\} e_{j'}(p',q) = 0 \tag{3.108}$$

For any q, the squares of the natural frequencies are the eigenvalues of the dynamic matrix while the polarization unit vectors are its eigenvectors. Solving the following equation:

$$det\left\{ D_{jj'}\begin{pmatrix} pp' \\ q \end{pmatrix} - \omega^2(q)\delta_{jj'}\delta_{jj'} \right\} = 0 \tag{3.109}$$

it is possible to compute the eigenvalues. For any value of the vector q, that are N in the first Brillouin zone, the equation has 3s countable solutions $\omega^2(q) = \omega_\alpha^2(q)$ characterized by a *branch index* α. Solution functions $\omega_\alpha^2 = \omega_\alpha^2(q)$ are called dispersion relations. Considering a primitive cell made by s nuclei, there are 3s degrees of freedom. Among them 3 refer to the center of mass of the basis, called *acoustic branches*, while the other 3s-3 refer to internal motion of the basis, the so called *optical branches*. The term acoustic comes from the fact that, when $q \to 0$, acoustic motions coincide with the macroscopic elastic waves that propagate at the speed of sound. Instead the term optical derives from the fact that the corresponding modes can have a flactuating electric dipole determining the optical infrared absorption in the crystal or

can have associated a fluctuation of electrical polarizability determining, in the crystal, the vibrational Raman scattering of photons. We can now express the most general solution of the dynamic equations as the following linear combination of all lattice waves:

$$u\binom{p}{n} = \frac{1}{\sqrt{Nm_p}} \sum_{q \in BZ} \sum_{\alpha}^{1,3s} Q(q,\alpha) e(p,q,\alpha) e^{iqn} e^{-i\omega_\alpha(q)t} \tag{3.110}$$

Introducing the 3sN normal coordinates $\xi(q,\alpha)e(p,q,\alpha)e^{iqn}$ and substituting these solutions inside the vibrational Hamiltonian it is possible to obtain:

$$H_\nu = \frac{1}{2} \sum_{q \in BZ} \sum_{\alpha}^{1,3s} \left\{ |P(q,\alpha)|^2 + \omega_\alpha^2(q) |\xi(q,\alpha)|^2 \right\} \tag{3.111}$$

in which $P(q,\alpha)$ are the kinetic momenta conjugated to normal coordinates. So the vibrational behaviour of the crystal is equivalent to that of a set of 3sN independent harmonic oscillators with frequencies $\omega_\alpha^2(q)$. Collective motions $\xi(q,\alpha)$ are harmonic motions, while motion of a single nucleus is not. For this reason they are called collective coordinates and their energy quanta $\hbar\omega_\alpha(q)$ behave as Bose particles, or *quasi-particles* called phonons. Infact, writing :

$$\hat{P}_{q,\alpha} = -i\hbar \frac{\partial}{\xi_{q,\alpha}} \tag{3.112}$$

it's possible, substituting this operator in the expression of the Hamiltonian, to switch immediately to a quantum description of lattice vibrations. In the 3D general case each oscillator with normal coordinate $\xi(q,\alpha)$ owns a frequency $\omega(q,\alpha)$ and a polarization unit vector $e(q,\alpha)$ and can assume only discrete energy levels:

$$E_n(q,\alpha) = \left(n(q,\alpha) + \frac{1}{2} \right) \hbar\omega(q,\alpha) \tag{3.113}$$

$n(q,\alpha)$ rapresents the *phonon occupation number* associated to the mode (q,α).

3.2.5 Infrared (IR) absorption spectroscopy

Perturbation theory and dipole operator Infrared spectroscopy is a particular optical spectroscopy in which quantum transitions between different vibrational states are observed. The transition probability between two stationary states ,$|i>$ and $|f>$, promoted by a time

dependent perturbation written in the form of $\hat{H}'(t) = \hat{V}\cos(\omega_0 t + \varphi)$, with the $\hat{V}$ operator being time independent, is given by:

$$P_{i\to f} = \frac{2\pi}{\hbar}\left|\left\langle i|\hat{V}|f\right\rangle\right|^2 \delta(E_f - E_i - \hbar\omega_0) \tag{3.114}$$

The previous equation rapresents the so called Fermi golden rule, $|i>$ and $|f>$ are known eigenstates of a given Hamiltonian $\hat{H}$ for which $\hat{H}'$ can be taken as a weak enough perturbation. The intensity of the absoprtion will be obviously proportional to the transition probability. Energy conservation, expressed inside the delta, is a necessary but not sufficient condition for the transition to occur. Selection rules are determined by the possible value of the transition moment operator of the perturbation between the two states involved in the transition, $\left\langle i|\hat{V}|f\right\rangle$. For a collection of charges forming the molecule and neglecting magnetic effects, the perturbative Hamiltonian operator $\hat{H}'$(t) which describes the interaction of the molecule with the external electric field $E(t)$ is given by:

$$\hat{H}'(t) = \sum_I -E_0(eZ_I R_I)\cos(\omega_0 t+\varphi) + \sum_i E_0(er_i)\cos(\omega_0 t+\varphi) \tag{3.115}$$

In the previous equation the sum over I rapresents the sum over all the nuclei while the sum over i rapresents the sum over the electrons. Since $E_0 cos(\omega_0 t + \varphi) = E(t)$, we can write:

$$\hat{H}'(t) = -\left[\sum_I eZ_I R_I - \sum_i er_i\right]E(t) = -\hat{\mu}E(t) \tag{3.116}$$

where μ is the dipole operator. So the time-independent part of the operator $\hat{H}'$(t) is:

$$\hat{V} = -\hat{\mu}E_0 \tag{3.117}$$

Therefore the evaluation of the matrix element showing in Fermi golden rule is reduced to:

$$\left\langle i|\hat{V}|f\right\rangle = -\left\langle i|\hat{\mu}|f\right\rangle E_0 \tag{3.118}$$

The projection of the transition dipole moment $\left\langle i|\hat{\mu}|f\right\rangle$ on the polarization vector of the incoming optical field governs photon absorption, which drives the quantum transition of the molecule from state $|i>$ to state $|f>$.

Vibrational transitions The case where the initial and final quantum states of the molecule are two different vibrational states of the

same electronic states is the situation occurring in IR absorption spectroscopy. The matrix elements of the transition operator for the $i \to f$ quantum transition can be written in the following way:

$$\langle\langle i|\hat{\mu}|f\rangle\rangle = \langle g| \prod_j (0_j|[\hat{\mu}_n + \hat{\mu}_e] \prod_k |n_k)|g\rangle = \prod_j (0_j|\langle g|\hat{\mu}_n + \hat{\mu}_e|g\rangle \prod_k |n_k) \tag{3.119}$$

in which $\langle g|\hat{\mu}_n + \hat{\mu}_e|g\rangle = \mu(\vec{R})$ rapresents the expectation value of the molecular dipole due to charge distribution of both electrons and nuclei in the ground electronic state, that is a function of the set of atomic positions ($\vec{R}$). $(0_j|$ is the generic initial vibrational state while $|n_k)$ is the generic vibrational final state. As we explained above, the set of atomic positions can be expressed in terms of normal coordinates $\vec{q}$; therefore also $\mu(\vec{q})$ can be expressed as a function of normal coordinates. As a first approximation, we can express the dependenece of the expectation value of the dipole as a function of the molecular geometry as a Taylor expansion arrested at the first order:

$$\mu(q) \approx \mu_0 + \sum_j \left(\frac{\partial \mu}{\partial q_j}\right)_0 q_j \tag{3.120}$$

Substituting this relation inside the (119) and doing the calculations we can write the final result:

$$\langle\langle i|\hat{\mu}|f\rangle\rangle = \sum_s \left(\frac{\partial \mu}{\partial q_s}\right)_0 (0_s|q_s|n_s) \prod_{j \neq s} (0_j|n_j) \tag{3.121}$$

Observing the equation above, we can see that the value of the static molecular dipole at equilibrium does not influence IR absorption for a purely vibrational transition. The specific normal mode, characterized by a certain normal coordinate, will be IR active if there is a variation of the dipole moment with resepct to that normal coordinate. Finally the IR absorbance (A_k) of a given one-quantum transition associated to mode k is given by:

$$A_k \propto \frac{1}{2}\left(\frac{\hbar}{\omega_k}\right)\left(\frac{\partial \mu}{\partial q_k}\right)_0^2 \tag{3.122}$$

With ω_k equal to the freqeuncy associated to the quanta of the specific normal mode.

3.2.6 Raman scattering

Classical Theory of Raman scattering: Basic Model

The classical theory of Raman scattering is based on the idea that the electromagnetic field of the incident light induces in the system a time

dependent dipole moment $M(t) = \sum_i e_i r_i(t)$ where e is the electron's charge and r is the position vector. Let $E = E_0 \cos \omega_L t$ be the electric vector of the incident light. For the dipole moment M induced by E we write:

$$M = \alpha E + \frac{1}{2}\beta E^2 + ... \tag{3.123}$$

in which α is the electronic polarizability and β is a third rank tensor, called hyperpolarizability that we will neglect in this treatment. In general α is a second-rank tensor, but we will consider only the isotropic system's case where M is parallel to E. α depends on the electric charge distribution ρ of the system ($\alpha = \alpha(\rho)$). If the atomic configuration changes during the vibration, ρ and hence α will also change. Considering a diatomic molecule and assuming an electric field parallel to its axis, ρ and α will change during the vibration. For sufficiently small displacements of the nuclei from their equilibrium positions, α will change linearly with the normal coordinate $Q = \sqrt{\mu}(u_2 - u_1)$. μ is the reduced mass and u_2 and u_1 are the atoms' 1 and 2 displacements. Expanding α in a Taylor series we obtain:

$$\alpha_0 + \left(\frac{\partial \alpha}{\partial Q}\right)_0 Q + \frac{1}{2}\left(\frac{\partial^2 \alpha}{\partial Q^2}\right)_0 Q^2 \tag{3.124}$$

The *first-order Raman effect* is determined by the term linear in Q, the *second-order Raman effect* by the term quadratic in Q and so on. We will only refer to first-order Raman scattering. If the molecule vibrates with frequency ω_s we have $Q = Q_0 cos\omega_s t$ and obtain

$$\alpha(t) = \alpha_0 + \left(\frac{\partial \alpha}{\partial Q}\right)_0 Q_0 cos\omega_s t \tag{3.125}$$

Substituting (112) in (110) and using known trigonometric formulae the following expression can be obtained:

$$M(t) = \alpha cos\omega_L t + b[cos(\omega_L - \omega_s)t + cos(\omega_L + \omega_s)t] \tag{3.126}$$

where:

$$\alpha = \alpha_0 E_0, \qquad b = \frac{1}{2}\left(\frac{\partial \alpha}{\partial Q}\right)_0 Q_0 E_0 \tag{3.127}$$

The equation shows that the induced dipole moment M vibrates not only with the frequency ω_L of the incident light, but also with the frequencies $\omega_L \pm \omega_s$. These latter frequencies arise from the modulation of the electronic polarizability α by the vibration of the atoms. The classical radiation theory of an oscillating dipole is based on the description of the electromagnetic field produced by an accelerated charge

employing Maxwell's equation. The intensity of radiation emitted by the dipole moment M(t) into the solid angle $\mathrm{d}\Omega = \sin\theta d\theta d\phi$ is given by:

$$dI(t) = \frac{d\Omega}{4\pi c^3}\sin^2\theta|\ddot{M}(t)|^2 \tag{3.128}$$

Integrating over θ and ϕ and inserting the expression of M(t) in the (114) we obtain:

$$I(t) = AE_0^2\big[k_0^2\cos^2\omega_L t + k_1^2\cos^2\big(\omega_L - \omega_s\big)t + k_2^2\cos^2\big(\omega_L + \omega_s\big)t\big] + crossterms \tag{3.129}$$

where:

$$k_0^2 = \alpha_0^2\omega_L^4 \tag{3.130}$$

$$k_1^2 = \frac{1}{4}\left(\frac{\partial\alpha}{\partial Q}\right)_0^2 Q_0^2(\omega_L - \omega_s)^4) \tag{3.131}$$

$$k_2^2 = \frac{1}{4}\left(\frac{\partial\alpha}{\partial Q}\right)_0^2 Q_0^2(\omega_L + \omega_s)^4) \tag{3.132}$$

Neglecting the cross terms, we expect that scattered light will have peaks at the frequencies ω_L and $\omega_L \pm \omega_s$. This can be demonstrated calculating the frequency dependence of the scattered light, the power spectrum, obtained as a fourier transform of M(t). Making the calculation we obtain:

$$P(\omega) = \pi AE_0^2\big\{k_0\delta\big(\omega - \omega_L\big) + k_1^2\delta\big[\omega - \big(\omega_L - \omega_s\big)\big] + k_2^2\delta\big[\omega - \big(\omega_L + \omega_s\big)\big]\big\} \tag{3.133}$$

The first term is the power scattered per unit solid angle at the frequency ω_L of the incident radiation and is known as *elastic scattering* or *Rayleigh scattering*. The second and the third terms rapresent the *inelastic* or *Raman scattering* that consists in a radiation scattered at the Stokes frequency $\omega_L - \omega_s$ and at the anti-Stokes frequency $\omega_L + \omega_s$ respectively. Each term is proportional to k_i^2 which, at the same time, is proportional to the square of the polarizability derivative with respect to the normal coordinate. It means that if this derivative is 0, the Stokes and anti-Stokes peaks disappear for that specific normal mode; this fact rapresents the so called selection rules for Raman scattering. The classical theory correctly predicts the existence of the Stokes and anti-Stokes lines, as can be seen Fig. 3.1, but it leads to an incorrect ratio of their intensities. Infact, from the equations above, the ratio between the Stokes and anti-Stokes peaks should be:

$$\frac{I_{Stokes}}{I_{anti-Stokes}} = \frac{\big(\omega_L - \omega_s\big)^4}{\big(\omega_L + \omega_s\big)^4} \tag{3.134}$$

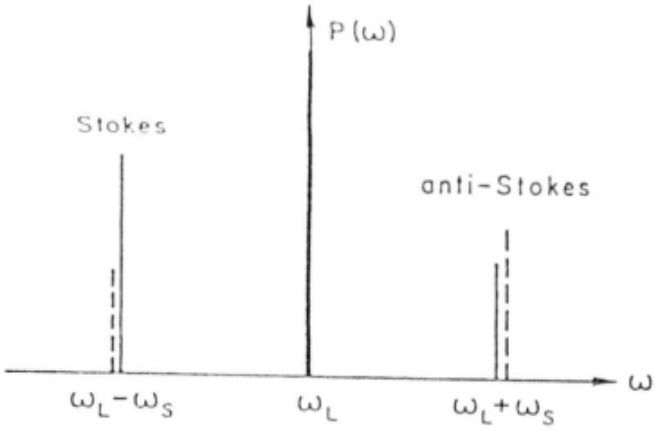

Figure 3.1: Stokes and anti-Stokes lines; dotted lines come from the classical theory. [34]

which is certainly less than unity, whereas experimentally it is found that the Stokes lines are more intense than the anti-Stokes ones. This error is corrected by using a quantum theory for the interpretation of the Raman effect. We have already said that in general the direction of the induced dipole moment M does not coincide with the direction of the electric field E. So $M = \alpha E$ will be a vectorial relation and the polarizability is thus a second-order tensor. We can define, for a given normal coordinate of vibration Q_s, changes in the polarizability components as:

$$\Delta\alpha_{\rho\sigma,s} = \alpha_{\rho\sigma,s} Q_s = \left(\frac{\partial\alpha_{\rho\sigma}}{\partial Q_s}\right)_0 Q_s \tag{3.135}$$

The normal mode Q_s will appear in the Raman spectrum only if at least one of the six components $\alpha_{\rho\sigma,s}$ of the *variation in polarizability* matrix, build from the polarizability matrix itself, is different from zero. In this case the normal mode Q_s is called Raman active. Whether or not a normal mode is Raman active depends on the simmetry of the equilibrium configuration and of the symmettry of the normal modes Q_s. If the structure and symmetry of the vibrating system is known, it is possible to predict the number of Raman active modes for each symmetry species of the symmetry group under consideration.

Quantum theory of Raman scattering applied for crystalline solids

In terms of particle theory of light, Rayleigh scattering corresponds to an elastic collision process between the photon and the crystal whereas Raman scattering corresponds to an inelastic collision in which the photon either loses one or more quanta of vibrational energy (Stokes lines) or acquires one or more such quanta (anti-Stokes lines). In *first-order scattering* only one phonon is involved while in the *second-order scattering* two phonons are involved. We will describe in detail the first phenomenon. Fig. 3.2 shows the transitions for Rayleigh scattering and for first-order Stokes and anti-Stokes scattering. Let (ω_L, k_L) be the incident photon of the laser with frequency ω_L an wavevector $k_L, (\omega_{sc}, k_{sc})$ the scattered photon, and (ω_j, q) the optical phonon $s = (q, j)$ involved in the scattering process. Energy and momentum are conserved between initial and final states of the system. For Rayleigh scattering we have:

$$\omega_L = \omega_{sc} \tag{3.136}$$

$$k_L = k_{sc} \tag{3.137}$$

while for Raman scattering the conservation of energy and momentum are:

$$\omega_L = \omega_{sc} \pm \omega_j(q) \tag{3.138}$$

$$k_L = k_{sc} \pm q \tag{3.139}$$

In the Stokes process a phonon $\omega_j(q)$ is created (+ sign), while in the anti-Stokes process the phonon (ω_j, q) is annihilated (-sign). The two

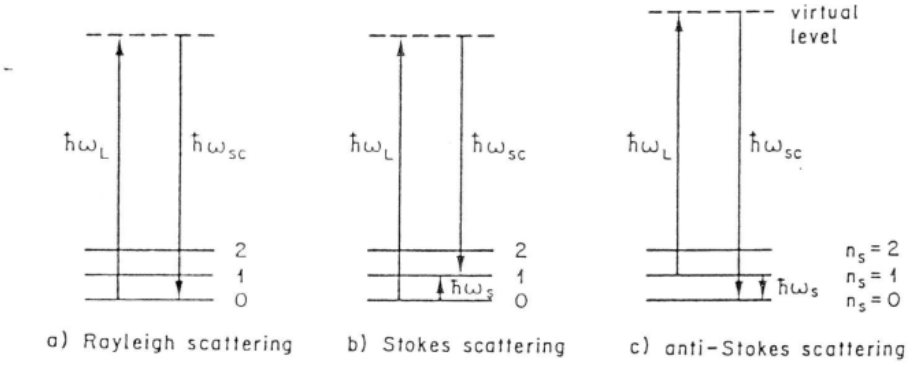

Figure 3.2: Transitions for (a) Rayleigh scattering, (b) first-order Stokes scattering and (c) first-order anti-Stokes scattering [34]

processes are shown schematically in Fig. 3.2. Since $\omega_L >> \omega_s = \omega_j$ it follows that $\omega_L \cong \omega_{sc}$ and, as a consequence, $k_L \cong k_{k_{sc}}$. Due to this,

assuming that the experiments are generally carried out at frequencies where there is no dispersion of the refractive index n, can be demonstrated that in first-order Raman scattering only $q \cong 0$ optical modes can be excited. If a photon with $\hbar\omega_L$ approaches a crystal, it perturbs the electronic wavefunctions because only electrons are light enough to follow the fast-changing electric field of the photon. We can consider this situation as a non stationary state with higher energy assumed by the crystal. This high energy level has nothing to do with the concept of energy levels of the crystal, and infact it is called *virtual level* in order to indicate that it is introduced into the discussion only for the description of the perturbation process. If this virtual level is effectively a real electronic energy level of the crystal, we will talk about *resonant Raman*, and its signal will be much more intense with respect to a normal Raman signal. Due to the fact that the state with $\hbar\omega_L$ is a non-stationary state, the photon leaves it. If it returns to its initial state this gives rise to Rayleigh scattering in which the frequency of the photon remains the same; this is also called *elastic scattering*. With a much lower probability, the photon can lose part of its energy in the interaction process and thus leaves the system with a lower energy $\hbar\omega_{sc}$ (Stokes process). Since the crystal must return to a stationary state the difference $\hbar\omega_L - \hbar\omega_{sc}$ must correspond to a phonon energy; this process is associated with a creation of a phonon of energy $\hbar\omega_s$. In an analogue way, the photon can leave the crystal with higher energy if by chance it finds the system in an excited vibrational state, and the system jumps after the interaction process to the ground state level. This corresponds to the anti-Stokes process which is associated with an annihilation of a phonon. The Stokes and anti-Stokes processes are also referred to as *inelastic scattering*. The picture developped in this subsection demonstrates the experimental behaviour of the ratio between the Raman intensity signals of the Stokes and anti-Stokes processes respectively, because the population of the ground vibrational level is much higher than the population of the excited vibrational levels. Thus the chance for the incident photon to find the system in an excited vibrational level is much smaller than for the ground state. Since the ratio of the two populations, according to Bose-Einstein statistics is proportional to $exp(\hbar\omega_s/k_BT)$, the ratio of the intensities of a Stokes line to a corresponding anti-Stokes line is expected to be proportional to:

$$\frac{I_s}{I_{as}} \propto \left(\frac{\omega_L - \omega_s}{\omega_L + \omega_s}\right)^4 exp\left(\frac{\hbar\omega_s}{k_BT}\right) \tag{3.140}$$

This ratio is considerably larger than unity, that is in contrast with the classical description previously reported.

Chapter 4

Modulation of the electronic gap of graphdiynic fragments by molecular structure and topology

In this study I carry out a computational investigation based on DFT calculations on different types of fragments obtained as finite-dimension subunits of infinite 2D γ-graphdiyne, whose structure is reported in Fig. 4.1. The aim is analysing how the topology, the molecular structure and the geometry of the connection between hexagonal rings formed by sp^2 carbon atoms diacetylenic units in sp hybridization can affect the HOMO-LUMO gap of the system, shedding light on the π-electron conjugation effect occuring in GDY. This work has been inspired by a previous paper published by Tahara et al. [35], where a similar investigation has been carried out for graphyne subfragments. γ-Graphyne (Fig. 4.1) is a planar crystalline structure made by only sp/sp^2 hybridized carbon atoms. Its structure is very similar to that of graphdiyne, in which each hexagon is connected to the others by acetylenic units instead of di-acetylenic ones.

DFT calculations have been carried out for the molecular models sketched in Figs. 13-16 by using the GAUSSIAN 09 package [36] with PBE0 hybrid exchange-correlation functional and 6-31G(d,p) basis set and the numerical values of gaps so computed are reported in Table 4.1. We noticed that all the structures that we have analyzed are fixed in a planar geometry, so no effects of distortion from planarity on delocalization were considered. Even if finite GDY fragments could be not exactly planar, anyway our aim is to investigate the intramolecular effects which rules the electronic properties of 2D-GDY, which is indeed

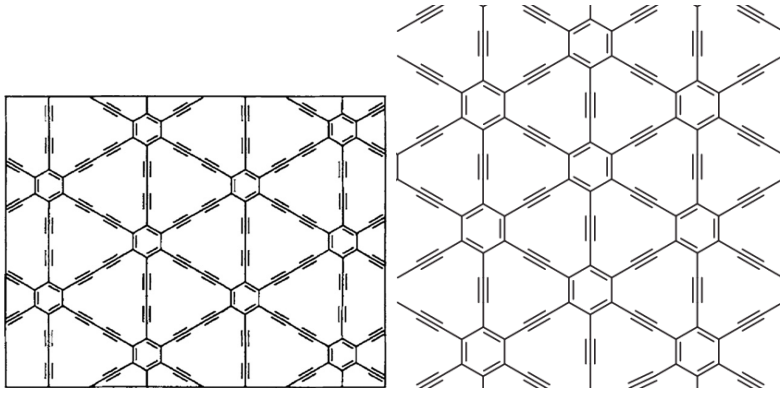

(a) γ-Graphdiyne (b) γ-Graphyne

Figure 4.1: γ-Graphyne's and γ-Graphdiyne's structures

described as infinite planar slab. Morever, with my results, it is possible to have a clearer vision on the electronic properties of these type of fragments that could be helpful to scientists who synthetized them [5]. It can be used as a reference to obtain molecules with peculiar electronic properties and with a certain degree of π-conjugation, depending on the topology of the synthetized molecules. A usual, distortion from planarity are expected to reduce π-electron delocalization and increases the band gap, as shown in [35] for finite dimension GY fragments. We have to remember that a great part of the fragments that we analyzed in our work have been already synthetized. For example the fragments that we called F13, F16, F15 and also others have been already obtained experimentally by Haley [37]. In order to compare our results with extended systems, we also carried out DFT calculations adopting Periodic Boundary Conditions (PBC) by using the CRYSTAL17 code [38] for both infinite 1D polymers where monomeric units are connected in different conjugation pathways(para, ortho, meta) and infinite 2D γ-GDY. Also in this case PBE0/6-31G(d,p) level of theory has been employed.

4.1 Effect of the meta, ortho and para conjugation in graphdiynic polymeric chains with the increase of monomeric units

Tahara et al. have done computational studies on aromaticity, bond length alternation (BLA) and band gap in dehydrobenzoannulene (DBA) based molecules, whose structure is reported in Fig. 4.2, to understand the electronic effects of diacetylenic units on phenyl rings' delocaliza-

FRAGMENT	GAP(eV)	FRAGMENT	GAP(eV)
F1	3.6858	F2	3.3745
F3	3.3119	F4	3.1935
F5	3.5685	F6	3.5976
F7	3.1133	F8	3.1141
F9	3.1211	F10	3.1620
F11	2.8964	F12	4.1560
F13	3.8436	F14	2.9837
F15	2.9307	F16	3.0088
F17	3.3138	F18	3.2572
F19	3.4229	F20	3.3029
F21	3.4118	F22	3.0052
F23	3.0583	U	4.3489
P2	3.6281	P3	3.3364
T2	4.151	T3	4.07
T4	4.03	C3	4.07
C4	4.03	O2	3.814
O3	3.604	O4	3.505

Table 4.1: Fragments' band gaps

tion.

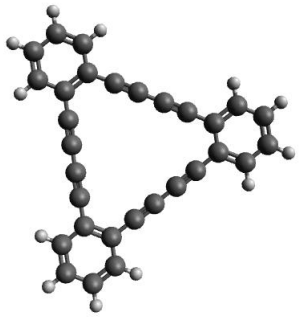

Figure 4.2: Dehydrobenzoannulene

In their analysis they focused also on the effect of the conjugation-pathway type on the electronic gap. Indeed, the connection between phenyl rings and diacetylenic units can be done in three different ways (Fig. 4.3) :

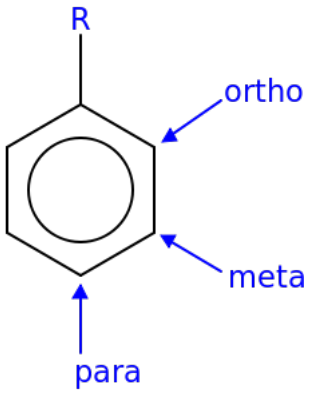

Figure 4.3: Orto, meta and para positions

- In ortho-substitution, two substituents occupy positions next to each other. In Fig. 4.3, these positions are marked R and ortho.
- In meta-substitution the substituents occupy positions marked by R and meta in the figure
- In para-substitution, the substituents occupy the opposite ends corresponding to R and para.

The authors found that the length and the number of para-conjugation pathways between aromatic rings and diacetylenic units in fused DBA rings play an important role in determining the electronic properties. In particular the band gap is found to decrease when increasing the number and length of these types of pathways in the different fragments. Inspired by the work by Tahara, I extended and widened this analysis to describe GDY and related fragments, starting by its smallest building units. Tahara indeed considered as the fundamental unit of GY the simple triangular model of three phenyl groups linked by acetylenic units while in my case I considered also much simpler building blocks. As a first step I carried out indeed DFT calculations on oligomeric chains made by increasing number of diacetylenic units and different conjugation pathways, compared to the associated infinite polymers computed in PBC. The results are reported in Fig. 4.4.

As a first effect I found that π-conjugation for chains in which the substitution of the diacetylenic units is in meta with respect to phenil groups is very low. By connecting the chemical groups in meta-, two different types of chains can be generated by changing the configuration: trans (T series) and cis (C series). For both configurations, the

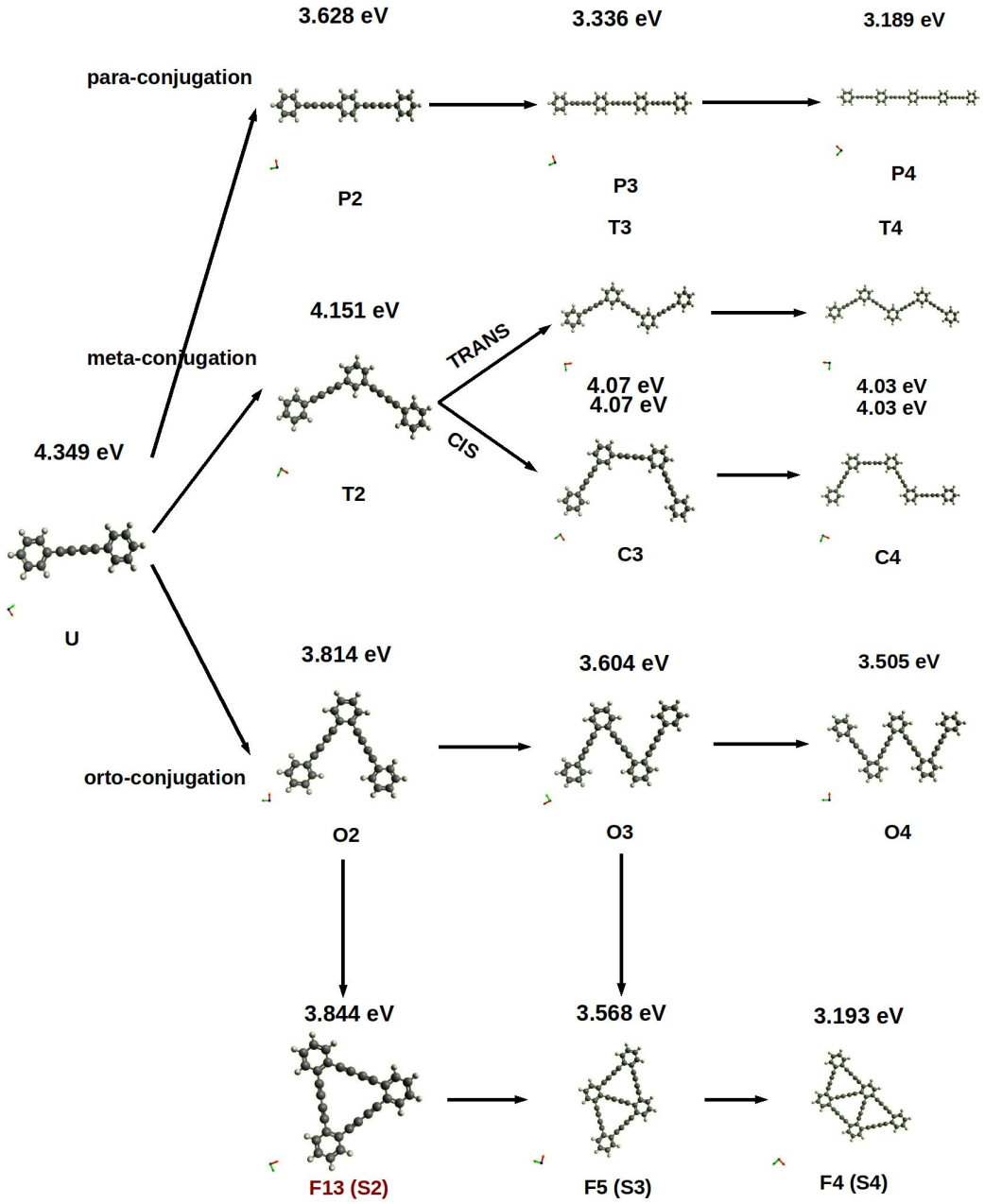

Figure 4.4: Different types of conjugation with increasing number of diacetylenic units

gap decreases very slowly with the increase of the diacetylenic units and reaches, very quickly, an asymptotic value that corresponds to the infinite polymer in cis and trans configuration. Due to low increase of π-electron delocalization induced by meta conjugation, not significant differences are found for different type of isomerism of the chain (cis and trans) as shown in Fig. 4.4. Infact both C3 and T3 (4.07 eV) and both C4 and T4 (4.03) have the same value of the gap. All of these results agree on what has been widely reported in the literature about meta-conjugation pathway. For the subsitution in para, as already found by Tahara et al. [35], we obtain a very fast decrease in the gap with the increase of diacetylenic units until reaching a plateu. This can be seen in the P series (U,P2,P3). The band gap value found for the infinite para-polymer is 2.836 eV which is significantly larger than the value found in 2D-GDY that according to our calculation is 1.639 eV, as reported in chapter 5. Therefore, the modulation of the gap in GDY systems cannot be described only based on chain-models fragments. Concerning ortho-conjugation, I also have found that this configuration (O series) gives a non negligible contribution in the decrease of the gap with the increase of the number of units, saturating faster than para-units but slowlier with respect to meta ones. As a last case, I considered also the S series formed by oligomers where triangular rings are fused together. It should be noted that the associated infinite polymer would coorespond to the case of the thinnest armchair nanoribbon that can be defined for γ-GDY, as described in detail in chapter 6. The oligomers so obtained can be described a models where both ortho and para-conjugation pathways are co-existing. In Fig. 4.5 we can observe the peculiar trend of their band gap for increasing number of units: for 2 and 3 diacetylenic units in the chain ortho-conjugation seems to rule the band gap behaviour while increasing more and more the length of the oligomers the gap progressively decreases becoming lower than para-conjugated molecules and displaying a much slower decay. Indeed the asymptotic value is reached approximatively for 20 diacetylenic units giving the lowest value of the band gap when the plateau is reached. This value is reported as the band gap value computed for the related one dimensional infinite chain, as a reference. The corresponding infinite polymer shows a gap of 2.28 eV which is anyway higher than 2D-GDY. This is in disagreement to what has been reported by Tahara, who suggests that by maximizing the number of units in para-conjugation (at least in one dimension) the graphyne-like character would be recovered. On the other hand the results obtained for the infinite S models is in perfect agreement with what has been reported about GDY nanoribbons [20]:GDYNR have indeed band gaps

that are higher than 2D-GDY and which decreases with the transversal width of the ribbons, so the more we approach te 2D systems. This is why the infinite S polymer, the thinnest GDYNR, correctly displays a gap much larger than 2D-GDY. Further comparison and discussion about GDYNR will be reported in one of the following chapter.

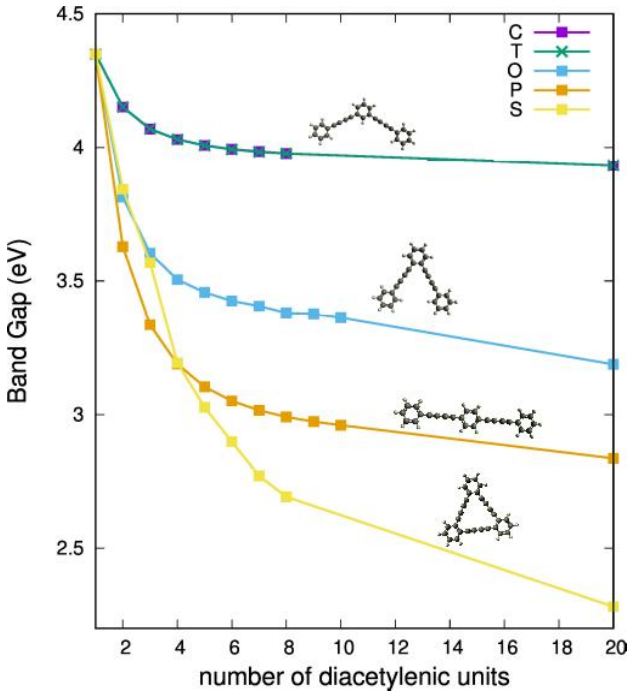

Figure 4.5: Band gap variation for different chains with respect to the number of diacetylenic units

4.2 Influence of the number and length of para-pathways in graphdiynic fragments

Analyzing various GDY subfragments we can state that the para-substitution is the most efficient in terms of π-delocalization and gives the highest decrease in the gap depending on the number of units connected in para with respect to the phenil ring. This statement is in agreement with the relevant results obtained by Tahara, for which it is the length and the number of para-conjugated units that have the most significant effects on the electronic properties as already noticed in the previous subsection for P models. This effect can be seen for example in fragments F2 and F8: in F8 (3.1141 eV) we have 3 para-conjugated pathways made by 2 diacetylenic units while for F2 (3.3745

eV) we have only one. Also comparing F2 (Fig. 4.6) and F9 (Fig. 4.7) I observed a decrease in the gap because in the first (3.3745 eV) we have one para pathway made by two units and an ortho pathway while in the second (3.1211 eV) we have two para-pathways. Moving then from F9 to F8 (Fig. 4.7) it can be seen that the addition of another para-pathway made by 2 units reduces further the gap but not significantly. Another interesting behaviour can be seen in Fig. 4.8. Indeed, here we have that the band gap of F14 (2.9837 eV) is lower than that of F23 (3.0583 eV). This is due to the fact that in F14 we have one long pathway in para with 3 units and 2 pathways in para with 2 units while for F23 we have again one three-units para pathway and a long ortho pathway (that conjugates less). Analyzing then F15 (2.9307 eV) with respect to F14 (2.9837 eV) we see that the band gap decreases but not so effectively. On the basis of these examples, we can say that indeed the number and length of para-conjugated pathways affect for sure the band gap but their effect rapidly becomes ineffective the more we increase them.

4.3 Effect of the ortho- and meta-conjugation in graphdiyne fragments and of the ring's closure

In addition to the previous observations, which parallels what found by Tahara for GY fragments, further effects can be identified based on the different structure and topology in the GDY models here considered. Indeed, even if para-conjugation gives initially a large effect on the gap, other phenomena can be of the same order of magnitude. If we consider model such as F2 (3.3745 eV), F17 (3.3138 eV) and F19 (3.4229 eV) fragments, where additional units are added in ortho-position with respect to P2 (3.6281 eV) molecule, it can be seen that there is a decrease in he band gap of about 0.3 eV (Fig. 4.6). The gap is comparable with P3 (3.3364 eV) that is the next oligomer in the P series where we are increasing the length of the para-conjugated pathway. This behaviour suggests that the combined presence of both ortho- and para-conjugation on the phenyl group gives another important contribution in band gap decrease.

Another peculiar effect that I have identified is related to the closure of triangular rings. Indeed as we can see in Fig. 4.6, for F19 (3.4229 eV), F2 (3.3745 eV) and F8 (3.1141 eV) molecules the closure of the rings progressively lowers the gap, in particular if we consider F4 (3.193 eV) and F11 (2.896 eV) in comparison with F2 and F8, F4 in particular can be described as a model where the longest para-conjugated pathway is formed by only two diacetylenic units but anyway it has a band

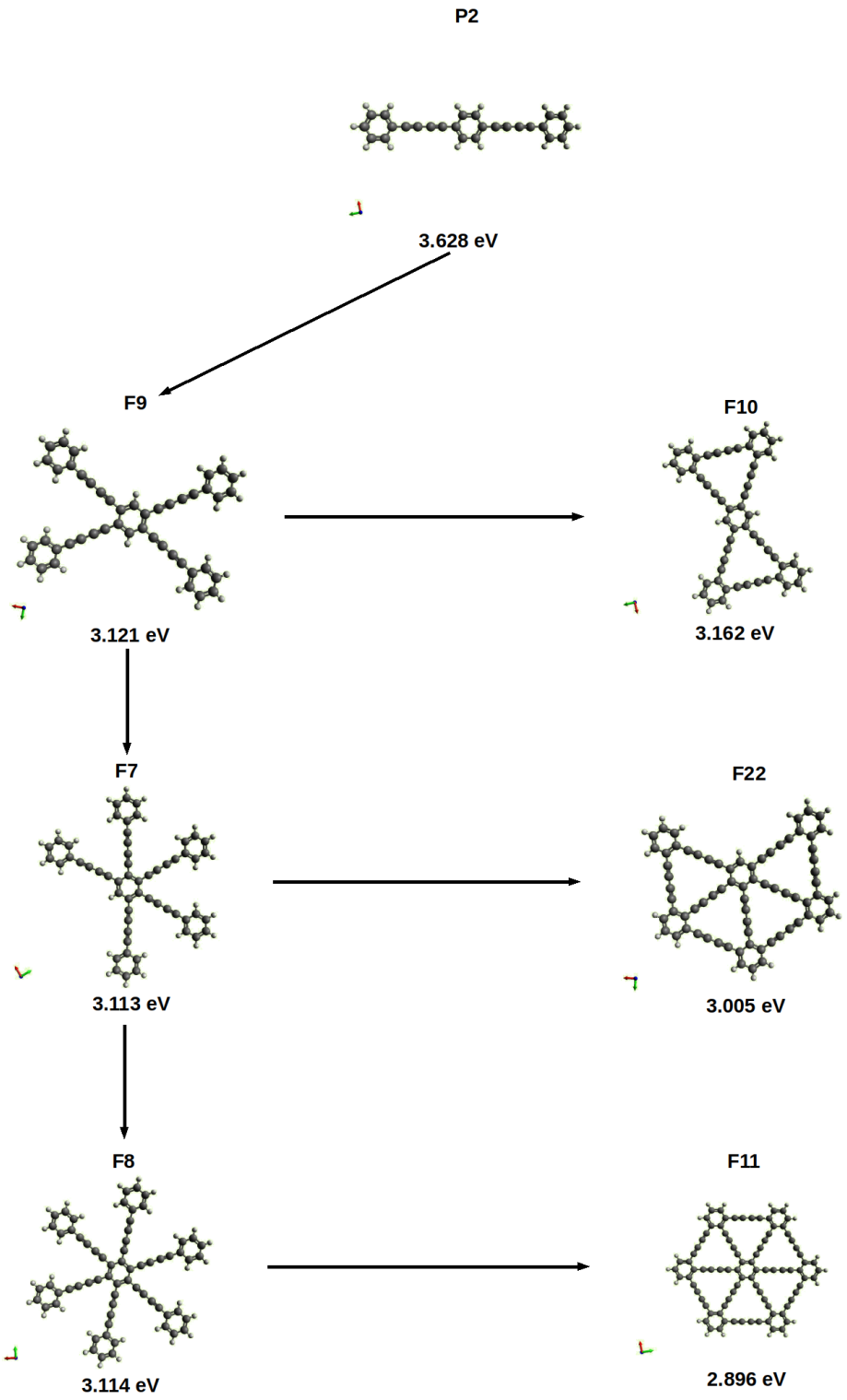

Figure 4.6: Effect of orto-conjugation in addition with the para one and of ring's closure

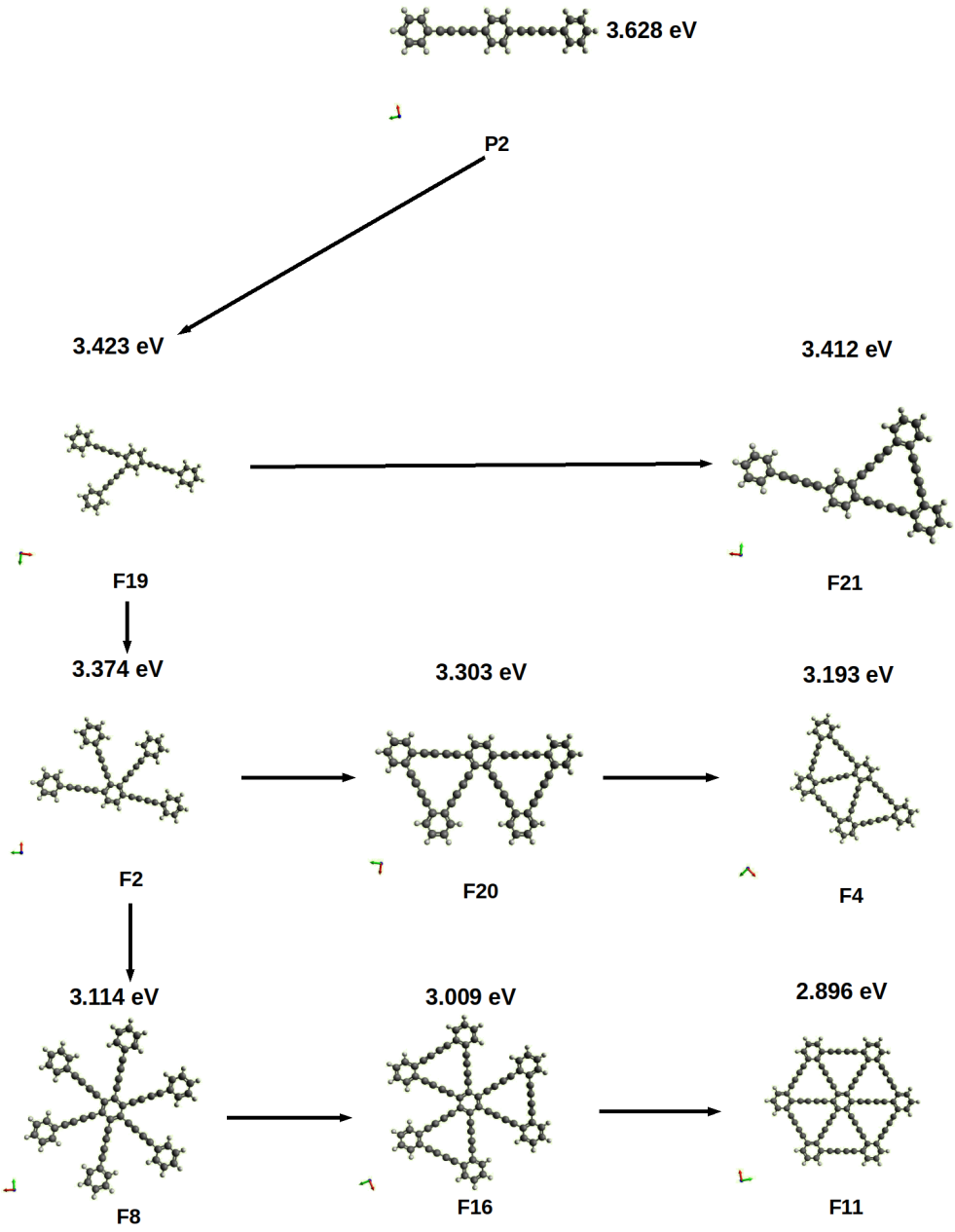

Figure 4.7: Effect of the increase in the number of para-conjugations and also of the rings' closure

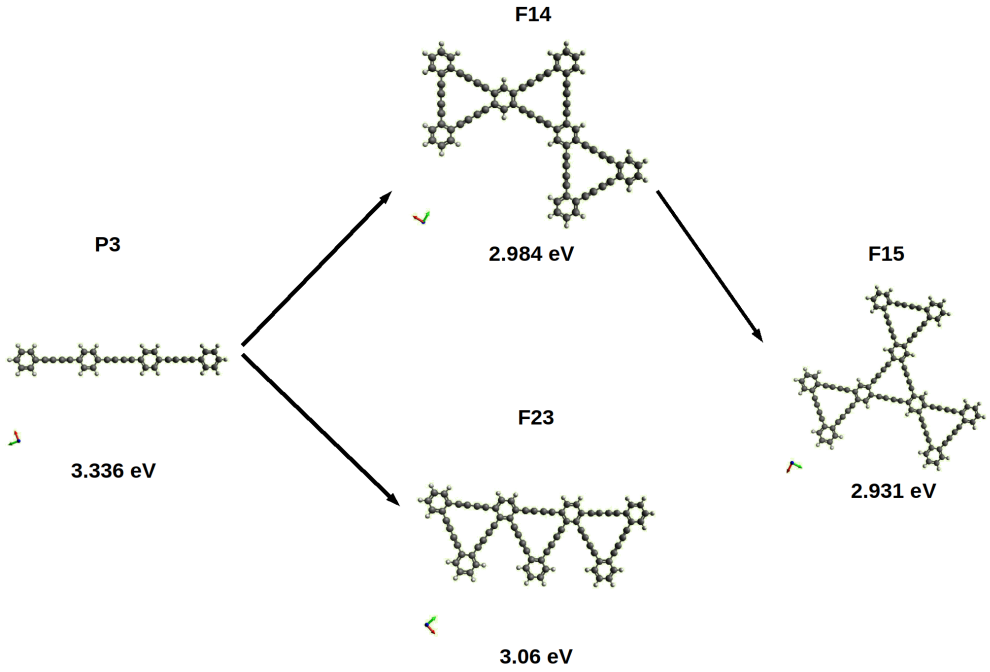

Figure 4.8: Different types of fragments with the same maximum length of the para-conjugation

gap which is comparable with the para-conjugated oligomers P4 (3.189 eV) where the para-conjugated pattern include four diacetylenic units. Furthermore, we can also consider F4 as one half of F11 model where thanks to the formation of a larger number of para-conjugated units the gap is further reduced. All the structures that I have analyzed are planar, so no effects of distortion on delocalization were considered. As a final case, I further highlight the lack of effect which is induced by meta-conjugation. Indeed, if we compare the fundamental units U (4.349 eV) with T2 (4.151 eV) with model F12 (4.1560 eV) we verify indeed that conjugation in meta does not affect the band gap. This is particularly important since infinite 2D materials based on F12 units have been indeed produced [referenza], and it would be thus very interesting to compare their properties with respect to γ-GDY based on the structural topological effects here investigated.

4.4 Conclusions

Based on the data and the discussion reported above I summarize here the main results obtained:

- It is not sufficient to consider only monodimensional infinite chains to understand the electronic behaviour and π-electron delocalization in GDY. It is necessary to move towards a two dimensional description, rapresented by the model of the nanoribbon.
- I have demonstrated that the results obtained by Tahara about para-conjugation pathways are compatible also for GDY subfragments: increasing para-conjugation pathways in number and length, a significant decrease in the gap is obtained
- In addition, I have seen that there is a coupled effect between para- and ortho-conjugation, both in small fragments and long chains, having a further effect in lowering the gap
- The formation of triangular rings further lowers the band gap.
- The meta-conjugation gives a negligible π-electron delocalization, preventing any long range π-conjugation.

These results can be useful to understand better the electronic properties of these type of molecules and optimize their possible use in nanoelectronics. Infact, tuning for instance the synthesis it is possible to obtain different types of fragments or chains with different conjugation in order to get the desired properties in terms of conductivity

and electron mobility. Moreover, thanks to this investigation, it is possible to compare electronic properties of different infinite conjugated chains with nanoribbons made by cutting the infinite GDY with different edges. As we will see in one of the following section the edge resembles the infinite chain in terms of electronic and also vibrational properties, giving us a good instrument for comparison.

Chapter 5

Computational investigation of GDY crystal

After the evaluation concerning GDY subfragments, I focused on the computational analysis of infinite periodic structures. Infact my aim was to shift the attention towards GDY-NRs in order to study their electronic and vibrational properties. The study was driven by the fact that the intriguing electronic properties of graphdiyne and, in particular, of graphdiyne's nanoribbons make them appealing for nanoelectronic devices. Moreover the vibrational characterization, through IR and Raman spectroscopies, rapresents an important tool to understand in a better way their morphology and topology.

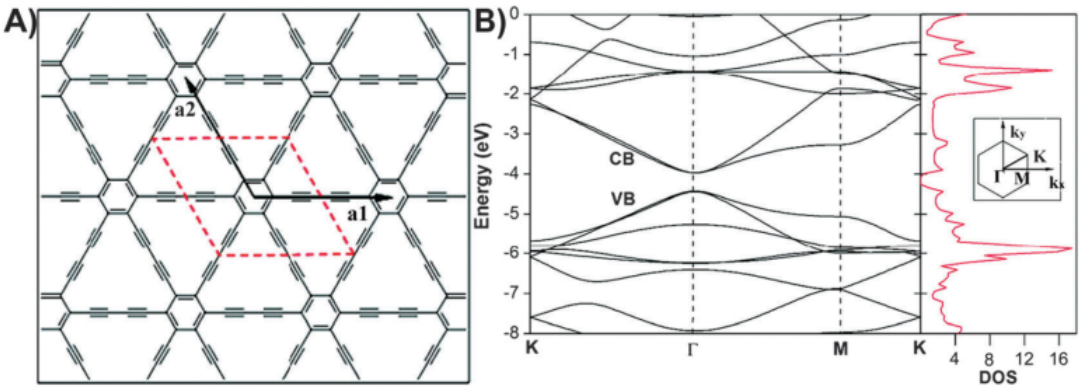

Figure 5.1: Schematic representation of a single GDY sheet. Band structure and density of states for a single GDY sheet, obtained from DFT calculations. The Brillouin zone is also shown.

The calculations of the 2D γ-graphdiyne were done using the CRYSTAL14 and CRYSTAL17 codes by using DFT and applying periodic boundary conditions. For these evaluations we use the PBE0 hybrid functional and the 6-31G(d,p) (6-31G(d) in the case of the infinite GDY) as basis set. The TOLINTEG parameter was set to 9 9 9 9 80, which means that integrals are either approximated or disregarded when the overlap between the corresponding basis functions is below 10^{-9}. The treshold on the self consistent field (SCF) energy was set to 10^{-8} (TOLDEE parameter set to 8) for the geometry omptimization and to 10^{-10} for the calculation of numerical derivatives in the Coupled Perturbed Hartree Fock process implemented in Crystal. The reciprocal space was sampled along the two lattice vectors according to a sublattice with a SHRINK factor set to 50 50; it corresponds to 234 independent k vectors scanned in the irreducible part of the Brillouin zone. For the basis set, because exponents of carbon gaussian basis functions lower than about 0.17 Bohr cause severe convergence problems in the SCF-procedure due to near (or even) linear dependencies in the basis set, a gaussian's exponent was increased from 0.1687 to 0.187 as suggested by Lorenz at al. for the case of graphene [39]. The first analysis was focused on the study of the electronic and vibrational properties of the infinite slab of γ-graphdiyne. From the literature we know that GDY is a semiconductor, whose symmetry group is $P6/mmm$ (D_{6h}), with a direct band gap located in the reciprocal space at the Γ point (wavevector $k = 0$). In Fig. 5.1 the band structure of the graphdiyne is reported from the literature [16]. Usually the GDY band gap depends on the applied methods and the exchange-correlation functionals used, and it ranges from 0.46 to 1.22 eV as reported in literature (see Table 1 in the second chapter).

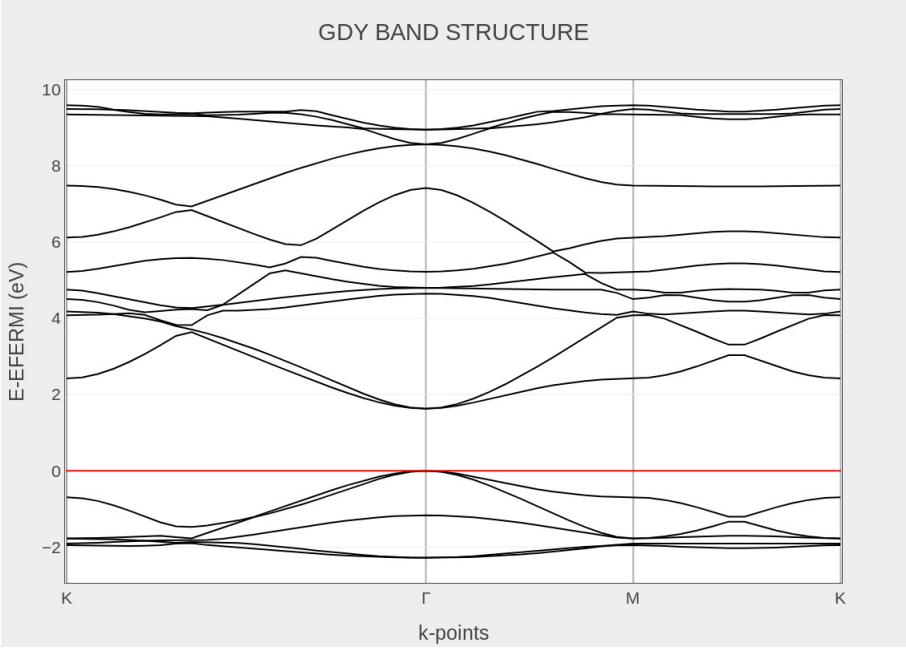

Figure 5.2: Graphdiyne band structure; the red line rapresents the Fermi energy.

GDY crystal has a primitive cell that contains 18 carbon atoms, that means 108 electrons per cell. Therefore the number of electronic bands will be 108 and the band gap will fall between the 54th and the 55th band. In Fig. 5.2 the computed band structure for the γ-GDY is reported. As we can see from my computation, the band gap is at Γ as it is known from the literature, and it has a value of 1.629 eV, much larger than the values found with LDA or with other functionals. This is caused by the use of the PBE0 hybrid functional instead of GGA functionals or other functionals based on LDA that are less accurate in predicting the band gap. Compared to graphene, it can be seen that the presence of *sp*-hybridized carbon atoms induces the opening of a gap in the structure when we pass from a completely sp^2 hexagonal structure (graphene) to a mixed $sp - sp^2$ structure. Band structure of graphdiyne is composed by deeply located σ-type bands, whereas the low-energy π (π^*) bands form the edges of the gap.

In my analysis I focused mainly on the interpretation of vibrational spectra since in literature there are only few theoretical studies on the prediction of vibrational properties of graphdiyne. As we said, the GDY primitive cell contains 18 atoms that means 54 normal modes of vibration. Through the use of Coupled-Perturbed Hartree Fock method,

implemented in Crystal, it was possible to compute Raman and IR spectra of the infinite GDY slab, reported in Fig. 5.3.

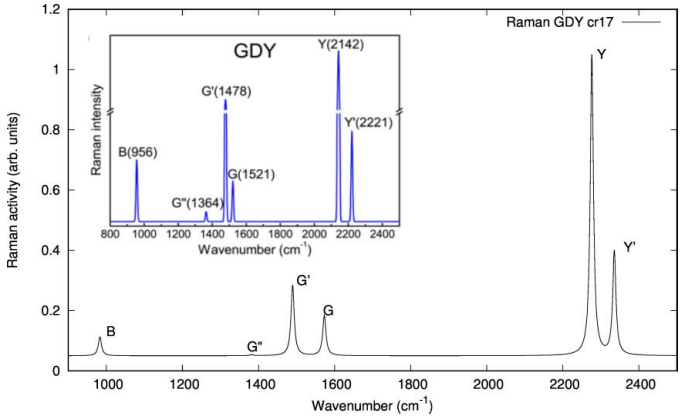

(a) Raman spectra

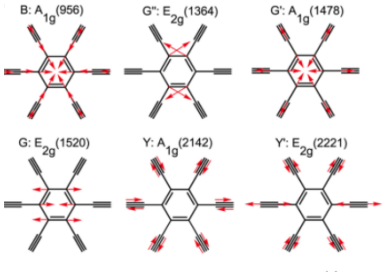

(b) Normal modes, taken from the literature [18], related to the raman spectra

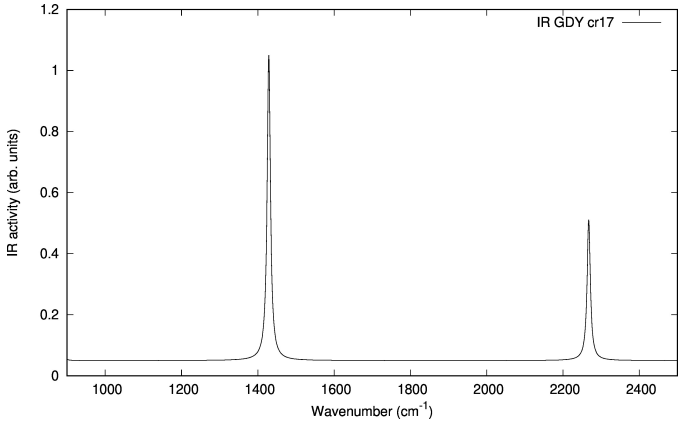

(c) IR spectra

Figure 5.3: Raman (containing also the one taken from the literature for comparison, calculated using DFT with LDA as exchange-correlation function [18]), IR spectra and normal modes of infinite γ-GDY

The most intense and important Raman peaks are reported in Table 5.1 with wavenumber, Raman activity and symmetry species of the associated normal modes. The names of the Raman lines reported in the table have been used based on the nomenclature introduced by Zhang et al. [18].

Table 5.1: Most intense Raman active normal modes

Line	Wavenumber (cm^{-1})	Raman activity (A^4/amu)	Symmetry species (irrep)
B	983	231213	A_{1g}
G"	1382	6278	E_{2g}
	1382	6278	E_{2g}
G'	1490	869870	A_{1g}
G	1573	248923	E_{2g}
	1573	248923	E_{2g}
Y	2276	3707443	A_{1g}
Y'	2335	638183	E_{2g}
	2335	638183	E_{2g}

As we can see, we obtain a good agreement between our calculated Raman spectra and the one deriving from the literature, which has been computed with DFT using LDA as exchange-correlation function [18]. We observe a shift in the two high wavenumber peaks, the ones related to alkyne chains normal modes, probably due to the different exchange-correlation functional used for the two different computed spectra. Thanks to the results of vibrational computations it was possible also to analyze normal modes related to the Raman peaks, in order to compare them with the ones coming from the literature. Some calculated normal modes are degenerate, therefore in the tables they are marked with two peaks but in the Raman and IR spectra they are fitted with a single Lorentian function with an intensity that is the sum of the two intensities associated to the degenerate modes. At first we can observe the so called B mode (Fig. 5.4), located at 983 cm^{-1} in our Raman spectra, that corresponds to the breathing mode of the hexagonal rings present in the structure. This mode can be found also in graphene, it is called D peak, it is located at 1350 cm^{-1} and it is active only for disordered graphene. Due to the effect of the diacetylenic units linked to the hexagons that tend to withdraw electronic charge due to the *sp* hybridization, the bonds in the graphdiyne's hexagons are less strong with respect to graphene ones. This is the reason that causes a decrease in the force constant of the bond implying a decrease in the wavenumber associated to that normal mode of vibration. However the

presence of this normal mode in both the structures makes it a sort of fingerprint of the carbon-based hexagonal structure.

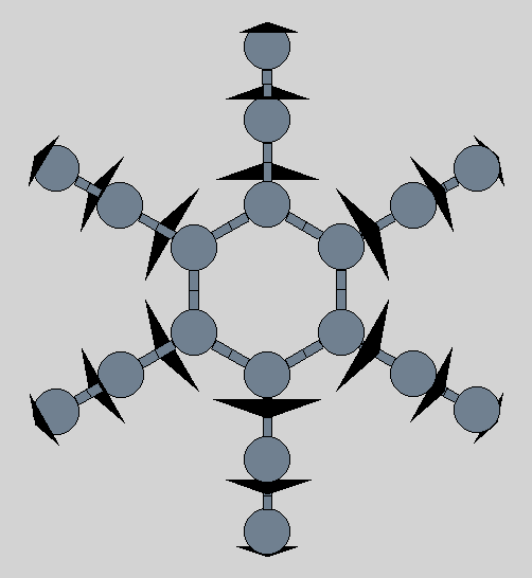

Figure 5.4: Breathing mode of the hexagonal rings (B mode)

The G peak in the graphdiyne Raman spectra is located at almost the same wavenumber with respect to graphene; infact for the latter is located at 1582 cm^{-1} (Fig. 5.5) while for GDY it is located at 1573 cm^{-1}.

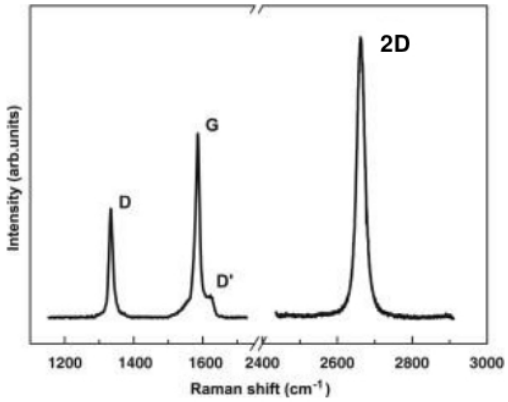

Figure 5.5: Raman spectra of graphene

As we know this peak is related to the stretching of the bonds in the hexagonal rings, and it involves vibration of the sp^2-hybridized carbon atoms. Here we observe only a very slight shift in the wavenumber due to acetylenic linkages but it is also possible to observe a decrease in intensity of this peak as a further consequence of the presence of diacetylenic units. In Fig. 5.6 the normal mode assocaited to the G line of the GDY crystal is rapresented.

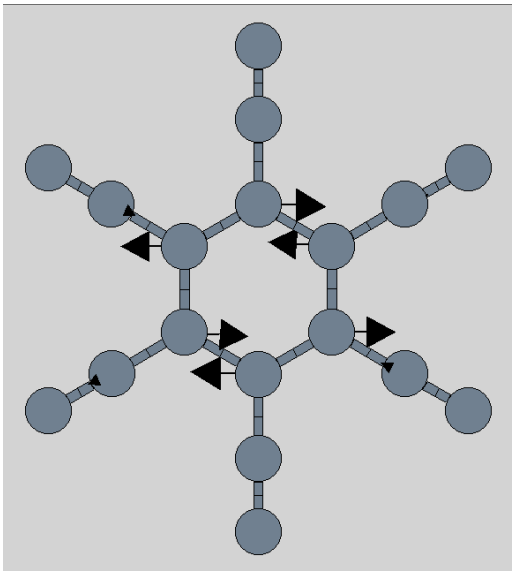

Figure 5.6: Stretching mode of the bonds in the exagons (G mode)

Differently from graphene, graphdiyne has other 2 peaks that can be found in the same wavenumber region of the G peak; they have been called G' and G". They are located respectively at 1490 cm^{-1} and 1382 cm^{-1} and they are again due to normal modes including the rings but coupled to motions also of the diacetylenic units that are present in the structure. The G' line is connected to the vibrations of carbon-carbon single bonds between triply coordinated atoms and theirs doubly coordinated neighbours. It is a sort of breathing mode coupled with a CC stretching mode involving triple bonds. The G" line comes from the scissoring vibration of atoms in benzene rings. The normal modes of vibration for these peaks are depicted in Fig. 5.7 .

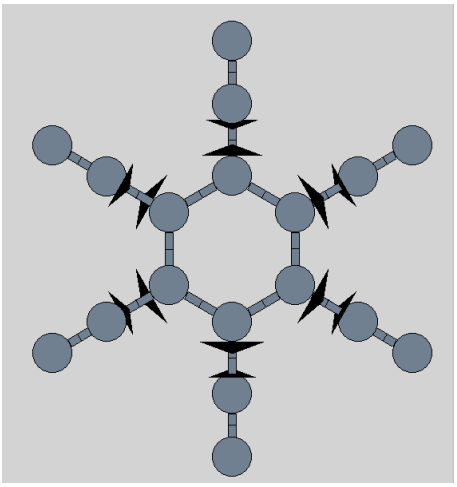

(a) G'

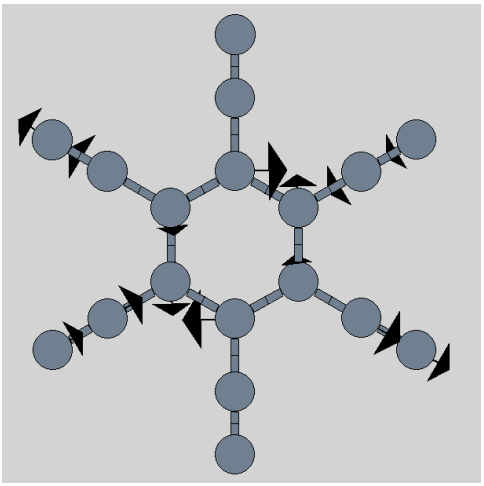

(b) G"

Figure 5.7: Vibrational normal modes for G' and G" lines

At higher wavenumbers we find the region of the Raman spectra where we have markers of the *sp*-chain, in the wavenumber range of 1800-2500 cm^{-1}. Indeed we observe two peaks that are called Y (at 2276 cm^{-1}) and Y' (at 2335 cm^{-1}). In graphene, due to the absence of *sp* hybridized carbon atoms, this region is occupied only by second order raman peaks. The two normal modes associated with the two lines can be seen as 2 of the 6 linear combinations of the 6 ECC modes [40], each one localized on the single diacetylenic unit. The normal mode associated to the Y peak is rapresented by the synchronous stretching and contracting of triple bonds and it is a fully symmetric mode. It is the total symmetric combination between the 6 ECC modes in which

they are all in phase between each other. The normal mode associated to the Y' line can be described as another linear combination of the 6 ECC modes associated to the single diacetylenic unit, in which the ECC modes are out-of-phase between each others. One third of the chains are vibrating with an ECC mode with a certain phase while the other two thirds are vibrating with an ECC mode, localized on each single chain, that has a different phase with respect to the previous one. Both normal modes are reported in Fig. 5.8.

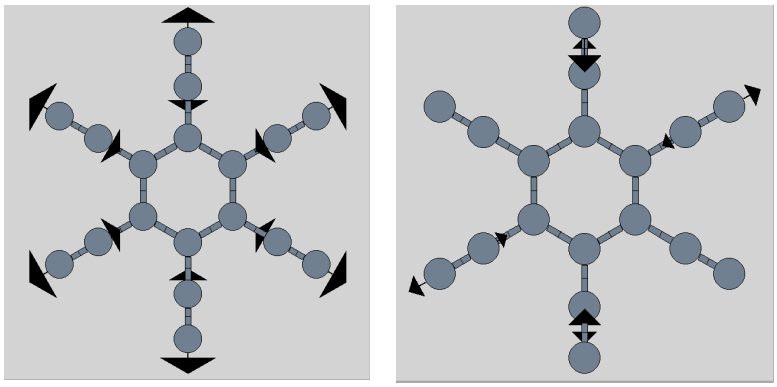

(a) Y (b) Y'

Figure 5.8: Vibrational normal modes for Y and Y' lines

About the IR spectra, the most intense normal modes are reported in Table 5.2. We can distinguish two major peaks, one located at 1429 cm^{-1} and the second located at 2267 cm^{-1}. The first peak is associated

Table 5.2: Most intense IR active normal modes

Wavenumber (cm^{-1})	IR activity (km/mol)	Symmetry species (irrep)
1429	522	E_{1u}
	522	E_{1u}
2267	240	E_{1u}
	240	E_{1u}

to a vibrational normal mode that involves vibrations of sp^2 hybridized carbon atoms in the hexagonal rings while the second is associated to a normal mode characterized again by CC stretching of sp hybridized carbon atoms, as reported in Fig 5.9.

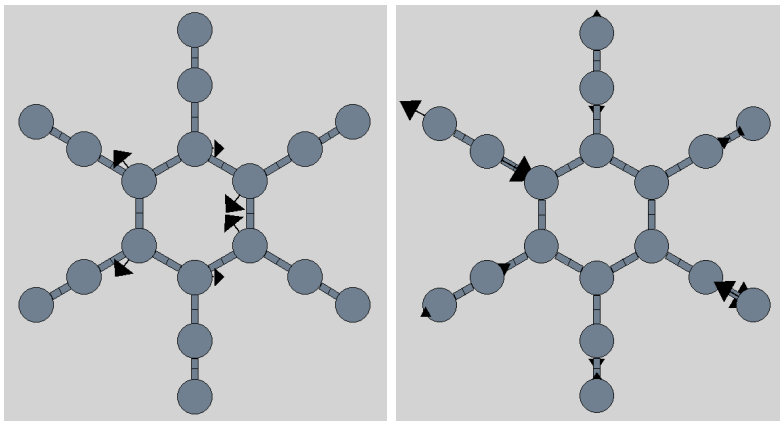

(a) 1429 cm^{-1} (b) 2267 cm^{-1}

Figure 5.9: IR acrive normal modes of the two active lines in the IR spectra. On the left the one at 1429 cm^{-1}, on the right the one at 2267 cm^{-1}.

Chapter 6

Theoretical study of the electronic and vibrational properties of GDY nanoribbons (GDYNRs)

6.1 Introduction

Moving from GDY fragments to the infinite systems, I focused my attention on DFT calculations, by using again the CRYSTAL14 and CRYSTAL17 packages, of graphdiyne nanoribbons. Consistently with the calculations on fragments and 2D-GDY, I used the PBE0 hybrid functional and the 6-31G(d,p) as basis set, the SHRINK factor was set to 50 and the TOLDEE and TOLINTEG parameters were set at the same values used for the infinite GDY slab. The SHRINK factor so adopted corresponds to 26 k points scanned in the first Brillouin zone. The aim of this work was to study in detail the electronic properties, in terms of the band gap, and the vibrational properties, analyzing Raman spectra and normal modes of vibration, of GDYNRs focusing on π-conjugation effects. For these structures, the same terminology reported in the literature was used. Infact we divided nanoribbons in 2 families: zigzag (Fig. 6.2) and armchair (Fig. 6.1) nanoribbons. This is due to the fact that both band gap and Raman spectra are strongly dependent on the nanoribbon's edge type and different normal modes are active depending on the edge considered. As reported in literature, the nomenclature used for our nanoribbons is defined by the index n that indicates the number of repeated units ($C_6 - C \equiv C - C \equiv C - C_6 - C \equiv C - C \equiv C - C_6$) along the ribbon. For armchair nanoribbons these units correspond to the monodimensional chains of

type P, formed by phenil groups and diacetylenic units, contained in the thickness of the nanoribbon. For zigzag ones the corresponding units are the monodimensional T-type chains contained in the nanoribbon. For this scheme, armchair nanoribbons (ANRs) are defined by only integers value of n, whereas for zigzag nanoribbons (ZNRs) the number of repeated units n can be also an half integer (Fig. 6.1 and 6.2). At the edges, carbon atoms are saturated bonding them with hydrogen atoms to avoid dangling bonds.

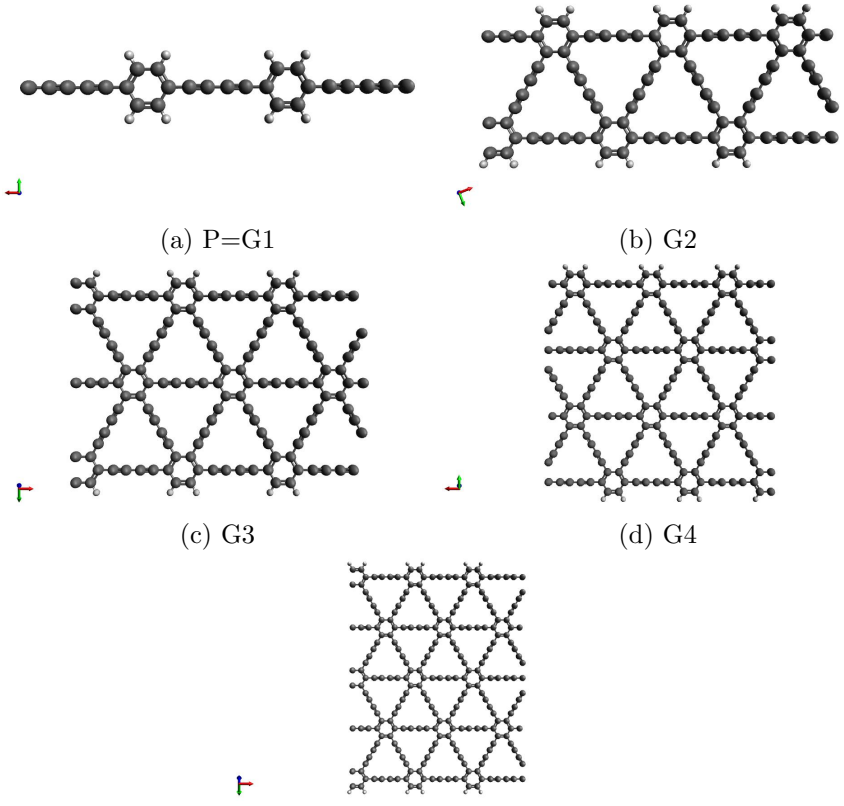

(a) P=G1 (b) G2

(c) G3 (d) G4

(e) G5

Figure 6.1: Structure of armchair nanoribbons

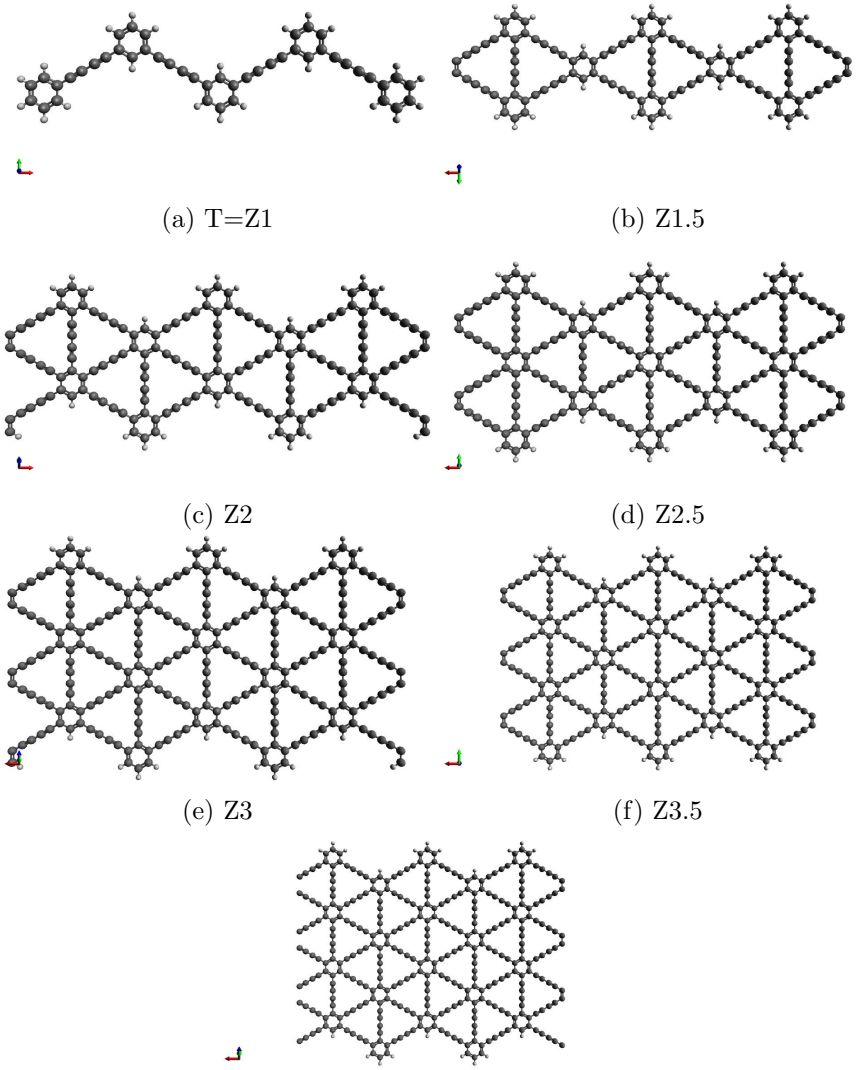

(a) T=Z1 (b) Z1.5

(c) Z2 (d) Z2.5

(e) Z3 (f) Z3.5

(g) Z4

Figure 6.2: Structure of zigzag nanoribbons

6.2 Band structure and band gap evolution of GDYNRs with increasing width

The first analysis is based on the computation of the band structure of armchair and zigzag nanoribbons with different width. For simplicity, the armchair series was termed with the name G while the zigzag series was termed with the name Z, as reported in literature [20]. All the

analyzed nanoribbons are reported in the Table 6.1 with name, lattice constant and band gap. What we found by the analysis of the band

Table 6.1: Armchair(G) and Zigzag(Z) nanoribbons with reported lattice constant, band gap and number of electrons per cell

Name	lattice constant(Å)	BG (eV)
G2	9.439	2.2813
G3	9.439	2.0146
G4	9.439	1.8813
G5	9.439	1.8044
Z1.5	16.35	2.8658
Z2	16.35	2.4100
Z2.5	16.35	2.1727
Z3	16.35	2.0301
Z3.5	16.35	1.9370
Z4	16.35	1.8727

structure is that they are all, both zigzag and armchair ones, semiconductors with a direct band gap located at Γ, similar to the infinite 2D-GDY (Fig. 6.3). Moreover, as also previously reported in literature [20], the band gap decreases with the increase of the nanoribbons' width approaching to the value, both for zigzag and armchair ones, of the infinite GDY, that corresponds to an infinite width (1.6289 eV), as depicted in Fig. 6.4. This is a known effect of π-electron confinement. The position of the gap in the Brillouin zone is not affected by the edge-type of the nanoribbons, but, observing band gap values, we can notice that for the same number n (number of repeating units along the ribbon) associated to the nanoribbons, armchair nanoribbons have a lower band gap with respect to the zigzag ones at least for low values of n. Increasing the width of the nanoribbons both zigzag and armchair nanoribbbons band gaps approach to very similar values and tend, in the same way, to the band gap of the infinite GDY.

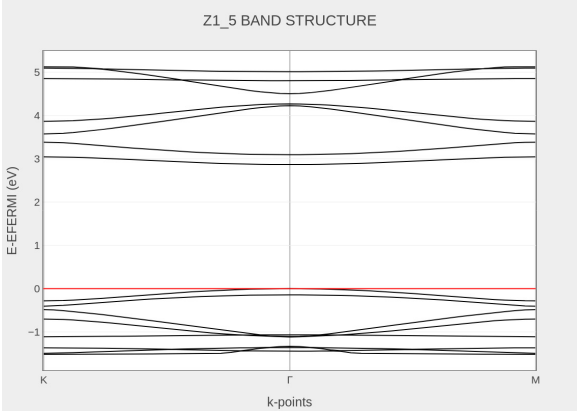

(a) Z1.5

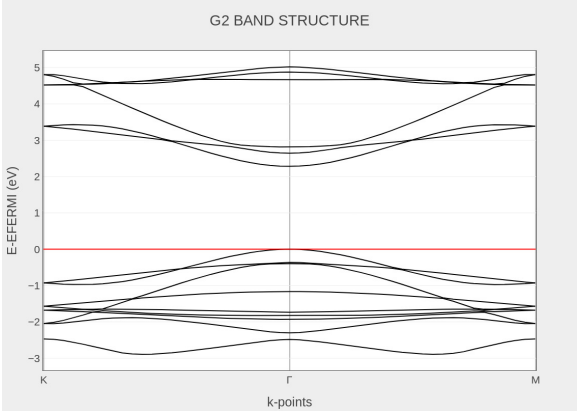

(b) G2

Figure 6.3: Computed band structure of zigzag (Z1.5) and armchair (G2) nanoribbons. The Fermi line is reported in red.

This result shows that the band gap is affected by the edge-type of the nanoribbons. Moreover if we compare the edge of the nanoribbons with the one dimensional chains made by phenyls and diacetylenic units linked to these (as analyzed and reported in chapter 4) we can make interesting observations. Indeed we notice that the edge of the zigzag nanoribbons can be related to a single monodimensional chain of T type (meta-conjugation between diacetylenic linkages). From our theoretical investigation we have seen that T type chains have a very low π-electron delocalization resulting in a larger gap that decreases very slowly with the increase in the number of diacetylenic units (see Fig. 4.5 in chapter 4). On the other hand the edge of armchair nanoribbons corresponds to the single monodimensional chain of P type (para-conjugation between diacetylenic linkages), where conjugation has been found to extend at larger distances.

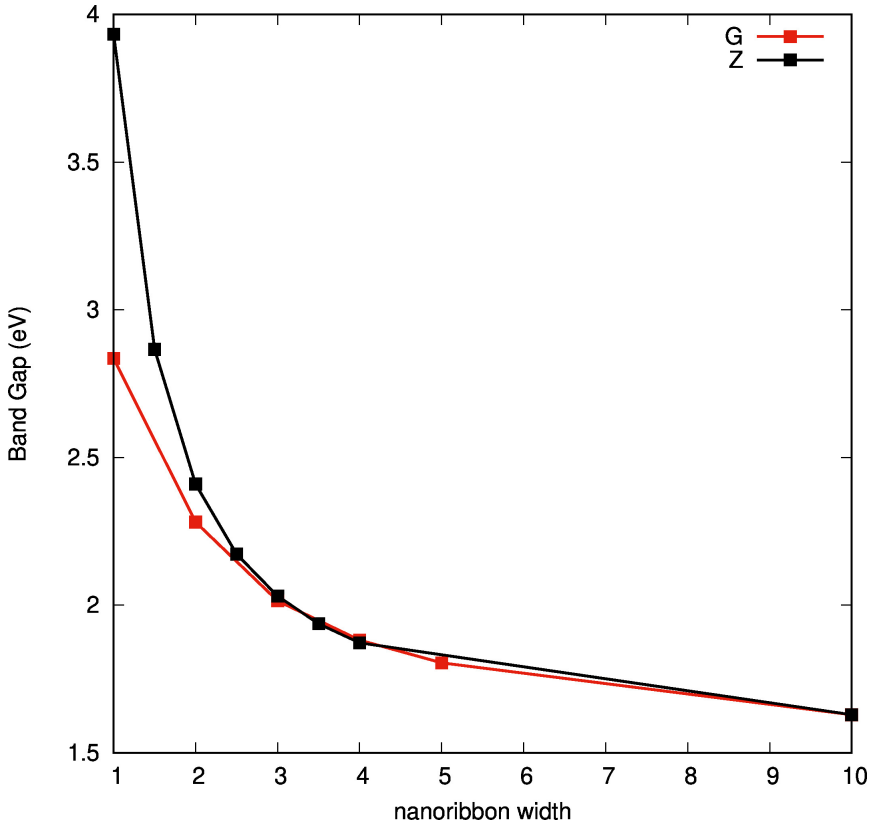

Figure 6.4: Trend in the band gap, for zigzag and armchair nanoribbons, depending on the increasing width (same nomenclature reported in Figs. 6.1, 6.2 for the width's definition). For n=10 we have reported the band gap of the infinite GDY as a reference.

Indeed analyzing our computational results, we have demonstrated that these chains possess a good π-electron delocalization and the band gap decreases rapidly with the increase of diacetylenic units. This effect affects the band gap of armchair nanoribbons, resulting in lower band gap values for these NRs with respect to the zigzag ones. Based on these results, I can conclude that the nanoribbons' edge plays an important role in determining π-electron delocalization, reflected by this influence on the band gap. Clearly this influence of the edge, as expected, rapidly decreases as the nanoribbons' width increases approaching the infinite 2D case. Already for n values higher than 3 we can observe, in Fig. 6.4, that both trends in the band gap collapses into one practically and they reach asymptotically the band gap value of the infinite GDY.

6.3 Analysis of the Raman spectra of zigzag and armchair GDY nanoribbons

The second focus on graphdiyne nanoribbons was the computation of the Raman spectra and their interpretation for both zigzag and armchair edges. Using the same approach adopted for the infinite GDY, CRYSTAL package was used exploiting the Coupled Perturbed Hartree Fock method to compute the Raman spectra of GDYNRs. The TOLDEE parameter was increased to 10 for this study, as required for an accurate prediction of this vibrational force fields. For simplicity, the analyzed spectra were divided depending on the nanoribbon edge type: armchair nanoribbons, integer number zigzag nanoribbons, half-integer number zigzag nanoribbons. This was done because each of the listed group has a different edge that corresponds to a different behaviour of the Raman spectra. For our analysis we neglect all the peaks located at wavenumber lower than 1400 cm^{-1} since they are not relevant for our discussion.

6.3.1 Armchair nanoribbons

At first we have analyzed Raman spectra of armchair nanoribbons. All the spectra are reported in Fig. 6.5, both for high and low wavenumbers, and they are compared with the Raman spectra of the infinite GDY and with the Raman spectra of the P monodimensional chain built by alternating sp^2 phenyls with diacetylenic sp units attached in para position between each other. From the analysis of the normal modes associated with the Raman peaks (Table 6.2) we obtain important results. We can start the analysis observing the low wavenumber Raman peaks for the P chain, that can be considered also as the G1 nanoribbon, comparing them with the armchair nanoribbons' ones. 2 peaks can be observed, one located at 1441 cm^{-1} and the other one located at 1681 cm^{-1}. Looking at the normal modes associated to these peaks, we notice that they are present also in all the armchair nanoribbons series but not in the infinite GDY. This is caused by the fact that they are normal modes localized on the edges of the nanoribbon (Fig. 6.6) and they disappear when there are no more edges in the structure. Therefore both these bands can be taken as marker bands of the presence of GDYNRs having finite width. Moreover these two peaks shift when we pass from the P chain to the first armchair nanoribbon (G2). This is caused by the appearence of other diacetylenic units attached to the phenyl groups, with resepct to the P chain, located at the edges that tends, thanks to the high electronegativity of sp-carbon, to

withdraw charge from the phenyls modifying the force constant of the associated normal modes and inducing the observed shift. In particular, increasing the nanoribbon's width from P to G2, the normal mode located at 1441 cm^{-1} shows a slight blue shift towards 1451 cm^{-1} while the normal mode at 1681 cm^{-1} suffers a red shift towards 1632 cm^{-1}. These normal modes are reported in Fig. 6.6. A more detailed analysis of the numerical values of the internal force constants associated to the CC stretching of the phenyls would be required for a better estimation of these effects.

Nanoribbon	Wavenumber(cm^{-1})	Raman activity(Å^4/amu)
P	1441	49101
	1681	323297
	2344	989038
G2	1451	146712
	1507	78114
	1632	641919
	2307	1492568
	2346	1087603
G3	1444	30748
	1452	99468
	1453	57669
	1499	373616
	1566	13178
	1571	212735
	1630	48792
	1630	561066
	2293	2763591
	2342	1592953
	2349	73400
G4	1452	129162
	1453	40041
	1495	778765
	1569	76620
	1571	170665
	1573	192893
	1630	157998
	1630	434647
	2287	4092539
	2312	382667
	2341	1874713
	2344	224908
G5	1452	51637
	1452	101022
	1493	1238503
	1570	82626
	1571	230668
	1573	312409
	1574	57612
	1630	169086
	1630	415534
	2268	295109
	2285	4861513
	2305	959491
	2341	1873400
	2341	726038
GDY	1490	869870
	1573	248923
	1573	248923
	2276	3707443
	2335	638183
	2335	638183

Table 6.2: Wavenumber and Raman activity of the most important peaks in different armchair nanoribbons

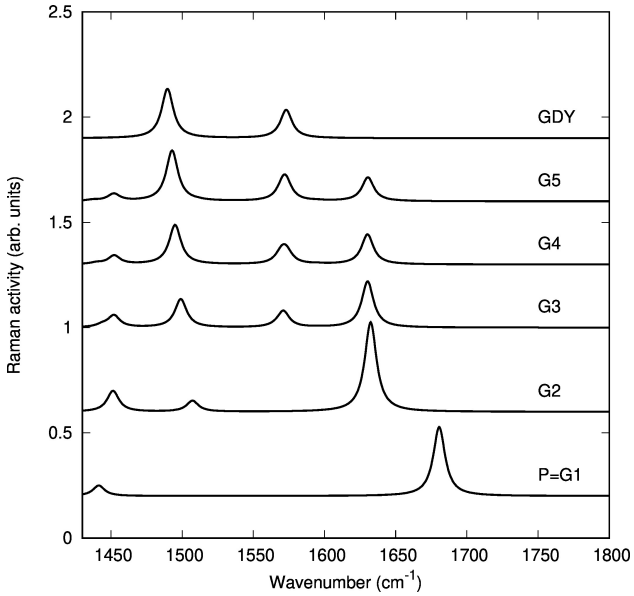

(a) Low wavenumber Raman spectra

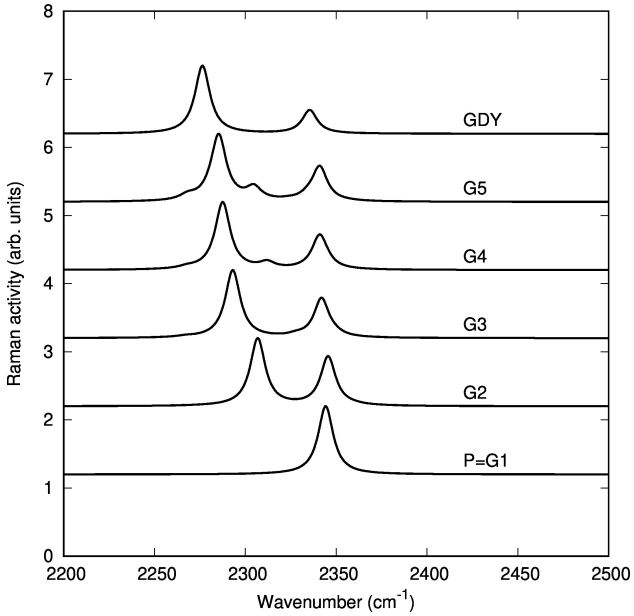

(b) High wavenumber Raman spectra

Figure 6.5: Computed Raman spectra for ANRs, infinite GDY and P chain. Both high and low wavenumber regions are reported

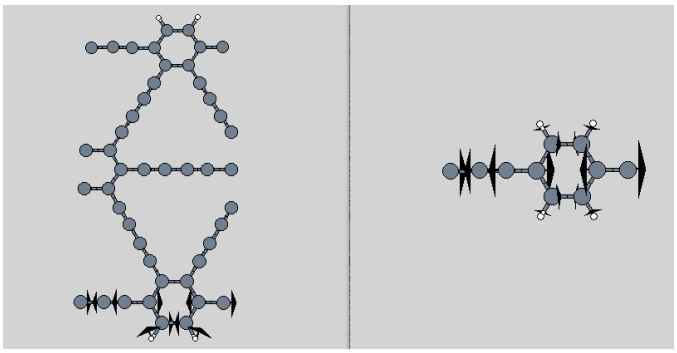

(a) Normal mode at 1441 cm^{-1}

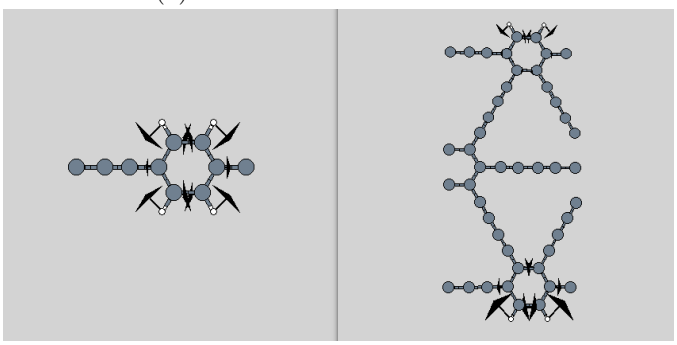

(b) Normal mode at 1681 cm^{-1}

Figure 6.6: Normal modes of the P chain, at 1441 cm^{-1} and at 1681 cm^{-1}, compared with the ones present in the G2 nanoribbon

Going from the P chain to G2 and then to G3 nanoribbons, we can distinguish in the Raman spectra the rise of two peaks that correspond to the G' and G peaks of the infinite graphdiyne (at 1490 cm^{-1} and 1573 cm^{-1} respectively, see Fig. 6.5). Indeed increasing the nanoribbons' width they become more and more intense until we approach the spectrum of GDY. Moreover the one at 1507 cm^{-1} of the G2 Raman spectra suffers a red shift increasing the nanoribbon's width, so going from G2 to G5 and then to the infinite GDY. What is also intereseting to see is that in the output of the normal modes' analysis, for the G3, G4 and G5 nanoribbons the G peak is described respectively by two , three and four different normal modes that are not degenerate as in the case of the infinite graphdiyne. In Table 6.3 frequencies and intensities of these normal modes are reported; the difference in wavenumber between them is also reported as $\Delta\nu$. This effect is caused by the confinement introduced in the nanoribbon and the change in the symmetry of GDYNR with respect to 2D-GDY. Passing from the 2D structure of the infinite GDY to the 1D structure of nanoribbons we introduce a distinction between the direction parallel to the principal

Table 6.3: Normal modes associated to the G peak in different armchair nanoribbons

Nanoribbon	Wavenumber (cm^{-1})	Raman activity(Å^4/amu)	$\Delta\nu$ (cm^{-1})
G3	1566	13178	
	1571	212735	5
G4	1569	76620	
	1571	170665	2
	1573	192893	2
G5	1570	82626	
	1571	230668	1
	1573	312409	2
	1574	57612	1
GDY	1573	248923	
	1573	248923	0

axis of the nanoribbon and perpendicular to it. This introduce a split in the degenerate normal modes associated to the G peak, and this split is decreasing the more we approach to the 2D GDY structure where the modes become degenerate. Normal modes associated to the G peak are reported in Fig. 6.7, 6.8, 6.9 for each armchair nanoribbon.

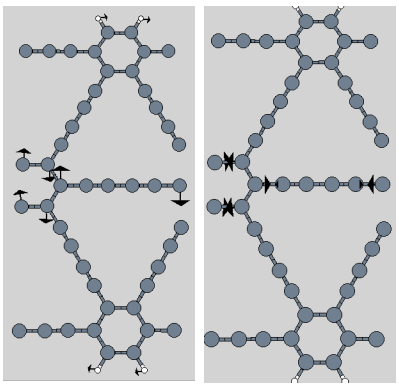

(a) 1566 cm^{-1} (b) 1571 cm^{-1}

Figure 6.7: Normal modes associated to the G peak for the G3 nanoribbon

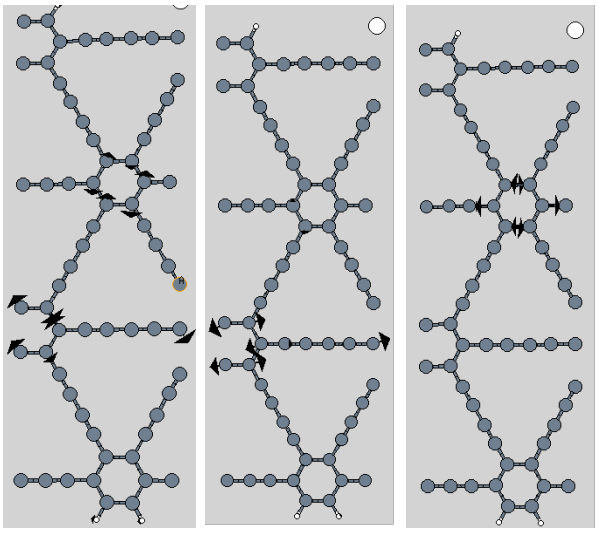

(a) 1569 cm^{-1} (b) 1571 cm^{-1} (c) 1573 cm^{-1}

Figure 6.8: Normal modes associated to the G peak for the G4 nanoribbon

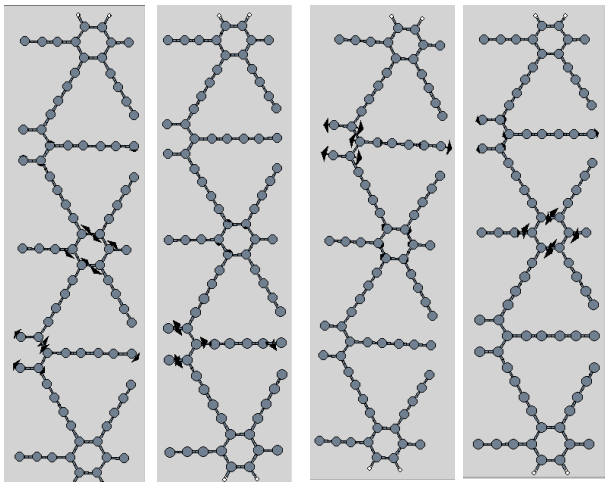

(a) 1569 cm^{-1} (b) 1571 cm^{-1} (c) 1572 cm^{-1} (d) 1573 cm^{-1}

Figure 6.9: Normal modes associated to the G peak for the G5 nanoribbon

Moving the analysis of the high wavenumber Raman spectra, in the P chain we can distinguish only one peak. It is located at 2344 cm^{-1}, and it is related to the stretching of the sp carbon atoms present in the structure. It is the ECC mode of a C_4 sp-carbon chain localized on the diacetylenic units between the phenyls (Fig. 6.10).

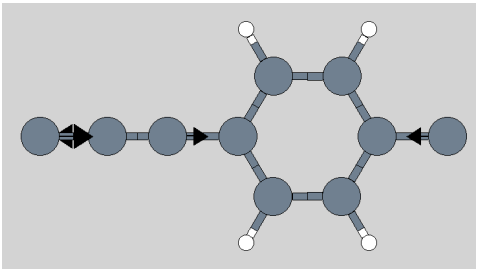

Figure 6.10: Normal mode associated to the peak at 2344 cm^{-1} for the P polymer

Analyzing G2, we can notice the same peak of the P chain at 2346 cm^{-1} but also the appearence of another peak, located at 2307 cm^{-1}. The normal modes associated to these two peaks are both connected to the ECC mode localized on single diacetylenic linkages, but with different phases one with respect to the other. Infact, observing the two normal modes reported in Fig. 6.11, it can be seen that they are very similar. But the vibrations of the diacetylenic units inside the nanoribbon, differently from the edge ones, are out of phase between each other. Moreover the peak at 2307 cm^{-1} is very sensitive to the nanoribbon's width. Infact going from G2 to G5 we can notice a red-shift of this peak while the other one remains practically in the same position.

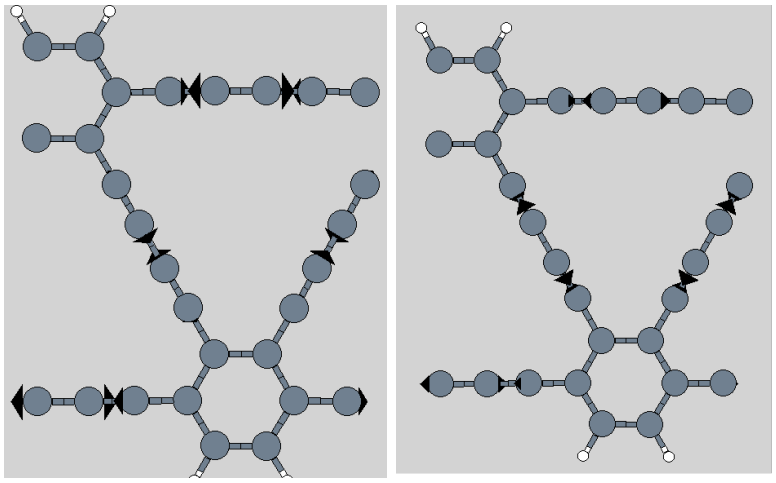

(a) 2345 cm^{-1} (b) 2306 cm^{-1}

Figure 6.11: Normal modes associated to the two peaks of the high wavenumber region for the G2 nanoribbon

6.3.2 Zigzag nanoribbons

The final analysis is focused on the Raman spectra calculation of integer number and half integer number zigzag nanoribbons. The computational parameters used are the same of the armchair nanoribbons' analysis. In Fig. 6.12, 6.13 Raman spectra of all zigzag nanoribbons, both for the low and high wavenumber regions, are reported. In the figures are also reported the Raman spectra of T type polymer for comparison, as in the case of armchair nanoribbons and P polymer. T monodimensional chains are built by alternating carbon atoms hexagons with diacetylenic units attached to each hexagon in meta-position and correspond to Z1 GDYNR. I start by analyzing the Raman spectra of the T chain: for what concern the low wavenumber region, we can distinguish three major peaks located at 1493 cm^{-1}, 1646 cm^{-1} and 1675 cm^{-1}. Visualizing the vibrational normal modes associated to these peaks we can observe that they are also present in the Z2 nanoribbon spectrum, in which two of them are shifted with respect to their position in the T polymer spectrum. Indeed the ones at 1675 cm^{-1} and at 1493 cm^{-1} show a red shift towards respectively 1627 cm^{-1} and 1459 cm^{-1} moving from the T chain to the Z2 nanoribbon. Increasing more the NR width, we can observe that the two peaks, passing to Z3 nanoribbon, show only a very slight red-shift. The shifts are due to the fact that these modes are strongly dependent on the width and on the increase of the diacetylenic units attached to the phenyl groups in the edge of the nanoribbon. Similar to what happened for armchair nanoribbons, the sp diacetylenic units tend to withdraw electronic charge, modifying the force constants associated to the bonds and causing the shifts. On the contrary, the peak at 1646 cm^{-1} is unaffected by the width of the nanoribbon and remains in the same position also for the other integer number zigzag nanoribbons. All the three peaks are connected to normal modes whose vibration is localized on the edge of the nanoribbon. Infact their intensity decreases the more the NR extension is increased, and they disappear for the case of the infinite GDY. Normal modes associated to these 3 peaks are illustrated in Fig. 6.18. When we extend the structure from T to Z2, we can observe the appearence of two intense peaks whose intensity increses with the increase of the nanoribbon's width. These resemble, as in the case of armchair nanoribbons, the G' and G peaks of the infinite graphdiyne and are not present in the polymer chain T. Analyzing the normal modes associated to these peaks, it can be observed that for the Z2 nanoribbon there is one normal mode associated to the peak at 1568 cm^{-1}. But when the extension of the nanoribbon is increased, so passing from Z2 to Z3, we can notice that the normal

modes associated to these peaks become two and they remain the same also going from Z3 to Z4.

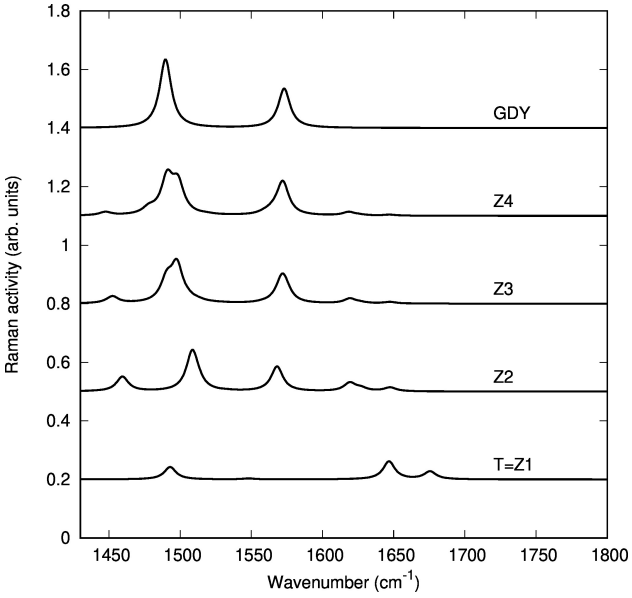

(a) Low wavenumbers Raman spectrum

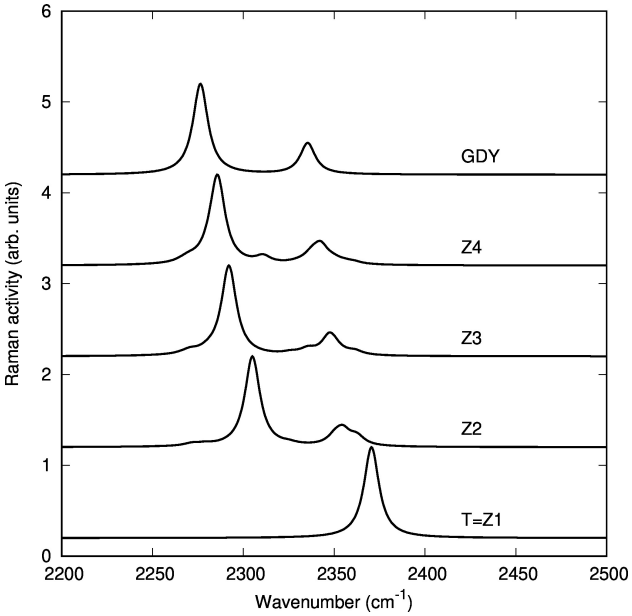

(b) High wavenumbers Raman spectrum

Figure 6.12: Raman spectra of integer number zigzag nanoribbons

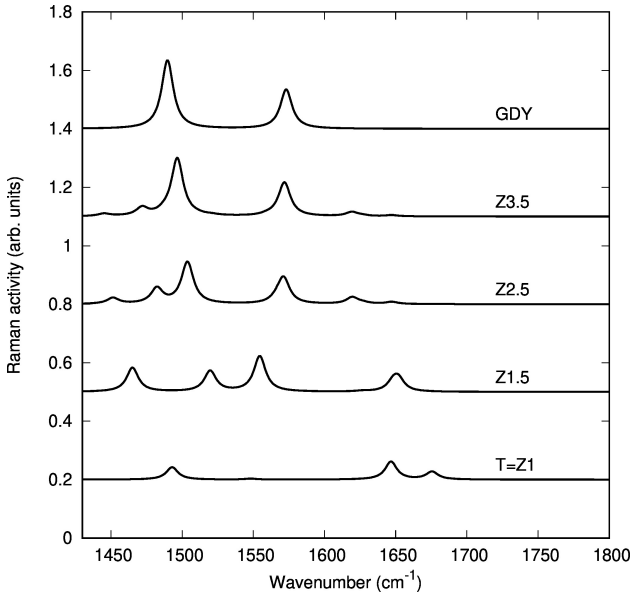

(a) Low wavenumbers Raman spectrum

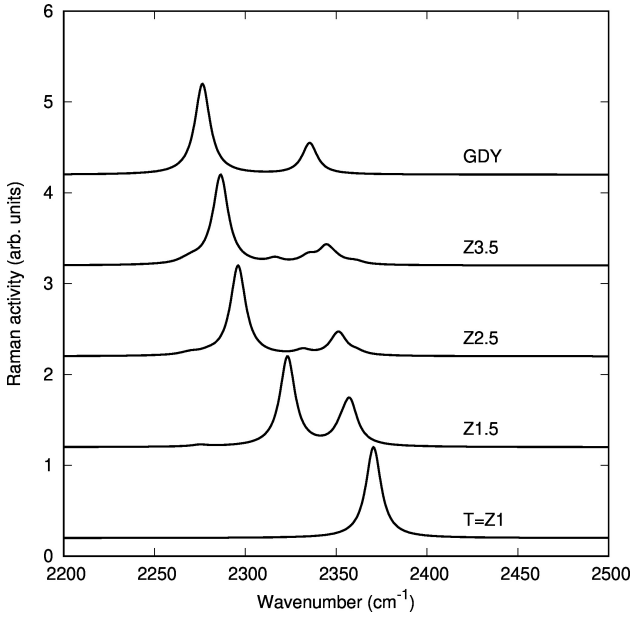

(b) High wavenumbers Raman spectrum

Figure 6.13: Raman spectra of half integer number zigzag nanoribbons

The explanation to this phenomenon is that moving from Z2 to Z3, we increase the number of phenyl groups inside the nanoribbon in which the vibration can occur. But when the width is increased more, going from Z3 to Z4, the vibration remains localized on the centre of the nanoribbon and it involves the same number of phenyls. As we

can see this peak does not show an appreciable shift in wavenumber increasing the NR extension and it tends to become the G peak when we reach the GDY structure. All these normal modes are reported in Fig. 6.15, 6.16, 6.17. Instead for the peak located at 1508 cm^{-1} in the Z2 Raman spectrum we can notice that it is generated from one normal mode reported in Fig. 6.19. But going from Z2 to Z3 this normal mode disappears and the peak is mainly originated from the contribution of two different normal modes, located at 1490 cm^{-1} and 1498 cm^{-1}. Vibrations associated to these normal modes are depicted in Fig. 6.20. For Z4 the normal modes that contribute to the rise of this peak become three, located at 1478 cm^{-1}, 1491 cm^{-1} and 1498 cm^{-1}. It is due to the fact that, for the normal modes of vibration localized in that range of wavenumbers, increasing the width of the nanoribbon the possible combinations of vibrations increase. These normal modes are reported in Fig. 6.21.

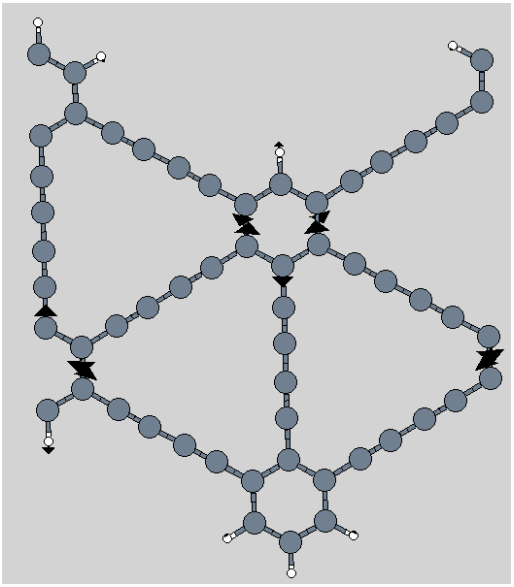

Figure 6.14: 1568 cm^{-1}

Figure 6.15: Normal mode of vibration of the Z2 nanoribbon, associated to the band at 1568 cm^{-1}

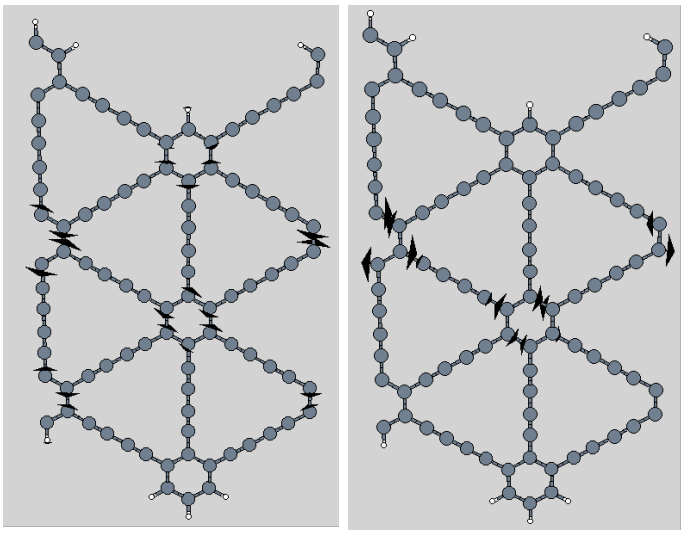

(a) 1571 cm^{-1} (b) 1574 cm^{-1}

Figure 6.16: Two normal modes of vibration of the Z3 nanoribbon, associated to the bands at 1571 cm^{-1} and 1574 cm^{-1}

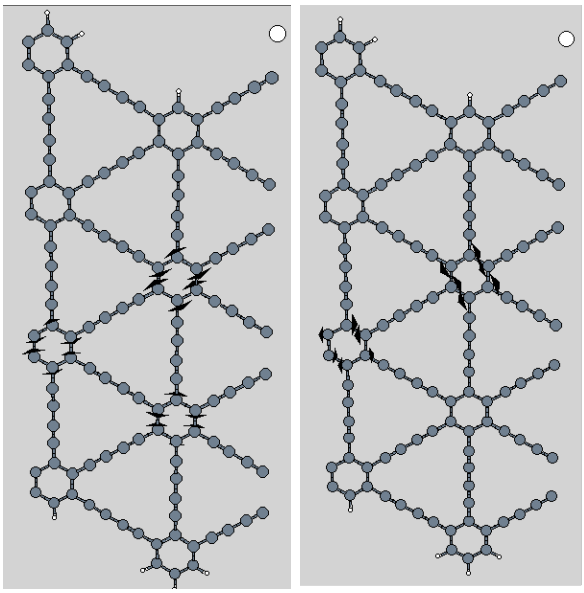

(a) 1572 cm^{-1} (b) 1573 cm^{-1}

Figure 6.17: Two normal modes of vibration of the Z4 nanoribbon, associated to the band at 1572 cm^{-1} and at 1573 cm^{-1}

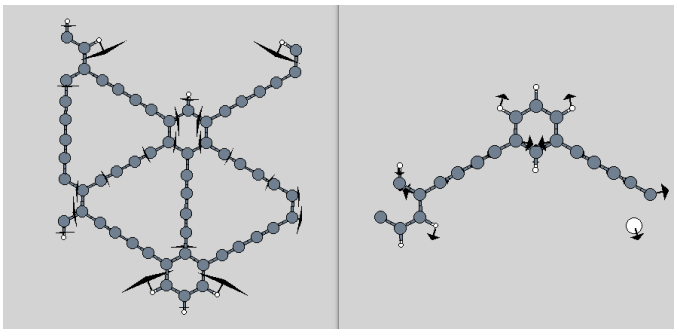

(a) 1493 cm^{-1}

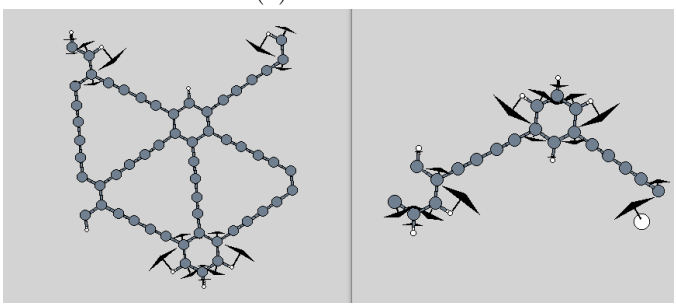

(b) 1646 cm^{-1}

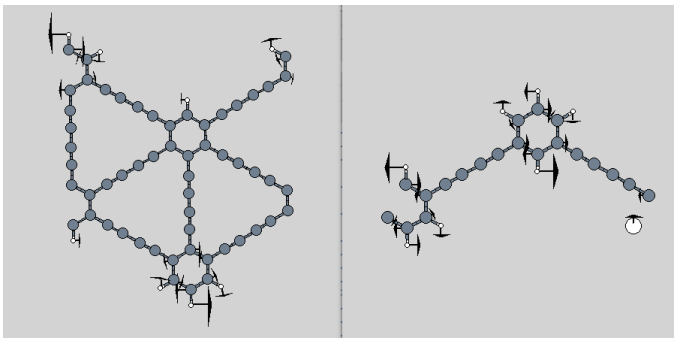

(c) 1675 cm^{-1}

Figure 6.18: Normal modes of vibration of the T polymer and the Z2 nanoribbon, associated to the band at 1493 cm^{-1}, 1646 cm^{-1} and 1675 cm^{-1} in the T polymer Raman spectrum

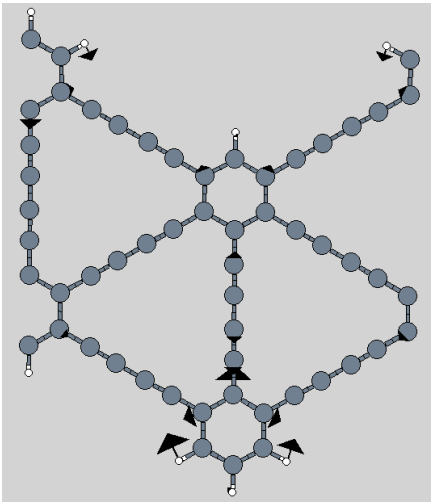

Figure 6.19: Normal mode of vibration of the Z2 nanoribbon, associated to the band at 1508 cm^{-1}

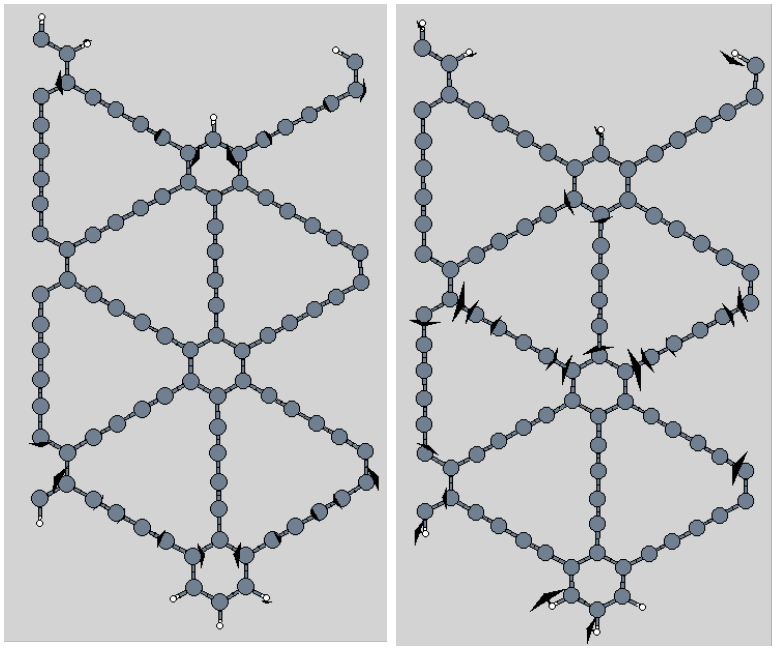

(a) 1490 cm^{-1} (b) 1497 cm^{-1}

Figure 6.20: Two normal modes of vibration of the Z3 nanoribbon, associated to the bands at 1490 cm^{-1} and 1497 cm^{-1}

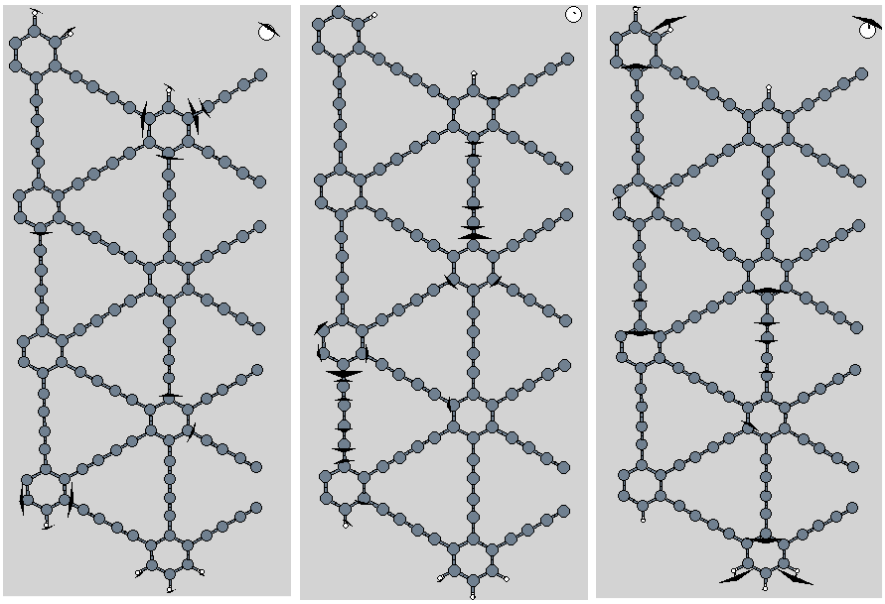

(a) 1478 cm^{-1} (b) 1491 cm^{-1} (c) 1498 cm^{-1}

Figure 6.21: Normal modes of vibration of the Z4 nanoribbon, associated to the bands at 1478 cm^{-1}, 1491 cm^{-1} and 1498 cm^{-1}

For the half integer zigzag nanoribbons the behaviour is similar. In this case, going from T to Z1.5 we observe that the peak at 1646 cm^{-1} does not shift, as in the case of Z2, and the peak at 1493 cm^{-1} shifts towards 1465 cm^{-1}. The same shifts are present also between Z1.5 and Z2.5. It is interesting to notice that the intensity of the second peak increases from T to Z1.5, while passing from Z1.5 to Z2.5 and from Z2.5 to Z3.5 it decreases and becomes less intense with respect to the T polymer. Analyzing the peak at 1675 cm^{-1}, it seems to disappear going from T to Z1.5 and it reappears in the Z2.5 spectrum shifted to 1619 cm^{-1}. Studying the normal modes associated to this peak it can be seen that in Z1.5 nanoribbon this normal mode is present at 1652 cm^{-1} and so its intensity overlaps with the intensity of the line at 1648 cm^{-1} and they cannot be distinguished as two separate lorentian peaks. As in the case of integer number zigzag nanoribbons these modes are edge modes and tend to disappear the more we increase the NR extension, approaching the structure of the infinite slab of graphdiyne. The edge normal modes are reported in Fig. 6.22 for the Z1.5 nanoribbon. The remaining two peaks of the Z1.5 nanoribbon, located at 1520 cm^{-1} and 1554 cm^{-1}, are generated by two bulk normal modes rapresented in Fig. 6.23. As we can see, the normal mode associated to the peak at 1554 cm^{-1} is the same that we have for Z2 (1568 cm^{-1}) and in the

others integer number zigzag nanoribbons, but it is slightly shifted to smaller wavenumbers while the normal mode associated to the peak at 1520 cm^{-1} is present also in Z2 and it is the one at 1508 cm^{-1}, so slightly shifted to higher wavenumbers. Increasing the width and passing to analyze the Raman spectra of the Z2.5 nanoribbon it can be noticed that the the normal mode associated to the peak at 1571 cm^{-1} corresponds to the one of the Z1.5 NR located at 1554 cm^{-1}; it appears shifted and it reaches also the same wavenumber value that it has in both armchair and integer number zigzag nanoribbons. Observing the Raman spectra of Z2.5 we notice also that instead of the peak that was present in Z1.5 at 1520 cm^{-1} we can observe two peaks, located at 1482 cm^{-1} and at 1503 cm^{-1}. Analyzing the normal modes associated to these peaks, we can state that they are generated by 2 similar normal modes, whose vibrations are reported in Fig. 6.24, and they coincide with the normal mode associated to the peak located at 1520 cm^{-1} of the Z1.5 nanoribbon. It splits in two different modes associated to two different peaks. Infact in Z2.5 nanoribbon we have an alternated width along the periodic direction, alternating two phenyls and one diacetylenic unit with three phenyls and two diacetylenic units. The first peak (1482 cm^{-1}) is localized on the thinner part, the one with a single diacetylenic unit, while the second one (1503 cm^{-1}) is localized on the thicker part of the nanoribbon, the one with two diacetylenic units; this is the reason why they can be seen as two distinct peaks located at different frequencies. Going more in detail, the peak located at 1503 cm^{-1} takes the contribution to its intensity also from another normal mode, located at 1505 cm^{-1}, and reported in Fig. 6.25. Increasing the extension of the structure it can be seen this peak tend to disappear, as we can see in Z3.5 and in the infinite GDY, in which it is absent.

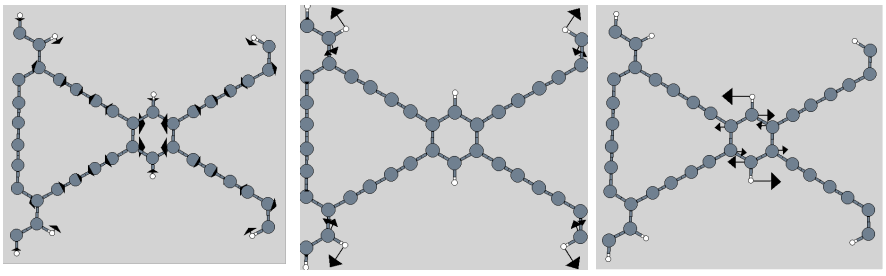

(a) 1465 cm^{-1} (b) 1648 cm^{-1} (c) 1652 cm^{-1}

Figure 6.22: Normal modes of vibration of the Z1.5 nanoribbon, associated to the bands at 1465 cm^{-1}, 1648 cm^{-1} and 1652 cm^{-1}

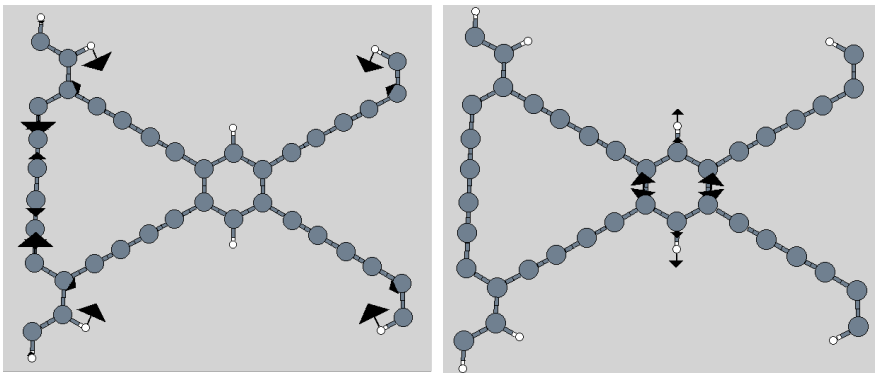

(a) 1520 cm^{-1} (b) 1554 cm^{-1}

Figure 6.23: Two bulk normal modes of vibration of the Z1,5 nanoribbon, associated to the bands at 1520 cm^{-1} and at 1554 cm^{-1}

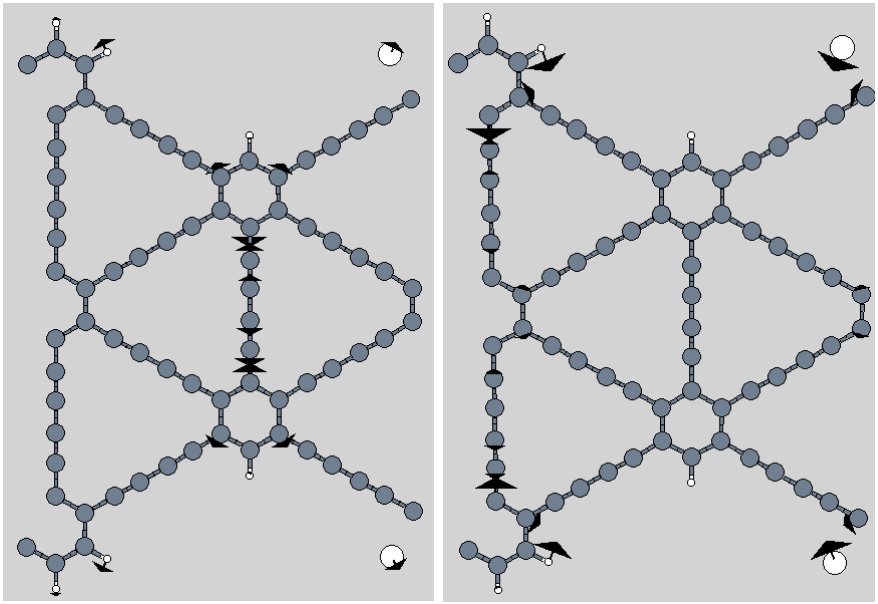

(a) 1482 cm^{-1} (b) 1503 cm^{-1}

Figure 6.24: Two bulk normal modes of vibration of the Z2,5 nanoribbon, associated to the bands at 1482 cm^{-1} and at 1503 cm^{-1}

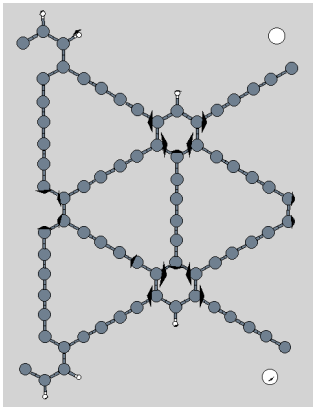

Figure 6.25: Normal mode of vibration of the Z2,5 nanoribbon, associated to the band at 1505 cm^{-1}

Moving the discussion towards the high wavenumber region, at first we can analyze the case of integer number zigzag nanoribbons. Observing the high wavenumber region of the Raman spectra for the T chain and the different nanoribbons we can do important observation. The first is that for the T polymer we have one only peak located at 2371 cm^{-1} and the normal mode associated to this peak is reported in Fig. 6.26. It is an ECC mode localized on the diacetylenic units in which the vibrations are all in phase between each other. Going from T to Z2 we observe one well defined peak at 2305 cm^{-1}, originated from a single normal mode (Fig. 6.27), and a very broad peak that is originated by the contribution of three different normal modes located at 2350 cm^{-1}, 2355 cm^{-1} and 2363 cm^{-1} (Fig. 6.28). The first well defined peak, increasing the width going from Z2 to Z3 and Z4, shifts resepctevely to 2292 cm^{-1} and to 2285 cm^{-1}. The broad peak tends to shift at lower wavenumbers and becomes a single well defined peak in the case of infinite GDY. Concerning the half integer number zigzag nanoribbons, in the Z1.5 nanoribbon two peaks can be distinguished from the Raman spectra, one located at 2323 cm^{-1} and the other one located at 2357 cm^{-1}. Normal modes associated to these peaks are illustrated in Fig. 6.29. They are both rapresented by ECC modes localized on single diacetylenic units, but with different relative phases. Analyzing Z2.5 and Z3.5 we can see that the peak of Z1.5 at 2323 cm^{-1} shifts towards lower wavenumber (2296 cm^{-1} for Z2.5 and 2286 cm^{-1} for Z3.5) but the normal mode that gives rise to this peak remains practically the same (Fig. 6.29). Now considering the peak at 2357 cm^{-1} of the Z1.5 NR, it can be noticed that in the Raman spectra of the Z2.5 and Z3.5 nanoribbons this peak becomes broader, due to the superposition of different lorentian lines, and it tends to shift to lower wavenumbers.

The main normal modes that give rise to this broad band are reported in Fig. 6.31 and Fig. 6.30 for Z2.5 and Z3.5 respectively.

All the normal modes that we have talken about for zigzag nanoribbons are reported in Table 6.4 in terms of wavenumber and intensity associated to each single mode.

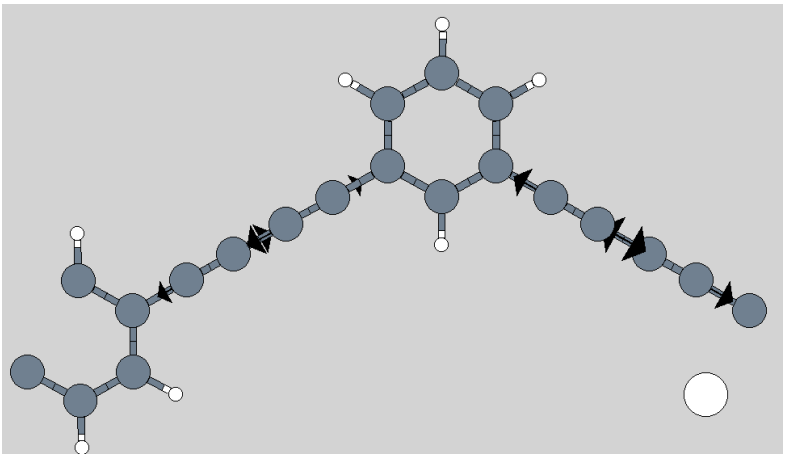

Figure 6.26: Normal mode of vibration of the T polymer in the high wavenumber region, associated to the band at 2371 cm^{-1}

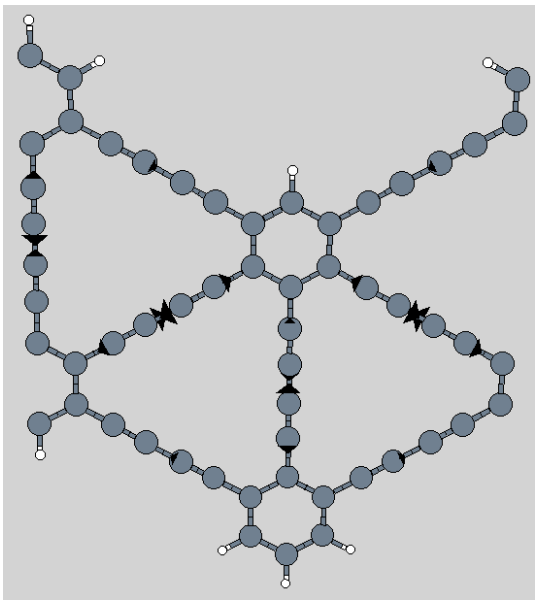

Figure 6.27: Normal mode of vibration of the Z2 polymer in the high wavenumber region, associated to the band at at 2305 cm^{-1}

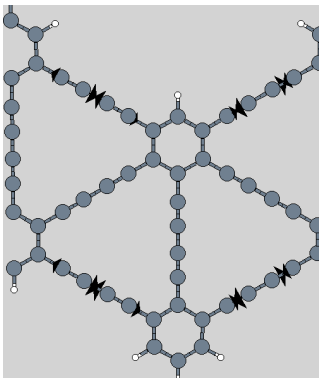

(a) 2350 cm^{-1}

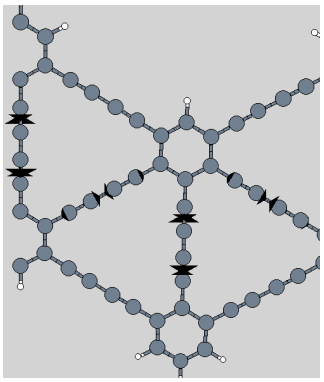

(b) 2355 cm^{-1}

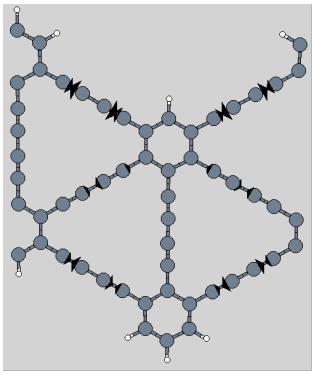

(c) 2364 cm^{-1}

Figure 6.28: Normal modes of vibration, in the high wavenumber region, of the Z2 nanoribbon, associated to the bands at 2350 cm^{-1}, 2355 cm^{-1} and 2363 cm^{-1}

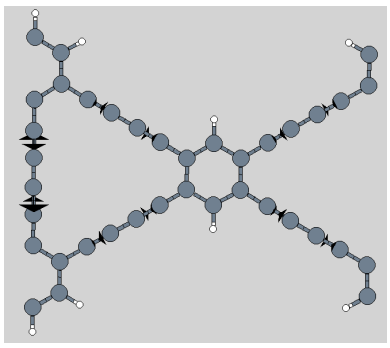

(a) 2323 cm^{-1}

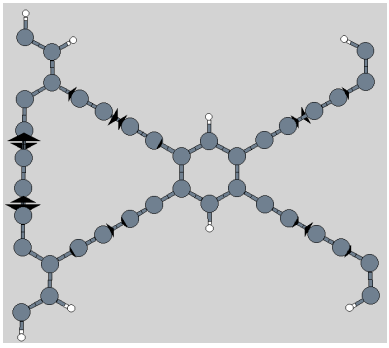

(b) 2357 cm^{-1}

Figure 6.29: Two normal modes of vibration in the high wavenumber region of the Z1,5 nanoribbon, associated to the bands at 2323 cm^{-1} and at 2357 cm^{-1}

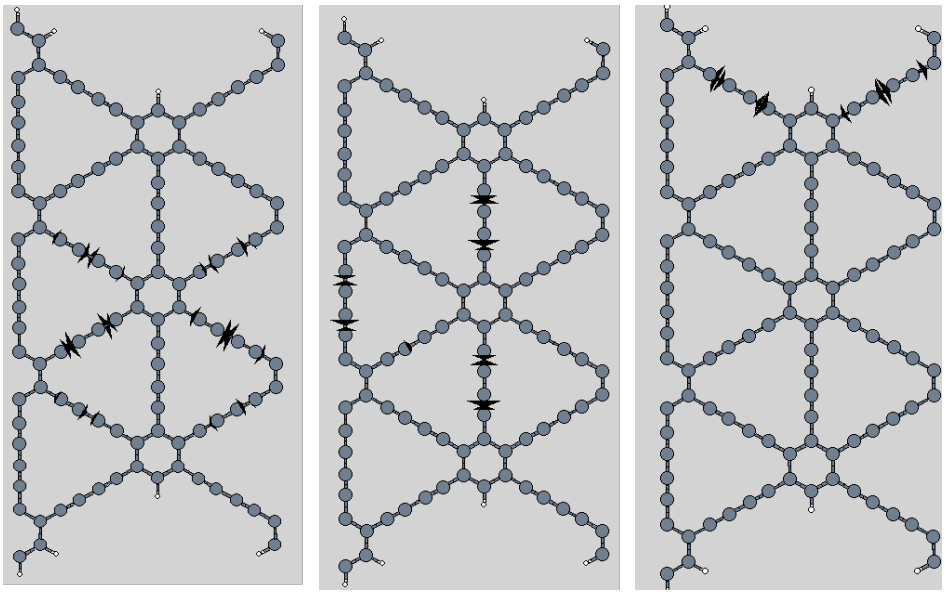

(a) 2335 cm^{-1} (b) 2344 cm^{-1} (c) 2349 cm^{-1}

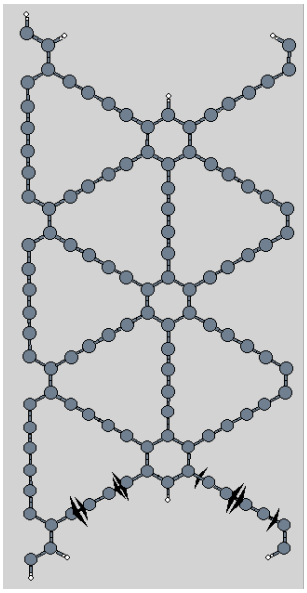

(d) 2350 cm^{-1}

Figure 6.30: Normal modes of vibration for the Z3.5 nanoribbon, associated to the bands at 2335 cm^{-1}, 2344 cm^{-1}, 2349 cm^{-1} and 2350 cm^{-1}

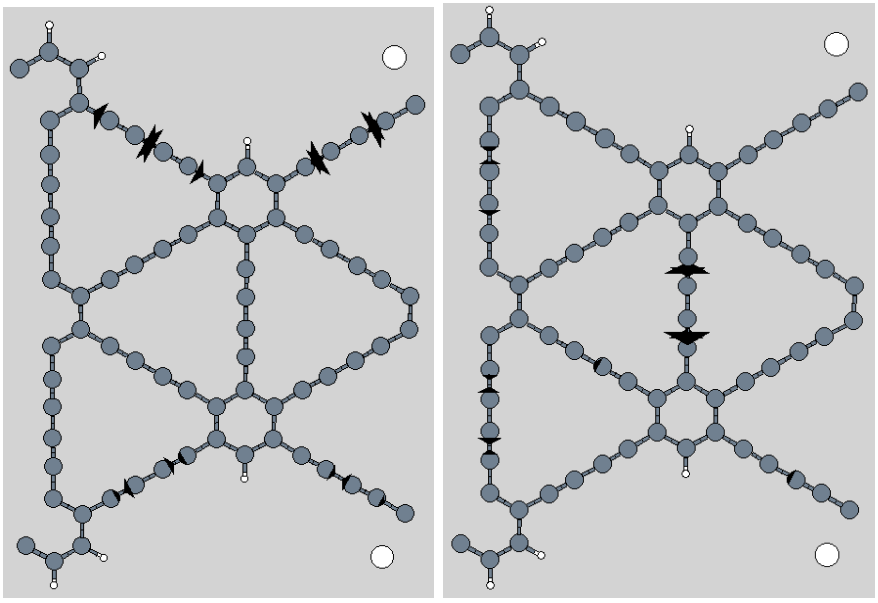

(a) 2349 cm^{-1} (b) 2352 cm^{-1}

Figure 6.31: Two normal modes of vibration of the Z2.5 nanoribbon, associated to the bands at 2349 cm^{-1} and at 2352 cm^{-1}

Nanoribbon	Wavenumber(cm^{-1})	Raman activity(Å^4/amu)
T	1493	9087
	1647	13145
	2371	186541
Z1.5	1465	61987
	1520	52518
	1554	91582
	1648	22909
	1652	29921
	2323	745668
	2357	349443
Z2	1459	102459
	1508	255891
	1568	173770
	1627	19503
	2305	2045253
	2350	181866
	2355	316037
	2363	194422
Z2.5	1451	72172
	1482	184683
	1503	363979
	1505	149406
	1571	298399
	1619	78578
	2296	3529357
	2349	197958
	2352	719752
Z3	1490	367911
	1498	631708
	1506	73400
	1571	391265
	1574	147705
	2292	4984466
Z3.5	1472	178615
	1497	1268944
	2286	6450872
	2335	550155
	2344	1205036
	2349	157107
	2350	117830
Z4	1478	154008
	1491	987170
	1498	817532
	1572	620648
	1573	268823
	2285	7608589
	2343	1571803
GDY	1490	869870
	1573	248923
	1573	248923
	2276	3707443
	2335	638183
	2335	638183

Table 6.4: Normal modes associated to the most important peaks in different zigzag nanoribbons

6.3.3 Comparison between Raman spectra of different edge-type nanoribbons

The final analysis carried out on nanoribbons is the comparison between Raman spectra of zigzag and armchair NRs to understand if they can be distinguished only by analyzing the Raman spectra. The study was done in order to find a possible characterization tool to discriminate between zigzag and armchair nanoribbons based on Raman marker bands. To clearly visualize the peaks associated to each Raman spectra and see the differences between different edge-type nanoribbons, G3, Z3 and Z2.5 are taken into account to focus on a peculiar NR width which is neither too short nor too large. This choice is due to the fact that peaks associated to vibration localized on the edges decrease their intensity increasing the nanoribbon's width and thus their marker bands would decrease in intensity. Furthermore the armchair series, G3 is the first nanoribbon in which the G peak is visible. In Fig. 6.32 the Raman spectra of these nanoribbons are compared, including the Raman spectra of the infinite GDY as a reference, both for high and low wavenumbers. Focusing the attention on the low wavenumber region of the Raman spectra, we can effectively distinguish between armchair, integer number and half integer number zigzag nanoribbons. At first it can be observed that the G3 armchair nanoribbon has a very high and well defined peak at 1630 cm^{-1} while Z3 and Z2.5, in the same region, are characterized by two distinct and small peaks, located at 1627 cm^{-1} and 1647 cm^{-1}. These peaks can be taken as markers to distinguish the two different edge-type nanoribbons. Moreover, looking at the same low wavenumber region, it is also possible to discriminate between half integer number and integer number zigzag nanoribbons. Infact, analyzing the peak G' of the infinite graphdiyne, it can be noticed that in the same region for the integer number zigzag nanoribbon Z2 we observe only one band, originated by the superposition of two normal modes located at 1490 cm^{-1} and at 1498 cm^{-1}. Looking at the Raman spectra of the half integer number zigzag nanoribbon Z2.5, in the same range of wavenumber two distinct peaks can be seen, one located at 1482 cm^{-1} 1503 cm^{-1}. Normal modes associated to these peaks are depicted in Fig. 6.33, 6.34. This diversity between the two Raman spectra can be taken as a marker of the two type of zigzag nanoribbons. Only the case of Z1.5, not reported here but shown in Fig. 6.13, is an exception: infact this nanoribbon does not present the two peaks in the wavenumber range of the G' peak. However it can be easily detected due the fact that its spectra is quite different with resepct to all the other zigzag nanoribbons (see Fig. 6.13) due to its peculiar very confined structure. Concerning the high wavenumber

Raman spectra, is quite difficult to discriminate between armchair or zigzag nanoribbon. The general trend for the two bands that can be distinguished for all the nanoribbons in this region is their shift towards lower wavenumber with the increase of the nanoribbon's width, but this doesn't allow to discriminate safely different edge types. Analyzing this region, it could be possible to carry out only a qualitative evaluation between nanoribbons with different width (Fig. 6.32).

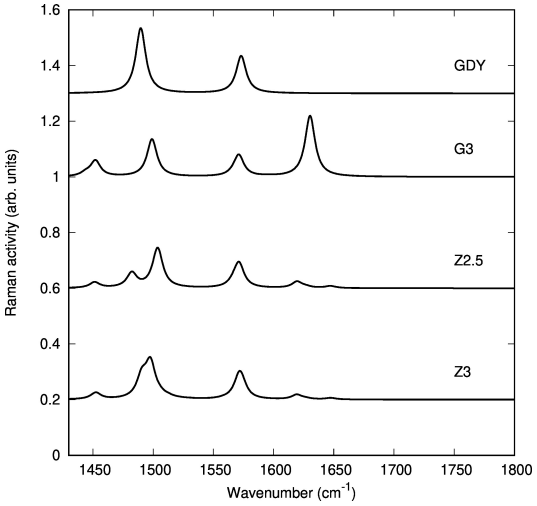

(a) Low wavenumbers Raman spectra

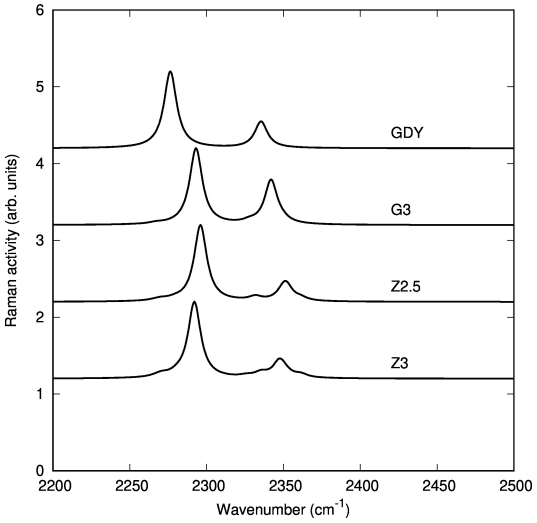

(b) High wavenumbers Raman spectra

Figure 6.32: Comparison between Raman spectra of zigzag and armchair nanoribbons, both for high and low wavenumber regions.

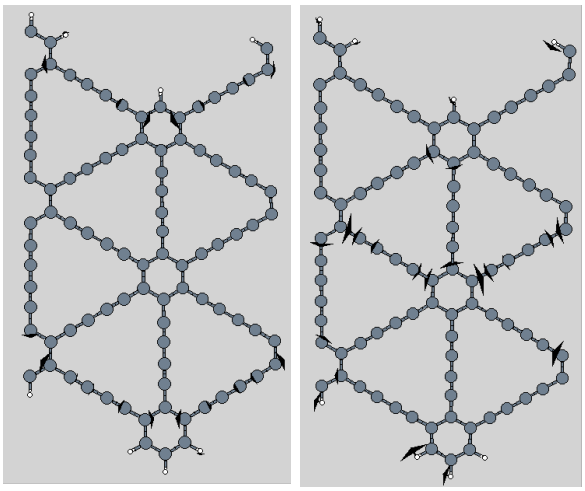

(a) 1490 cm^{-1} (b) 1497 cm^{-1}

Figure 6.33: Two normal modes of vibration of the Z3 nanoribbon, associated to the bands at 1490 cm^{-1} and 1497 cm^{-1}

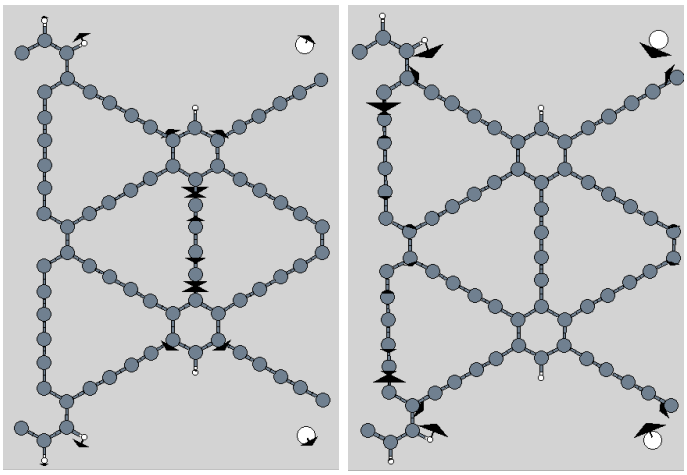

(a) 1482 cm^{-1} (b) 1503 cm^{-1}

Figure 6.34: Two bulk normal modes of vibration of the Z2,5 nanoribbon, associated to the bands at 1482 cm^{-1} and at 1503 cm^{-1}

6.3.4 Conclusions

Based on the data and the discussion reported above I summarize here the main results obtained:

- From the analysis of the band structure of both armchair and zigzag nanoribbons, I have understood that, as reported in litera-

ture, the band gap decreases as the nanoribbon's width increases. Moreover armchair nanoribbons, for short width, have a lower band gap with respect to the zigzag ones, consistent with the more delocalized character of para-conjugated edges.

- From the analysis of the Raman spectra and the normal modes associated to the peaks, it has been possible to better understand the effect of confinement introduced in the nanoribbons with respect to the 2D-GDY. Moreove, it has been possible to detect certain bands, whose normal modes are associated to the edge of the nanoribbon and that can be taken as markers of this type of nanostructure.

- From a comparison between the Raman spectra of armchair, integer number and half integer number zigzag nanoribbons it has been possible to distinguish marker bands that can be useful to discriminate between different edge-type nanoribbons.

The obtained results are very interesting and in literature the Raman spectra has been analyzed and computed only for infinite 2D GDY and GY. Considering nanoribbons there are no works about the discussion and the interpretation of Raman spectra. The analysis of the normal modes associated to the Raman peaks can be very useful to better understand intramolecular properties of GDYNRs, including π-conjugation effects, and how the different edges can affect these properties. Moreover, Raman turned out to be an optimum characterization tool for these structures, and can be very helpful for researchers that need to characterize these peculiar sp-sp^2 carbon-based nanostructures.

Chapter 7

Conclusions and future perspectives

In conclusion, in my thesis work I have done a computational investigation, by means of density functional theory, of hybrid sp-sp^2 carbon nanostructures. At first, linear molecules and molecular fragments made by phenyl groups connected by diacetylenic units have been studied by means of the GAUSSIAN09 package. The aim of this analysis was to investigate the electronic properties of these systems, in terms of π-conjugation effects. With the evaluation of their band gap, and how it can change depending on the type of conjugation (para, meta and ortho) of the diacetylenic linkages with respect to the phenyl groups, a careful analysis has been carried out for many fragments, including a few experimentally-available molecules. For the one dimensional chains characterized by different conjugations and different lengths, I have discovered that the polymer with para-conjugation (P series) is the one among the other linear polymeric chains characterized by the highest π-conjugation, resulting in lower values of band gap the more number of diacetylenic units is increased. On the other hand, meta-conjugation breaks the π-electron delocalization, stabilyzing high band gap even with increasing the number of the diacetylenic units. The ortho-conjugation has an intermediate effect on the gap that is not negligible. What I also found is that in the series that rapresents the smallest example of armchair nanoribbon (S series), the π-conjugation is very effecttive and I predicted the lowest band gap values for this series, with a plateau that is reached only for a very high number of diacetylenic units. By analyzing the different molecular fragments, we have proved that the para conjugation is the most effective in affecting the band gap of these structures, as Tahara previously investigated for the case of graphyne fragments [35]. In addition we verified that ortho-

conjugation gives a non negligible contribution in lowering the gap of the fragments. While structures where the combination of the ortho and the para conjugtion is possible, the band gap decreases significantly. Moreover the formation of rings formed by phenyl and chain in a triangular geometry (the basic units of γ-graphdiyne), further, lowers the gap and increases the electron delocalization in the nanostructures. Based on the analysis for finite dimension molecular fragments, I moved to the analysis of periodic structures using the CRYSTAL14 and CRYSTAL17 packages. At first I have studied electronic and vibrational properties of the infinite γ-graphdiyne (GDY). To study electronic properties, the band structure of the infinite GDY was computed (1.629 eV). After that, I computed the Raman and IR spectra for this ideal reference structure. I have analyzed the most important peaks occurring in the Raman and IR spectra, giving a detailed description of the normal modes associated to these peaks. This evaluation was preliminary for the study of grahdiyne-based nanoribbons made by cutting the 2D-γ-GDY along specific directions. Depending on the edge type originated by cutting the crystal, armchair or zigzag nanoribbons can be obtained. My focus on nanoribbons was motivated by the fact that these systems are very promising concerning the possibility to produce them by proper preparation techniques but there are few studies on these type of structures reported in literature, in particular concerning their characterization by Raman spectroscopy. First, I computed the band structure for armchair an zigzag nanoribbons with different width. The result is that increasing the nanoribbons' width (thus approaching the limit of GDY) the band gap tends to decrease as already reported in literature [20]. In particular, I noticed that, for small value of the width, armchair nanoribbons have a lower band gap with respect to the zigzag ones as a consequence of the conjugation effects highlighted for the one dimensional chains discussed in the first part. This can be explained analyzing the edge of these strutures: the armchair nanoribbons have the para conjugated monodimensional chain (P) as the edge, while zigzag nanoribbons have the meta conjugated one (T). As alredy commented, the P chain gives an higher π-electron delocalization to the armchair nanoribbon with respect to the T chain that contributes with a much lower delocalization. I then moved to the computation of the Raman spectra for armchair, integer number and half integer number zigzag nanoribbons. The main bands for different edge nanoribbons were studied in detail, including also the analysis of the normal modes associated to that peaks. We found various peaks whose normal modes are associated to vibrations localized at the edge of the structures and whose intensity tends to decrease increasing the

NR width and approaching the GDY structure for all the nanoribbons. These bands can be taken as relevant marker bands for the occurring of confinement effects. I have also analyzed the evolution of the peaks, increasing more and more the width of the NR, evolving towards the main bands of the infinite GDY. Finally I compared zigzag and armchair nanoribbons to understand if there is a way to distinguish them from the Raman spectra, in order to use these spectra as a useful characterization tool. Also to detect the edge-type of GDYNRs actually I was able to notice one single peak, located in the low wavenumber region, that is present only in armchair nanoribbons and can be used to distinguish between armchair and zigzag ones. Moreover, analyzing the splitting of one band in the integer number zigzag nanoribbons dividing into two distinct peaks in half integer number zigzag nanoribbons, it is possible to distinguish these two different edges nanoribbons.

Based on these results, various perspectives of my work can be opened. The first future investigation is to extend the dimension of the studied fragments and nanoribbons to understand how the electronic and vibrational properties evolve and can be tuned. Another aspect is the extension of this work to nanostructures with other different topologies. Indeed fragments and nanoribbons based on different graphdiyne type (for example α or β graphdiynes) should be studied in details. The same analysis can be also extended to structures with longer sp-carbon based linkages, as graphtriyne, graphfouryne and so on, to understand how the increase in the length of these units can affect the properties. Finally, a large variety of other hybrid sp-sp^2 structures, different from graphyne, graphdiyne and so on, can be indeed designed and it would be interesting to understand if there are other topologies that are promising and how their electronic and vibrational properties can change.

List of Figures

List of Tables

Bibliography

[1] A. Hirsch. The era of carbon allotropes. *Nature materials*, 9:868–71, 11 2010.

[2] R.H. Baughman. Dangerously seeking linear carbon. *Science*, 312(5776):1009–1010, 2006. cited By 72.

[3] C.S. Casari and A. Milani. Carbyne: from the elusive allotrope to stable carbon atom wires. *ArXiv e-prints*, January 2018.

[4] F. Cataldo. *Polyynes: Synthesis, Properties and Applications*. Boca Raton, CRC press, 2005.

[5] F. Diederich and M. Kivala. All-carbon scaffolds by rational design. *Advanced Materials*, 22(7):803–812.

[6] W.A. Chalifoux and R.R. Tykwinski. Synthesis of polyynes to model the sp-carbon allotrope carbyne. *Nature Chemistry*, 2(11):967–971, 2010.

[7] S. Yang and M. Kertesz. Linear cn clusters: are they acetylenic or cumulenic? *The Journal of Physical Chemistry A*, 112(1):146–151, 2008.

[8] D. Fazzi M. Tommasini C. Castiglioni W.A. Chalifoux N. R. Agarwal, A. Lucotti and R. R. Tykwinski. Structure and chain polarization of long polyynes investigated with infrared and raman spectroscopy. *Journal of Raman Spectroscopy*, 44(10):1398–1410.

[9] F. Cataldo, I.E. Castelli N. Manini G. Onida L. Ravagnan, E. Cinquanta, and P. Milani. Synthesis, characterization, and modeling of naphthyl-terminated sp carbon chains: Dinaphthylpolyynes. *The Journal of Physical Chemistry B*, 114(46):14834–14841, 2010.

[10] R.R. Tykwinski A. Milani C.S. Casari, M. Tommasini. Carbon-atom wires: 1-d systems with tunable properties. *Nanoscale*, 8:4414–4435, 2016.

[11] V. Barbieri A. Lucotti V. Russo F. Cataldo C.S. Casari A. Milani, M. Tommasini. Semiconductor-to-metal transition in carbon-atom wires driven by sp2 conjugated end groups. *The Journal of Physical Chemistry C*, 121(19):10562–10570, 2017.

[12] C.D. Methfessel F. Hampel J.A. Januszewski, D. Wendinger and R.R. Tykwinski. Synthesis and structure of tetraarylcumulenes: Characterization of bond-length alternation versus molecule length. *Angewandte Chemie International Edition*, 52(6):1817–1821, 2013.

[13] S.C. Brand M.M. Haley and J.J. Pak. Carbon networks based on dehydrobenzoannulenes: Synthesis of graphdiyne substructures. *Angewandte Chemie International Edition in English*, 36(8):836–838.

[14] H. Ma C. Yuan Q. Sun, L. Cai and W. Xu. Dehalogenative homocoupling of terminal alkynyl bromides on au(111): Incorporation of acetylenic scaffolding into surface nanostructures. *ACS Nano*, 10(7):7023–7030, 2016.

[15] A.L. Ivanovskii. Graphynes and graphdyines. *Progress in Solid State Chemistry*, 41(1):1 – 19, 2013.

[16] H. Liu Y. Li, L. Xu and Y. Li. Graphdiyne and graphyne: from theoretical predictions to practical construction. *Chem. Soc. Rev.*, 43:2572–2586, 2014.

[17] D.L.Mafra M.S.C. Mazzoni L.M. Malard, M.H.D. Guimarães and A. Jorio. Group-theory analysis of electrons and phonons in n-layer graphene systems. *Phys. Rev. B*, 79:125426, Mar 2009.

[18] Z. Li R. Zhao L. Tong Z. Liu J. Zhang S. Zhang, J. Wang and Z. Liu. Raman spectra and corresponding strain effects in graphyne and graphdiyne. *The Journal of Physical Chemistry C*, 120(19):10605–10613, 2016.

[19] D. Wang Y. Li Z. Shuai M. Long, L. Tang. Electronic structure and carrier mobility in graphdiyne sheet and nanoribbons: Theoretical predictions. *ACS Nano*, 5(4):2593–2600, 2011.

[20] B.Q. Song S.X. Du L.D. Pan, L.Z. Zhang and H.-J. Gao. Graphyne- and graphdiyne-based nanoribbons: Density functional theory calculations of electronic structures. *Applied Physics Letters*, 98(17):173102, 2011.

[21] W. Qiao H. Bai, Y. Zhu and Y. Huang. Structures, stabilities and electronic properties of graphdiyne nanoribbons. *RSC Adv.*, 1:768–775, 2011.

[22] C. Sun and D.J. Searles. Lithium storage on graphdiyne predicted by dft calculations. *The Journal of Physical Chemistry C*, 116(50):26222–26226, 2012.

[23] M. Hankel Z. Zhu V. Rudolph Y. Jiao, A. Du and S.C. Smith. Graphdiyne: a versatile nanomaterial for electronics and hydrogen purification. *Chem. Commun.*, 47:11843–11845, 2011.

[24] S. Lin and M.J. Buehler. Mechanics and molecular filtration performance of graphyne nanoweb membranes for selective water purification. *Nanoscale*, 5:11801–11807, 2013.

[25] A. Szabo and N.S. Ostlund. *Modern Qantum Chemistry: introduction to Advanced Electronic Structure Theory*. Dover Pubns, 1996.

[26] J.K. Labanowski. Simplified and biased introduction to density functional approches in chemistry, 1996.

[27] J. Kohanoff and N.I. Gidopoulos. *Density functional theory: basics, new trends and applications*. Wiley-Blackwell, 1 2003. Chapter Number: 26.

[28] R. G. Parr and Y. Weitao. *Density-Functional Theory of Atoms and Molecules*. Oxford University press, 1995.

[29] J.P. Perdew and S. Kurth. *Density functionals for non-relativistic Coulomb system*. Oxford University press, 2003.

[30] C. Adamo and V. Barone. Toward reliable density functional methods without adjustable parameters: The pbe0 model. *The Journal of Chemical Physics*, 110(13):6158–6170, 1999.

[31] E.A. Nersesov. *Fundamentals of atomic and nuclear physics*. Mir Publishers, 1990.

[32] Carlo E. Bottani. Lecture notes of solid state physics, 2017.

[33] M. Tommasini. Lecture notes: Physical properties of molecular materials, 2016.

[34] P. Brüesch. *Phonons: Theory and Experiments I*. Springer series in Solid-State Sciences. Springer-Verlag Berlin Heidelberg, 1982.

[35] M. Sonoda Y. Tobe K. Tahara, T. Yoshimura and R.V. Williams. Theoretical studies on graphyne substructures: geometry, aromaticity, and electronic properties of the multiply fused dehydrobenzo[12]annulenes. *The Journal of Organic Chemistry*, 72(4):1437–1442, 2007.

[36] H. B. Schlegel G. E. Scuseria M. A. Robb J. R. Cheeseman G. Scalmani V. Barone G. A. Petersson H. Nakatsuji X. Li M. Caricato A. Marenich J. Bloino B. G. Janesko R. Gomperts B. Mennucci H. P. Hratchian J. V. Ortiz A. F. Izmaylov J. L. Sonnenberg D. Williams-Young F. Ding F. Lipparini F. Egidi J. Goings B. Peng A. Petrone T. Henderson D. Ranasinghe V. G. Zakrzewski J. Gao N. Rega G. Zheng W. Liang M. Hada M. Ehara K. Toyota R. Fukuda J. Hasegawa M. Ishida T. Nakajima Y. Honda O. Kitao H. Nakai T. Vreven K. Throssell J. A. Montgomery Jr. J. E. Peralta F. Ogliaro M. Bearpark J. J. Heyd E. Brothers K. N. Kudin V. N. Staroverov T. Keith R. Kobayashi J. Normand K. Raghavachari A. Rendell J. C. Burant S. S. Iyengar J. Tomasi M. Cossi J. M. Millam M. Klene C. Adamo R. Cammi J. W. Ochterski R. L. Martin K. Morokuma O. Farkas J. B. Foresman M. J. Frisch, G. W. Trucks and D. J. Fox. Gaussian 09. http://gaussian.com/, 2009.

[37] Michael Haley. Cheminform abstract: Synthesis and properties of annulenic subunits of graphyne and graphdiyne nanoarchitectures. *Pure and Applied Chemistry - PURE APPL CHEM*, 80:519–532, 08 2008.

[38] R. Orlando C. M. Zicovich-Wilson B. Civalleri L. Maschio M. Rerat S. Casassa J. Baima S. Salustro B. Kirtman. R. Dovesi, A. Erba. 2018.

[39] L. Maschio M. Sgroi M. Lorenz, B. Civalleri and D. Pullini. Benchmarking dispersion and geometrical counterpoise corrections for cost-effective large-scale dft calculations of water adsorption on graphene. *Journal of Computational Chemistry*, 35(24):1789–1800.

[40] A. Milani F. Innocenti and C. Castiglioni. Can raman spectroscopy detect cumulenic structures of linear carbon chains? *Journal of Raman Spectroscopy*, 41(2):226–236.